EFFECTS OF GEOMETRICAL ORDER ON THE LINEAR AND NONLINEAR

OPTICAL PROPERTIES OF METAL NANOPARTICLES

By

Matthew David McMahon

Dissertation

Submitted to the Faculty of the

Graduate School of Vanderbilt University

in partial fulfillment of the requirements

for the degree of

DOCTOR OF PHILOSOPHY

in

Physics

December, 2006

Nashville, Tennessee

Approved:

Professor Richard F. Haglund, Jr.

Professor Charles A. Brau

Professor David E. Cliffel

Professor Sokrates T. Pantelides

Professor Robert A. Weller

In memory of my grandfathers, Raymond E. McMahon and James A. O'Neill

To my beloved wife, Carissa

For my children, Bethany and Andrew

FOREWORD

Why on earth, you ask, *would anyone spend five years of his life – in his twenties no less! – studying the optical properties of metal nanoparticles*? The answer is largely provided by what I now call Weller's First Criterion:

Am I interested?

In short: Yes! For as long as I can remember, I have been fascinated with light and color. Earth's ubiquitous sun was for centuries the best light source available to scientists – even sophisticated twentieth-century techniques like Raman scattering were first discovered with sunlight – and so it served me in the laboratory of youth. I recall the immense power of sunlight being demonstrated on a crisp New England autumn morning by a cousin with a magnifying glass and a fleeting pyromaniac streak. The late-afternoon rainbows of August are still some of the best examples of profound beauty in nature. It is this combination of power and beauty that attracts me to the study of light.

Over the years, I have also developed a fascination with certain theological parallels which may be drawn. The Christian Bible claims that "God is Light"[*]; and, regardless of how literally this statement was meant to be taken, it is indubitable that the lightlike union of power and beauty was recognized some thousands of years ago as a reflection of the divine nature. Undoubtedly, better physicists and better theologians have conceived deeper parallels; I myself only claim to have been struck by the tirelessness, timelessness and constancy of light, and the infinite breadth of the electromagnetic spectrum. I have tried not to think too hard about the theological hubris therefore implicit in the idea of *controlling* light on the finest scales, which is more or less the subject of my research;

---

[*] I John 1:5.

and yet I feel the force of the ancient command to "subdue [the earth]"[†]. Or to para-phrase King Solomon, "It is the glory of God to conceal a thing; but the honour of physi-cists is to search out a matter." [‡]

The idea of controlling the arrangement of little bits of precious metal on spatial scales literally un-resolvable by human eyes is similarly compelling for me. It seems wondrous that in spite of their diminutive dimensions, they display brilliant colors that are macroscopically visible – creating breathtaking connections between the realms of the seen and the unseen. Perhaps it is appropriate, then, that the best-known historical use of metal nanoparticles is in the coloration of medieval stained glass windows.

Matthew McMahon

Nashville, Tennessee

[†] Genesis 1:28.
[‡] Proverbs 25:2 (KJV).

ACKNOWLEDGMENTS

It has been said that when God gives gifts, they nearly always come in the form of a person. This has proven true during my graduate career, and my profuse thanks are due both to God and to the people who made these last five years a rewarding and enjoyable – it might be more accurate to say *relentlessly* enjoyable – interval.

This dissertation would never have come to pass without the consistent vision, steady example and patient encouragement of my adviser, Prof. Richard Haglund. It has been a delight to work under his supervision. When I first came to Vanderbilt I worked extensively with Prof. Robert Weller, and I greatly appreciate his teaching and direction in those early years as well as his service on my committee. I also thank my committee members Prof. Charles Brau, Prof. David Cliffel and Prof. Sokrates Pantelides for their teaching, suggestions and criticism.

Prof. Royal Albridge was largely responsible for my coming to Vanderbilt through his leadership of the NSF Research Experience for Undergraduates program. Prof. Len Feldman (a Drew alumnus) was instrumental in bringing me to Nashville as well, and I enjoyed working closely with him during my first three years of graduate school. The students in the program, especially Kat Camenisch, April Teske, Cyndi Heiner, Eric Chancellor and Hugo Valle, made the summer of 2000 a memorable one.

I am proud to count many current and former physics students and faculty among my friends. I would like to thank a few of them specifically: Dr. Dennis Fong, Prof. Rene Lopez, Dr. Michael Papantonakis, Dr. Ricardo Ruiz, Prof. Ken Schriver, Stephen Johnson, Jae Suh, Eugene Donev, Davon Ferrara, Nicole Dygert, Chris and Katie Goodin, Ja-

Dr. Barry and Linnea Robinson, Ed Briscoe, John and Damariz Lamb, Dr. David and Jen Dismuke, Chris and Trish Pino, Les and Jocelyn Carter, Brian Lennon, Dr. Monica Smatlak, Lauri Hornbuckle, Mary Konkle, Dr. Jason Gillmore, Paul Lambert, Sharon Conley, Don Paul and Ginger Gross, Kenny Benge, and Josh and Allyl McClure. The people of Christ Community Church welcomed and nurtured me as well; I thank Rev. Kevin Twit and Rev. Scotty Smith for wise counsel and Christian teaching, David Hampton for frequent opportunities to exercise the right side of my brain through music, and Rex Schnelle and Paul Quillman for their friendship.

My family has been supportive from the beginning, and I thank my parents, Raymond and Sally McMahon, for their unflinching support and prayers. I thank also my siblings, Lauren, Joshua, James, Colleen, Sarah, Jonathan, David, Timothy and Abigail, for oft reminders of who I am, and for steadfast refusal to take me more seriously than I ought to be taken. My aunt and uncle Kathy and Ted Clark graciously provided free rent for my first year in Nashville – an enormous gift in the world of a graduate student! – and with my grandmother Sara Lee O'Neill helped me purchase a car.

Finally and firstly, this dissertation is dedicated to my wife Carissa, whose love, hard work, patience and cooking have made the last four years a joy; and to our children Bethany and Andrew, who remind me daily that certain things are more important than others.

TABLE OF CONTENTS

LIST OF FIGURES

xiii

CHAPTER I

INTRODUCTION

1.1 Introduction

Small bits of metal have strong optical resonances in the visible and near-visible region of the photonic spectrum. By *small* I mean much smaller than the enormous sparkly pieces of metal that appear in jewelry, smaller even than the wavelengths of visible light, yet quite a bit larger than individual metal atoms. This size range (from one to one hundred nanometers) is becoming known popularly as the nanoscale, and these small-but-not-too-small bits we refer to as metal nanoparticles (MNPs). In plainer terms, MNPs light up at various colors.

Mankind has always maintained an attraction to shiny objects, and MNPs have been incorporated in colored glass since at least the fourth century A.D. It was not until the late nineteenth century, however, when Michael Faraday suggested that nanoscale clusters of metal were the coloring agent in stained glass, that the phenomenon began to be investigated using the methods of modern science [1]. Faraday's hunch was exactly right; when medieval artisans incorporated metal compounds into glass, the metals segregated into small clusters rather than dispersing atomically, and the MNPs thus produced give stained glass its vibrant color. The Lycurgus Cup, a relic of the Roman Empire, contains 50-nm particles composed of a gold-silver alloy; in reflection it appears pale green, but when illuminated from the interior it glows bright red. In 1908 Gustav Mie published analytical expressions for the electromagnetic surface modes of small metal

spheres, demonstrating the optical resonances and giving Faraday's idea firm theoretical footing [2]. The intervening century of research has established that these "Mie resonances" are due to a collective electronic behavior, known as the localized surface plasmon resonance (LSPR), which depends on the *substance, size, shape*, and *surroundings* of the nanoparticle [3, 4].

1.2 Linear Optical Properties of Metal Nanoparticles

The linear optical properties of MNPs (those properties that are independent of the irradiance) are determined by the localized surface plasmon resonance (LSPR). A *plasmon* is a collective oscillation of electrons in a metal. There are three classes of plasmons, depending on the geometry of the metal under study. We now review the plasmon types and *attempt* to clarify the nomenclature, which is not well developed and can be confusing.

A **volume** or **bulk** plasmon refers to a collective longitudinal oscillation of electrons that occurs within the *bulk* of a metal (that is, beyond the penetration depth or "skin depth" of any optical field). As an example, a volume plasmon could be excited by a low-energy electron which penetrates into the metal and transfers its kinetic energy to a group of electrons; in fact, volume plasmon energies are typically measured by electron energy-loss spectroscopy (EELS). Volume plasmons have the highest energy.

A **surface** plasmon is a collective longitudinal oscillation of electrons that occurs at a boundary between a metal and a dielectric. The conduction electrons involved are all at the surface of the metal. A related excitation sometimes confused with the surface plasmon is the *surface plasmon-polariton*. If we confine the discussion to surfaces, the two

2

terms appear to describe the same physics; for example, Raether states explicitly that the terms are identical [5]. The difference is that the *polariton* excitation is coupled with photons, whereas a *plasmon* strictly speaking is not.

This difference is clarified in the nanoparticle case by the different dispersion of surface-plasmon-polaritons and "free" surface plasmons (which are excited by low-energy electrons rather than photons) for larger nanoparticle sizes ([3], p. 53). Thus, when we refer to a *surface plasmon resonance* that gives bright colors, we are actually discussing a type of *surface plasmon-polariton*. To be sure, the word "resonance" indicates resonance between the electron oscillation and the incoming/outgoing light, which implies a polariton-like excitation. The **localized** plasmon is essentially a special case of the surface plasmon-polariton in which the excitation is "localized" in three dimensions. This is precisely the case with a metal nanoparticle, and as such this is the type of plasmon to which we will refer most often.

Regarding terminology, the best trade-off between completeness and brevity appears to be "Localized Surface Plasmon Resonance", or LSPR. Many alternate terms occur in the literature, though, such as the following:

- Particle Plasmon (blessedly succinct, and I reserve a right to its occasional use);

- Mie Resonance, the historical choice, though only strictly valid for spheres;

- Surface Plasmon Resonance (SPR), perhaps the most common term;

- Surface Plasmon-Polariton (SPP); and the rather unwieldy but most complete

- Localized Surface Plasmon-Polariton Resonance (LSPPR).

A basic (semi-classical) picture of the LSPR may be described as follows: Consider a spherical MNP as a homogeneous sphere of electrons superimposed on a homogeneous

sphere of positive ions. When an alternating electric field is applied, the electron sphere can move in response to the field against the positive background. This motion creates an imbalance of charge at the surface of the sphere (and, incidentally, only at the surface). The imbalance provides a restoring force to push the electron sphere back the other way, and so on and so forth. It is conceptually helpful to note that in the localized case an individual electron's motion is not necessarily restricted to the surface. The charge imbalance occurs at the surface, and so the restoring force comes from the surface, but the electrons themselves may move through the particle interior. The "interior" electrons will participate to the extent that the external field can "reach in" and perturb them. This relates to the skin depth, or penetration depth for light, of the metal. Typical skin depths at optical frequencies are on the order of 20-80 nm in the noble metals (Ag, Au, and Cu) [3].

The LSPR for a given MNP depends on the following properties:

- **Substance**;

- **Size**;

- **Shape**; and

- **Surroundings**.

By *substance* we refer to the particular metal constituting the particle, specifying the material dielectric function. The *surroundings* may be thought of as comprising two categories. The primary meaning is the local dielectric environment of the nanoparticle. As used in this work, it also includes the possibility of electromagnetic interactions (both near-field and far-field) with nearby metal particles or surfaces. Interactions between
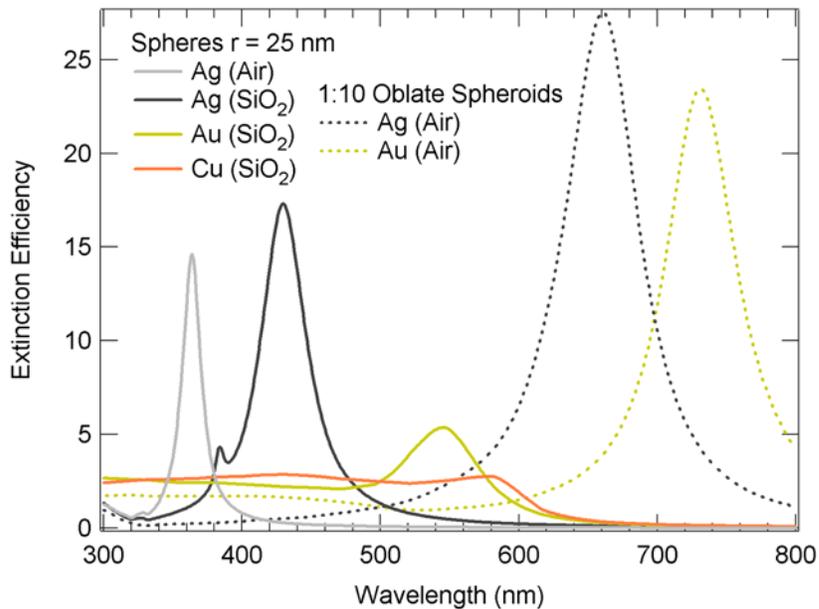
Figure 1.1. Calculated extinction spectra of noble metal spheres with 25 nm radius using Mie theory, and of oblate spheroids (major-axis mode) having nearly equivalent volume but 1:10 aspect ratio using the modified long-wavelength approximation, in various embedding media.

multiple particles with well-defined geometrical arrangements are of particular interest in this work. We will now discuss each of the above factors in more detail.

Substance. Restricting our discussion to noble metals: All other parameters being equal, the LSPR of silver will occur at the highest energy (shortest wavelength), followed by gold, then copper at the lowest energy (longest wavelength). For the ideal case of spheres in vacuum, silver also has the strongest (brightest) resonance by more than an order of magnitude; gold is slightly stronger than copper. See Fig. 1.1 for examples. These differences relate directly to the different dielectric functions of each metal. The different LSPR spectral positions and strengths mirror the reflectivity of the bulk metals, and are related to the differing onset of interband transitions in each; Ag has a sharp interband absorption peak around 4 eV, whereas Cu has a relatively broad interband ab-

sorption beginning at about 2 eV [6]. (It should be noted, therefore, that the Mie resonances in noble metals are not truly free-electron-like, but rather "hybrid" resonances with contributions from both *d*-band and conduction-band electrons [3].)

Size. Size effects are somewhat complex, but the most typical occurrence is that the LSPR will redshift with increasing size. We will discuss this further in Chapter II. I note in passing that *substance* can be related to *size*; nevertheless, all nanoparticles experimented upon in this work are well above the 10-nm range in which the dielectric function of noble metals depends on the particle size as well as the optical wavelength. One scientific motivation for studying metal nanoparticles is to probe this transition region from atomic behavior to bulk behavior through intermediate states which do not resemble either limiting case.

Shape. The LSPR depends strongly on shape. A sphere will have a single resonance, since it looks the same from all directions. In contrast, a general ellipsoid that has three unequal axes will have three different (but not independent) LSPR modes; that is, it will have a different color viewed from different directions. Fortunately, there are convenient mathematical formulations for "nice" shapes like ellipsoids. Unfortunately, even for ellipsoids the analysis is very complex [4], and convenient formulas for some more complex shapes have not been found.

Surroundings. The dielectric environment of the particle helps to determine the strength of the restoring force that the electrons experience. In general, for non-absorbing surroundings, an increase in the index of refraction of the surroundings redshifts the LSPR. The spatial distribution of the surroundings matters as well: it makes a difference whether a MNP is embedded in glass or resting on a substrate. Substrates tend

to be difficult to account for theoretically [7], and so-called "effective-medium approximations" are often used [8]. As an example, for a particle resting on a glass substrate in air, one might model the particle as if it were embedded in a homogeneous medium having refractive index 1.2, *i.e.* an effective index of refraction between 1 and 1.5.

The interplay between the *substance* and the *surroundings* is critical, and occasionally non-intuitive. Specifically, differences in the wavelength-dependent behavior of the dielectric functions involved can substantially alter both the position and strength of the LSPR. For instance, the LSPR of Cu NPs becomes dramatically brighter if they are embedded in a high-index dielectric as opposed to air, because the resonance is shifted away from the interband absorption edge [3].

These dependences lend themselves to several applications. One particularly active field, biochemical sensing, takes advantage of the high sensitivity of the LSPR to the local dielectric environment of the MNP [9-11]. A group at Northwestern University has demonstrated 100-zeptomole sensitivity with silver nanoparticles, and their results indicate that true zeptomole sensitivity is feasible [12]. Biochemical sensing is routinely performed on metal thin films with SPR spectroscopy, and the use of MNPs is primarily an extension of that technology.

It is noteworthy that ordered arrays of MNPs have been produced by lithographic methods for over two decades [13], but the function of the order has been primarily to study particle-particle interactions, *e.g.* by controlling interparticle distance. Virtually no work has been done to exploit the diffractive character of a square grating, though there has been work that acknowledged the diffraction implicitly through its effects on particle plasmon lifetimes [14] or so-called waveguide plasmons [15] (for a 1-D grating).

1.3 Nonlinear Optical Properties of MNPs

The nonlinear (or irradiance-dependent) characteristics of MNPs are not nearly as well-known as the linear properties. I limit the discussion here to second-order nonlinearities, since they are the only ones treated in the dissertation. In particular, second harmonic generation (SHG) has been used frequently to study ultrafast electron dynamics in MNPs by second-order autocorrelation, or local electric-field effects like surface-enhanced Raman scattering (SERS), but has been rarely considered on its own merits.

The primary difficulty with studying SHG in metal nanoparticle arrays is the well-known fact that symmetry forbids the generation of even harmonics by electric dipole sources in the forward and backward directions. Most researchers have only considered the traditional normal-extinction geometry in which excitation and detection are both perpendicular to the sample; in such an arrangement, second-harmonic light cannot be observed from symmetric particles. For second-order autocorrelation measurements, therefore, it has been necessary to use asymmetric particle shapes like triangles or Ls. These may be readily fabricated with lithographic techniques, but such complex shapes make modeling even the linear optical properties difficult. One would have to resort to numerical methods like the discrete dipole approximation, which divides a single particle into many smaller cubes to calculate the polarizability. To be sure, for electron dynamics measurements not much care has been taken to model the linear MNP properties, much less the nonlinear ones; the extinction spectra are typically treated phenomenologically, although general trends like size dependence can be inferred by analogy to disks. It seems rather obvious, for instance, that nonlinear yield will be enhanced when the particle plasmon is tuned to match either the fundamental or a harmonic of the pump laser.

8

The second harmonic of a laser beam may also be generated by a technique termed hyper-Rayleigh scattering (HRS), which has been used by chemists to study metal nanoparticles in solution [16]. Although the second-harmonic light produced by HRS is forbidden in the forward and reverse directions, it *can* be emitted in other directions. The scattered second-harmonic light is measured perpendicular to the pump beam, where the maximum of a dipolar radiation pattern that goes to zero in the forward and backward directions will occur. The mechanisms of HRS are themselves incoherent (that is, they have no well-defined phase), and since the particles are in constant Brownian motion the signal would be incoherent regardless.

Up to the present, there has not been a method for examining the second-order nonlinear optical properties of MNP arrays whose linear optical properties are relatively well-known and easily calculable. In contrast to the linear case, it has been explicitly suggested in the literature that arranging nanoparticles in a diffraction grating could be beneficial in SHG studies. A seminal paper by Wokaun and coworkers in fact examined diffracted SHG from silver nanoparticles in reflection mode [17]; however the particles they used were formed by evaporating silver at a sharp angle over a grating of silica pillars, meaning that the particles produced were rather like oddly-shaped half-caps and were not even flat, much less symmetric. (Even at that, they seemed more interested in SERS than in SHG *per se*.) This idea of using a diffraction grating to separate harmonic from fundamental light, and to spatially phase-match the SH light from MNPs, was revisited in a recent theoretical paper by Zheludev and Emel'yanov [18], though they too based their work on asymmetric triangular wedges with a complicated analysis that I, at

least, have been unable to verify. No one has yet even broached the possibility of studying symmetric particles like oblate spheroids or general ellipsoids with such a method.

1.4 Justification

The unique contributions of the work described in this dissertation are the following:

- Successful development of a focused-ion-beam lithography technique for the production of metal nanoparticle arrays. To my knowledge, the application of the FIB to lithographic nanoparticles is unique; though I note in Chapter III several good reasons why most researchers use electron-beam lithography instead. Regardless, Vanderbilt University is now one of only a handful of research institutions worldwide to demonstrate high-quality lithographic arrays of metal nanoparticles.

- By monitoring the LSPR of silver nanoparticle arrays over time, I have demonstrated that silver nanoparticles tarnish more rapidly than bulk silver when exposed to normal ambient levels of sulfur-bearing compounds, highlighting the sensitivity of the LSPR to changes in the chemical surroundings of the nanoparticle. This result may affect the implementation of certain nanoparticle-based sensors. It also has important implications for nonlinear optical measurements of silver NPs since, for instance, second-harmonic-generation is known to be highly surface-sensitive.

- Construction of a unique angle-resolved microscope for detection of second-harmonic light (or any other kind of light, for that matter) at arbitrary azimuth angles. The instrument is a kind of planar-array analogue of a polar nephelometer as described in Bohren and Huffman [4].

- The angle-resolved microscope enabled what I believe to be the most significant result of the dissertation: the first measurements of diffracted second-harmonic light from nanoparticles possessing planar inversion symmetry. Such a measurement is novel in itself, but more importantly, it makes it possible to essentially measure the nonlinear optical properties of a single particle of subwavelength dimensions with far-field excitation and detection. (Granted, this is a bit of an overstatement, as no lithographic ordered array will be perfectly monodisperse. However, in high-quality arrays the inhomogeneities can be quite small – amounting to a few percent of particle size, and such roughness inconsistencies can also have a very small impact on the optical properties. In addition, recently developed fabrication methods [19] allow chemically synthesized colloidal nanoparticles, which can be much more uniform than lithographic particles, to be organized in lithographic arrays.) For instance, we can distinguish between dipolar and quadrupolar second-harmonic radiation patterns directly in angular space. In addition, we measure unprecedented second-harmonic signal levels from metal nanoparticle arrays.
- We have advanced the state-of-the-art in the computation of the optical properties of arrays of metal nanoparticles, by taking account of specific excitation and detection geometries other than traditional normal-incidence extinction within a coupled-dipole formalism.

Metal nanoparticles are already finding use through their linear optical properties in biochemical sensing applications [12, 20]. The possibilities for nonlinear applications are just beginning to be explored, however, and it is in this area that my dissertation is likely

to have the greatest impact. The fact that the diffraction allows symmetric particles to be studied by second-order methods is itself crucial to the basic understanding of nonlinearities in metal nanoparticles. Current models of second-order nonlinear behavior in lithographic MNP arrays are necessarily complicated by asymmetrical particle shape, and are also measurement-specific [21]. The diffracted second-harmonic measurement provides a possible pathway to test theoretical models connecting the LSPR modes of the nanoparticle directly with the second-order nonlinear optical properties.

Potential nonlinear applications are not addressed directly in this work; but the use of diffracted second-harmonic light emphasized in my dissertation is a paradigm for the study of the basic second-order optical behavior of metal nanoparticles, which heretofore has not been possible for symmetric particle shapes. This may well lead to future applications. Symmetric NPs can be modeled in a straightforward manner, making connections between SHG and materials properties more practical. There is nothing intrinsic to the diffraction method that limits the technique to the study of second-order nonlinearities; third-order nonlinearities (which are responsible for the nonlinear index of refraction and nonlinear absorption) and higher nonlinearities could be studied as well. In addition, in conjunction with ultrafast excitation sources like Ti:sapphire lasers, it is conceivable to apply this technique to some of the most fascinating proposals for nanoscale plasmonics, such as surface plasmon amplification by stimulated emission of radiation (called "spaser" by analogy to the laser and maser [22]). Other possibilities include proposed applications in nonlinear optical signal routing and processing, possibly assisting the development of ultrafast photonic circuitry to infringe upon the domain of conventional electronics [23, 24]. Ideas that advance this frontier will necessarily rely on exploiting

nonlinear optical behavior. Photonic components need not behave like conventional circuitry – for example, nonlinear optical behavior can provide self-switching mechanisms [25]. It is also noteworthy that controlling the grating spacing of an ordered array allows control of the radiated angle of the harmonic light, which could be of use in signal routing. In any case, it is clear that understanding the nonlinear behavior of metal nanoparticles will be critical for the development of nanoscale plasmonics.

1.5 Organization of the Dissertation

The dissertation is organized into nine chapters including this one. Chapter II introduces theoretical computations of the optical response of MNPs. In Chapter III I describe the method of nanoparticle preparation, focused ion beam lithography, used extensively in this work. I also describe the setup and alignment of a dual-angle confocal fiber microscope that I designed and constructed.

The remaining chapters are organized by experiments. Chapter IV gives an example of the optical effects caused by tarnishing of silver nanoparticles. In Chapter V we first take up the topic of order, by presenting an explicit demonstration of the diffractive properties of ordered MNP arrays. Chapter VI begins a study of diffracted second-harmonic light from gold nanorod arrays which is extended in Chapter VII. In Chapter VIII we examine whether electric-field "hotspots" measurably change the second-harmonic output of a MNP array. Chapter IX concludes the dissertation with a summary of the principal results and a brief discussion of experiments that would naturally follow from those described herein.

CHAPTER II

COMPUTATIONAL MODELING

2.1 Introduction

Gustav Mie's now century-old classical theory describing the optical response of a metal sphere embedded in a dielectric has been remarkably successful despite its limited scope [2, 3]. However, modern fabrication techniques (*e.g.* planar techniques like EBL and IBL, as well as chemical synthesis of nonspherical NPs) have enabled researchers to study deviations from Mie's ideal case. The LSPR resonances of metal nanoparticles are now known to depend upon the shape and arrangement as well as the size and dielectric environment of the particles. In this chapter, we present computations of the optical properties of collections of metal nanoparticles with electromagnetic interparticle interaction. Along the way, we give a rough sketch of the theoretical basis for the optical properties of metal nanoparticles.

Numerical simulations of the optical properties of metal nanoparticles are desirable for a number of reasons. First, when done by computer they represent perhaps the fastest way to compare experimental results with theoretical models. Second, when the models have been shown to match experimental results, they can be used in a predictive manner to guide the experimenter's craft. Third, there exist only a handful of cases (spheres, oblate/prolate ellipsoids) that yield analytical solutions to Maxwell's equations, and even then one is often restricted to particles much smaller than the wavelength of light (*i.e.* quasistatic approximation) [4]. For larger sizes, other shapes (such as general ellipsoids,

or cubes [26]), and especially for large sizes *of* other shapes [27], the mathematical expressions can be rather frightening, and in general numerical simulation is necessary. We note in passing the existence of several numerical methods used to calculate the optical response of nanoparticle systems, particularly with nonspheroidal shapes, which will not be discussed in detail: T-matrix methods [28], finite-difference time-domain calculations (FDTD) [29], discrete dipole approximation (DDA) [30], multiple multipole approximation (MMA) [31], and conjugate-gradient fast Fourier transform (CG-FFT) [32]. We will focus on the coupled dipole approximation (CDA) [33], as it is perhaps the most convenient for calculating the response of arrays of particles – especially particles like spheroids, whose polarizability may be put in a tractable form.

The CDA, recently popularized by Schatz and co-workers, is an important step toward computationally modeling the collective electromagnetic response of arrays of nanoparticles. In this model each particle is treated as a radiating dipole, driven by an incident electromagnetic field; the particles interact through their retarded fields. The existing literature on the CDA deals mainly with computing extinction and scattering efficiencies, to calculate for array geometries what Mie calculated for single particles. In this chapter we present an extension of the CDA with the goal of increasing its utility for simulating the outcome of a wide class of potential optical experiments. We compute the total power radiated into the direction and solid angle that accurately describes the physical detector being used, by integrating the far-field intensity in the detector region once the self-consistent electromagnetic response of the interacting dipoles has been found. This technique captures certain features of the optical response that are overlooked by

efficiency calculations and may be experimentally probed by specific measurement configurations.

These computations are performed in a reasonable amount of time, so a significant number of particles in an array may be modeled. It should be possible to create and optically probe lithographic arrays of particles that can be modeled fairly closely by our calculations. A remark about the size of arrays is in order. Researchers have used fast Fourier transform (FFT) methods to calculate the response of arrays of infinite size. Such techniques are useful because they greatly reduce the computation expense while accurately modeling arrays that extend over very large areas. For the technological advancement of nanoscale photonics and plasmonics, however, it seems quite likely that there will be a need for photonic structures that accomplish a particular function while maintaining a small size. So it may prove very useful to understand the so-called "finite size effects" (referring to the finite number of particles in the array), which provides another motivation for this work.

2.2 Coupled Dipole Approximation

2.2.1 Theory

The CDA models the dipolar (lowest-order) optical response of arrays of individual nanoparticles, without including higher-order multipoles. The dipole moment induced in a single particle by a local electric field is given by the equation (SI units)

$$\vec{p}_i = \varepsilon_0 \alpha_i \vec{E}_{loc}(\vec{r}_i) . \tag{2.1}$$

Here $\vec{p}_i$ is the induced dipole moment, α_i is the polarizability of the particle centered at $\vec{r}_i$, $\vec{E}_{loc}$ is the local electric field, and ε_0 is the permittivity of free space. As an

example, for spheres in the quasistatic approximation (QSA) (radius $a \ll \lambda$ wavelength), the polarizability takes the form

$$\alpha = 3V \frac{\varepsilon - \varepsilon_m}{\varepsilon + 2\varepsilon_m} \tag{2.2}$$

where $V = \frac{4\pi}{3} a^3$ is the sphere volume, ε is the dielectric function of the particle and ε_m is the dielectric function of the surrounding medium. It is immediately seen from Eq. 2.2 that a resonance in the polarizability will occur when the following condition is satisfied:

$$\varepsilon = -2\varepsilon_m . \tag{2.3}$$

Other forms of the polarizability, including the modified long-wavelength approximation (MLWA) and a dipolar approximation from Mie theory, will be discussed below.

The local field arises from two sources, appearing as two terms. The first term is the incident light, $\vec{E}_{inc}(\vec{r}_i) = \vec{E}_0 e^{i\vec{k} \cdot \vec{r}_i}$ (where wavevector $\vec{k} = k\hat{k} = 2\pi\hat{k}/\lambda$). The second term is the superposition $\vec{E}_{ret}$ of the retarded fields from each of the other N-1 radiating dipoles in the array. Combining these terms, we have for the local field

$$\vec{E}_{loc}(\vec{r}_i) = \vec{E}_0 e^{i\vec{k} \cdot \vec{r}_i} - \sum_{\substack{j=1 \\ j \neq i}}^{N} \frac{1}{4\pi\varepsilon_0} \frac{e^{i\vec{k} \cdot \vec{r}_{ij}}}{r_{ij}^3} \left\{ k^2 \vec{r}_{ij} \times \left(\vec{r}_{ij} \times \vec{p}_j \right) + \frac{1 - ikr_{ij}}{r_{ij}^2} \left[r_{ij}^2 \vec{p}_j - 3\vec{r}_{ij} \left(\vec{r}_{ij} \cdot \vec{p}_j \right) \right] \right\} \tag{2.4}$$

Here $\vec{r}_{ij} = \vec{r}_i - \vec{r}_j$, and $r_{ij} = |\vec{r}_{ij}|$. We may now write Eq. 2.1 entirely in terms of the incident field, by substituting Eq. 2.3 for the local field and rearranging terms. This yields a matrix equation of the form

$$\vec{E}_{inc,i} = \alpha^{-1} \vec{p}_i + \sum_{j \neq i} A_{ij} \vec{p}_j \tag{2.5}$$

17

in which the A_{ij} are 3 x 3 matrices representing the interaction of two particles i and j.

Using the notation of the Northwestern research group, we may write Eq. 2.5 in the more

computationally suggestive form $A' p = E_{inc}$ in which A' is a 3N x 3N matrix and both p

and E_{inc} are 3N vectors (*i.e.*, each of N particles is represented by a 3-vector). When this

set of 3N complex linear equations is solved, the array p of self-consistent dipole mo-

ments is obtained. The optical properties may then be calculated from this dipole array;

for example, the unitless extinction and scattering efficiencies follow.

$$Q_{ext} = \frac{k}{\pi a^2 \varepsilon_0 |\vec{E}_{inc}|^2} \sum_{i=1}^{N} \mathrm{Im}(\vec{E}^*_{inc,i} \cdot \vec{p}_i) \qquad (2.6)$$

$$Q_{sca} = \frac{k^4}{6\pi^2 a^2 \varepsilon_0^2 |\vec{E}_{inc}|^2} \sum_{i=1}^{N} \left| \vec{E}^*_{inc,i} \cdot \vec{p}_i \right|^2 \qquad (2.7)$$

In general, the absorption efficiency $Q_{abs} = Q_{ext} - Q_{sca}$. In the quasistatic limit, absorp-

tion dominates so that $Q_{abs} = Q_{ext}$.

At this point, most calculations conclude. The framework here is certainly adequate

to calculate the expected outcome of an extinction measurement, and has been used for

that purpose. However, there may be experimental configurations for which the standard

normal-incidence extinction calculations will not apply. One can easily imagine an ex-

periment in which scattered light in some given direction is the measured quantity rather

than normal extinction; in fact, such measurement geometries occasionally appear in later

chapters. More importantly, nanoparticle arrays possessing high degrees of symmetry

can be expected to exhibit angular variations in their optical response, particularly when

illuminated at non-normal incidence. For instance, an appropriately designed two-

dimensional square lattice of metal nanoparticles will act as a Bragg reflector, as will be

demonstrated in Chapter 5. Consequently, the solid angle of the light-collecting device may also impact the observed optical response. For these types of measurements, an accurate calculation must take directional and solid-angle effects into account. One potential benefit of this approach is the possibility of designing arrays of nanoparticles whose optical response has a specified angular emission characteristic.

Fortunately, one is not limited to calculating extinction efficiencies and cross-sections once the dipole array is found. Specifically, the time-averaged power P radiated per unit solid angle Ω by an oscillating dipole moment $\bar{p}$ in the direction $\hat{n}$ into the far field is [34]

$$\frac{dP}{d\Omega} = \frac{c^2 Z_0}{32\pi^2} k^4 \left| (\hat{n} \times \bar{p}) \times \hat{n} \right|^2 \tag{2.8}$$

in which c is the speed of light and Z_0 is the impedance of free space. Equation 2.8 may be integrated over a given solid angle to yield the power radiated into that solid angle,

$$P = \frac{c^2 Z_0}{32\pi^2} k^4 \iint \left| (\hat{n} \times \bar{p}) \times \hat{n} \right|^2 \sin\theta \, d\theta \, d\phi \tag{2.9}$$

where the double integral runs over the desired limits for polar θ and azimuth ϕ angles. The integration limits are determined by the angular size and position of the light collection device to be used in the experiment, *e.g.* a microscope objective lens. We may solve the double integral numerically to find the power.

2.2.2 Survey

The CDA has been used most systematically by the Schatz research group at Northwestern University. What follows is a brief summary of the main results that have been achieved with the CDA, by that group and several others; some of these cases will be re-

visited later. The optical properties of one-dimensional chains and two-dimensional ar-

rays of Ag nanospheres with were studied with the CDA and the T-matrix method, which

is an exact calculation based on Mie theory [35]. It was found for 1-D chains that multi-

polar effects become especially important when particles approach closely; in particular,

the CDA is inadequate when the gap between neighboring particles is on the order of half

the particle radius. For 2-D arrays the CDA captures the most important array effects.

For Ag spheres with radius 30 nm, as the spacing is decreased from large values to 75 nm

(so spacing/diameter = 1.25) the LSPR blueshifts; as the particles approach even more

closely the LSPR redshifts slightly. In addition, the LSPR spectral width narrows slightly

from large spacing down to 180 nm (spacing/diameter = 3) and then broadens considera-

bly at still smaller spacings. This behavior results from the interaction of the retarded

dipole sums with the particle plasmon properties.

It was pointed out that multipole resonances, which are important for large spheres,

are suppressed in large ellipsoids with high aspect ratios. Thus, the quasistatic approxi-

mation may be useful for ellipsoids even when it fails for spheres of the same volume.

The optical properties of two interacting metal nanodisks were studied by experiment

and computation for Au and Ag [36, 37]. The experimental data were fit to a coupled-

dipole model with reasonable agreement. For light polarized along the nanoparticle-pair

axis, Coulomb attraction between the positive end of one dipole and the negative end of

the other reduces the interaction energy, redshifting the LSPR as the particles approach.

For light polarized perpendicular to the pair axis, repulsion between the positive and

negative sides of neighboring particles increases the interaction energy, blueshifting the

LSPR as the particles approach.

Narrow LSPR lineshapes (~1 nm) were found for one-dimensional chains of Ag nanospheres [38] with large spacing. The narrowing is due to interference effects, implying that an infinite chain produces the narrowest spectra. For 2-D arrays, the narrowing is much less pronounced.

2.3 Computational Considerations

We now show a broad-brush outline of the algorithm used, and give several recommendations for these computations. The calculations presented here were programmed in MATLAB and executed on a Pentium IV PC. The code I developed was initially verified by Prof. Robert A. Weller at Vanderbilt University, who wrote his own code for *Mathematica* on a Macintosh operating system; we calculated the optical response of identical silver nanoparticle arrays using the two programs in order to check the results against each other. I have used the MATLAB code independently to verify agreement with computations presented by the Northwestern group.

The computation algorithm adheres fairly closely to the derivation of the previous section. Physical constants (speed of light, impedance & permittivity of free space, etc.) and input parameters (particle radius and locations, dielectric functions, incident wavevector and polarization, detector solid angle, etc.) are defined first. The above equations must then be solved numerically at each wavelength of interest. The polarizability is wavelength-dependent through the complex dielectric function, so it is solved first. We may then use it to calculate the interparticle interaction matrices and find the matrix A', which is inverted to get the dipole array. The dipole array is used directly to compute the extinction properties.

We then use the dipole array in the numerical integration of Eq. 2.8; this is the primary contribution of this work. The integration process is computationally expensive compared with the extinction calculation, especially for large array sizes. The entire process may be repeated at each wavelength of interest (an algorithm I used), or done in full vector form including wavelength as a parameter (as Prof. Weller used).

The programs described here – especially the integrations – are computationally demanding, and if they are to be executed on a personal computer they must run as efficiently as possible. It takes a few seconds to calculate the extinction efficiencies of a given array over the visible wavelength range: it takes anywhere from several minutes to a few hours (depending on array size) to calculate the integrals over a realistic detector in the same wavelength range. For even moderately large arrays of 18 x 18 particles, it can take days to run a series of calculations in which a single parameter such as the interparticle spacing is varied. In particular, writing subroutines (which may be called tens of thousands of times) in fully vectorized form saves processing time. I have also found it immensely helpful to write vectorized versions of certain built-in MATLAB functions such as dot and cross products; examples are given in the Appendix.

Certain cautions may seem obvious, but I list them here for completeness. One must be careful to keep a consistent set of units throughout the computation. It is helpful to organize the units such that numbers appear without powers of ten wherever possible. (For instance, in my program the speed of light is given as ~300 nm/fs, a particularly memorable number for scientists interested in ultrafast nanoscale optics; see the Appendix for a list of units used in my program.) One must also be wary of operator definitions in certain programs, as they may be inconsistent with user assumptions. For example,

when the transpose of a vector is taken, some languages (like MATLAB) automatically perform a complex conjugate operation on the vector as well. Most of the matrices in this computation have complex values, so care must be taken with complex conjugation which may or may not be desired for a given matrix manipulation. It is easier than one might think to mistakenly use the complex conjugate of a vector to calculate scalar and vector products; this can be a difficult error to catch because you may complex-conjugate twice to display the vector itself, giving the apparent "right" answer.

2.4 Dielectric Functions

A brief digression regarding how dielectric functions are used in the calculations is of some practical importance. Perhaps the most comprehensive source of Ag dielectric function data is the *Handbook of Optical Constants of Solids* edited by Palik [39]; however, it sacrifices consistency for completeness. The data are collected from four sources, impressively spanning several orders of magnitude in photon energy. A closer look, though, reveals that the dataset switches sources right at the LSPR frequency of small silver spheres in vacuum. Several interpolation schemes have been used to average the difference between the datasets in the region of overlap, but the curves themselves indicate an offset between the two sources that may not be readily accounted for by such an interpolation. The Northwestern group has used exclusively the Palik data with such an interpolation.

We have preferred to use the data of Johnson and Christy [40] for both silver and gold, which extend over the entire spectral region of interest to us (300-1000 nm); as it happens, we are far from being alone in this choice [8, 41, 42]. The differences in the

raw dielectric function data seem somewhat trivial at a glance; however, they can be

magnified in calculations of the sort presented here. The disparities that appear in certain

calculations suggest that careful measurements of the optical properties of metal nanopar-

ticles eventually may be capable of distinguishing among competing dielectric function

datasets [3, 42]. We should state explicitly that we do *not* account for surface scattering

in what follows. For Ag, the electron mean free path is 52 nm; for Au, 42 nm [3]. Thus

in particles of 25 nm radius, the surface scattering is just becoming important, whereas in

particles of 10 nm radius significant deviations may be expected.
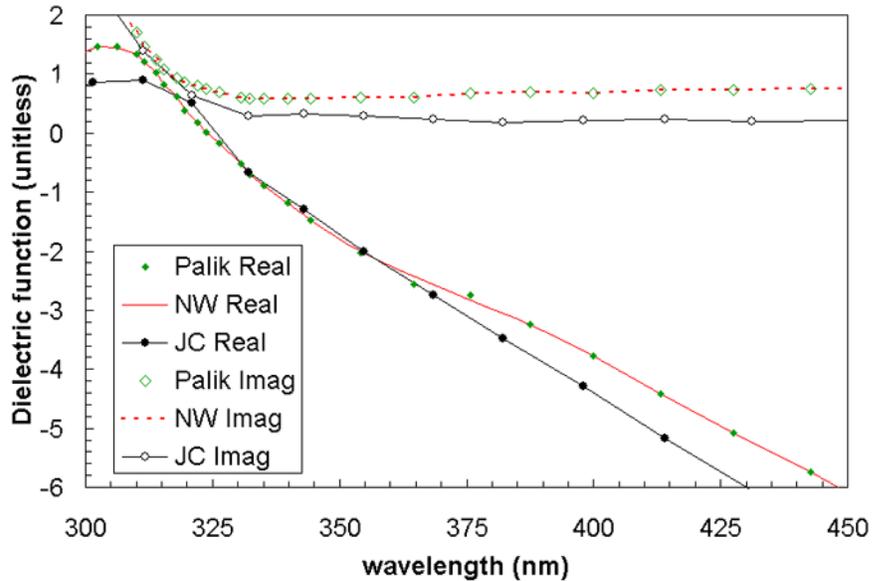
Figure 2.1. Comparison of Ag dielectric function data. At ~370 nm, Palik dataset switches source material. Northwestern's interpolation maintains the curvature change of the Palik dataset.

2.5 Polarizability Forms

In Section 2.2.1 we noted the quasistatic form of the polarizability for spheres in the

CDA. There are several other versions of the polarizability that may be used within the

basic formalism, depending on particle shape and the desired model. We now give an overview of these expressions.

MLWA. The QSA is a severe limitation when calculating the optical properties of spheres. Specifically, it ignores any spectral size-dependence of the resonance (other than scaling with volume). For sufficiently large particles it is necessary to adjust the particle polarizabilities to take into account two factors: 1) radiative damping, *i.e.* the effect of the reradiated field on the particle plasmon behavior, and 2) dynamic depolarization, caused by the finite ratio of particle size to wavelength (so that the QSA does not strictly hold). The resulting modifications to the polarizability constitute the modified long wavelength approximation (MLWA). First we write a more general form of the polarizability:

$$\alpha = V \frac{\varepsilon - \varepsilon_m}{\varepsilon_m + L(\varepsilon - \varepsilon_m)F},$$ (2.10)

where ε_m is the dielectric function of the surrounding medium, L is a shape factor = 1/3 for spheres, and within the QSA $F = 1$. To apply the MLWA we set

$$F_{MLWA} = 1 - (ka)^2 - \frac{2}{3}i(ka)^3;$$ (2.11)

Here a is the sphere radius (for ellipsoids it should be replaced with the semi-axis of interest). The second term corresponds to dynamic depolarization, the third to radiative damping [7]. (NOTE: I have adopted the terminology used by the Northwestern group but not their equations. In Ref. [33] an entirely different form of the spheroid polarizability is found from that of Bohren and Huffman, and the expression for the MLWA is accordingly different. There are several such oddities in Northwestern's published work. Evidently they yield the same answers, but the derivations of the equations are murky and

occasionally contain typographical errors. At least one of their versions of Eq. 2.4 contains an important sign error: the first minus sign on the right-hand side is incorrectly written as a plus sign in Ref. [35]. We initially discovered this by carefully applying the right-hand rule for the cross products.)

Mie Theory. Mie's treatment of spheres leads to expressions for scattering coefficients that may be used to calculate measurable quantities like optical efficiencies and cross-sections for single isolated particles. However, these coefficients may themselves be incorporated into the coupled-dipole formalism; that is, an effective electric dipole polarizability may be calculated from the first-order scattering coefficient, as demonstrated by Doyle [43]. The Mie scattering coefficients a_n and b_n are written as

$$a_n = \frac{m\psi_n(mx)\psi_n'(x) - \psi_n(x)\psi_n'(mx)}{m\psi_n(mx)\xi_n'(x) - \xi_n(x)\psi_n'(mx)},$$

$$b_n = \frac{\psi_n(mx)\psi_n'(x) - m\psi_n(x)\psi_n'(mx)}{\psi_n(mx)\xi_n'(x) - m\xi_n(x)\psi_n'(mx)} \tag{2.12}$$

where ψ_n and ξ_n are Riccati-Bessel functions, m is the *relative refractive index* of the particle compared with the embedding medium, and $x = ka$ is the size parameter. (The Mie expressions for optical cross-sections include summations over n from 1 to infinity.) The Riccati-Bessel functions and their derivatives can be expressed in terms of Bessel and Hankel functions (which MATLAB supports), or even more simply as combinations of sine and cosine functions using identities found in Ref. [44] (p.445). The effective dipole polarizability is related to the a_1 scattering coefficient [43]:

$$\alpha_{dipole} = i\frac{6\pi}{k^3}a_1 \tag{2.13}$$
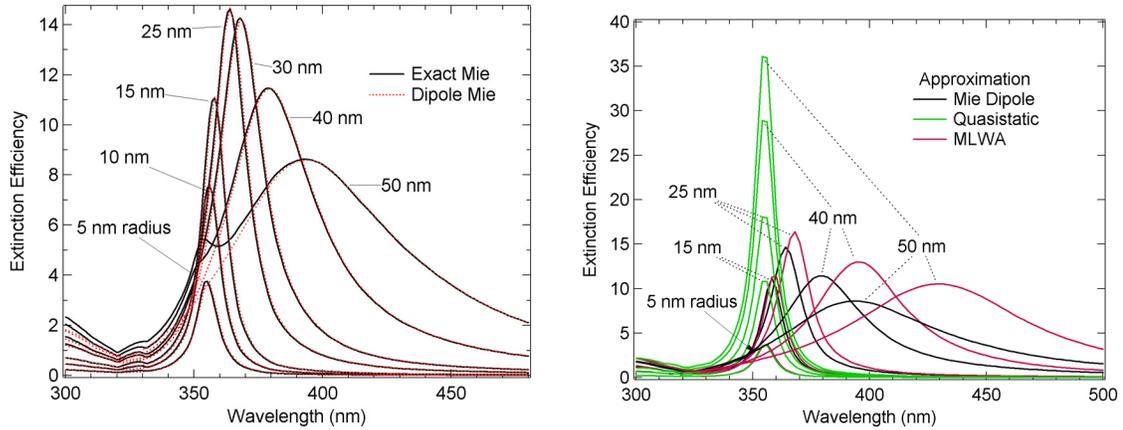
Figure 2.2. a) Comparison of Mie dipole approximation with exact Mie theory. b) Comparison of Mie dipole approximation, QSA, and MLWA for various particle sizes.

This represents an *exact* effective dipole polarizability independent of particle size; it is not subject to the QSA. (The above expression differs from Doyle's by a factor of 4π because we have chosen to work in SI units.) Doyle claims that for "good optical metals" such as silver, the dipole approximation gives good agreement with the full Mie theory. Mie coefficients were utilized, for example, in Ref. [38].

Comparison of Mie/Quasistatic/MLWA. We may examine the range of applicability of the Mie-dipole approximation by comparing with the exact Mie theory for spheres (MQMIE 2.4, Michael Quinten, Wissenschaftlich-Technische Software). Fig. 2.2a shows that for Ag spheres in vacuum, the Mie-dipole approximation closely follows the exact Mie extinction efficiency up to at least particle radius 50 nm. The exact Mie results indicate that at this size, the dipolar mode still dominates the small quadrupolar shoulder that occurs at higher energies. For particles of 100 nm radius (not shown), the short-wavelength shoulder develops into the strongest peak; the dipole no longer dominates and this approximation is no longer valid.

27

Fig. 2.2b demonstrates the size dependence of the QSA and MLWA compared with the dipolar Mie model for Ag spheres. Clearly, the quasistatic spectrum is unchanged with size, as expected from Eq. 2.2. For 5 nm radius, the correspondence with Mie theory is exact. As size increases, the QSA becomes progressively worse. (Somewhat ironically, the QSA works best where it works worst, because 5 nm radius in Ag is approximately where the real part of the dielectric function begins to depend strongly on particle size [3].) The MLWA is a considerable improvement at intermediate sizes, as the increased radiation damping with size is reflected in decreased amplitudes and the dynamic depolarization is seen in the redshift. However, at 40 nm radius, the redshift is exaggerated by 20 nm, and for 50 nm radius by 40 nm. In light of the fact that the Mie dipole expressions may be programmed fairly readily (provided one is willing to wrangle Riccati-Bessel functions) and do not appear to pose a significantly increased computational burden relative to the MLWA, it seems prudent to base any extinction calculations for spheres on the Mie-dipole formalism. We should note that the MLWA appears to be more useful for ellipsoids [33], for which exact computation schemes are much rarer, though they do exist (see, *e.g.* [45]).

Ellipsoids. The general form of the polarizability for an ellipsoid in the quasistatic approximation with semiaxes $a \geq b \geq c$ (not to be confused with the Mie coefficients) is as follows:

$$\alpha_i = V \frac{\varepsilon - \varepsilon_m}{\varepsilon_m + L_i(\varepsilon - \varepsilon_m)} \tag{2.14}$$

The shape factors L_i for the three possible axes obey the sum rule $\sum_{i=1}^{3} L_i = 1$. For spheres the shape factors all collapse to $L_i = 1/3$, by which we arrive at Eq. 2.2. For ob-

late and prolate spheroids, analytical expressions of the shape factors may be found. We list only the expression for an oblate spheroid, as it is a good approximation to a lithographically-prepared disk.

$$L_1 = \frac{g(e)}{2e^2}\left[\frac{\pi}{2} - \tan^{-1} g(e)\right] - \frac{g^2(e)}{2},$$

$$e^2 = 1 - \frac{c^2}{a^2}, \quad g(e) = \sqrt{\frac{1-e^2}{e^2}} = \sqrt{\frac{c^2}{a^2-c^2}} \tag{2.15}$$

Here e is the eccentricity of the spheroid, where the limiting values are a disk (1) and a sphere (0). For the oblate spheroid, $L_1 = L_2$.

The expressions for the shape factors of general ellipsoids are in integral form, as follows (here $i = a,b,c$);

$$L_i = \frac{abc}{2}\int_0^\infty \frac{dq}{(i^2+q)\sqrt{(a^2+q)(b^2+q)(c^2+q)}}. \tag{2.16}$$

However, the integrals may be solved straightforwardly in a few seconds using a computer program like *Mathematica*. Because at this time MATLAB does not handle infinities (or integrals in general) in a particularly natural way, *Mathematica* is greatly preferred for this calculation. The shape factor integral calculations are extraordinarily useful for calculating the linear optical properties of isolated metal nanoparticles, again within the quasistatic approximation. Combined with the dielectric function of the material, they can predict resonance peak positions for all three axes.

The results of shape factor calculations may be entered manually into a MATLAB computation; this requires no additional programming labor if all particles are assumed identical. It is worth noting that with a little effort, an array in which the individual parti-

cles have different isolated polarizabilities could be constructed and entered into the cal-

culation of self-consistent polarizabilities.

2.6 Does the Detector Make a Difference?

We now present results of CDA calculations with spheres. Our goal is twofold: to

demonstrate the effects of interparticle interactions on extinction spectra, and to test

whether a given detection geometry is correctly modeled by a simple efficiency calcula-

tion.
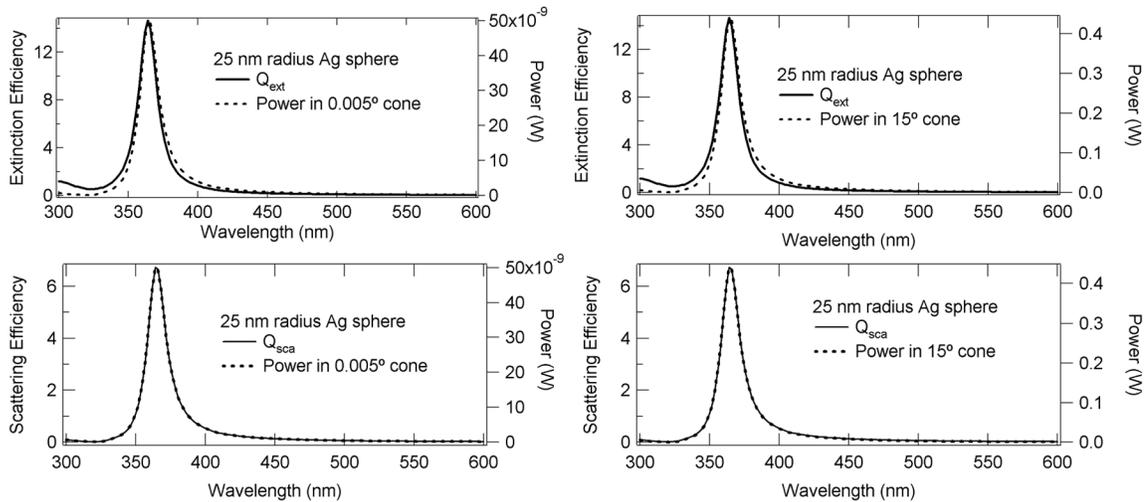
Figure 2.3. Extinction and scattering efficiencies for light normally incident on single 25
nm Ag sphere, compared with scattered power integrated over detector.

A check of the limiting behavior of the detector compared with an extinction effi-

ciency calculation in a traditional normal-incidence transmission or extinction measure-

ment demonstrates an important point. Strictly speaking, in the limit of zero solid angle,

the two calculations should coincide. Fig. 2.3 compares the extinction efficiency with

detector-integrated spectra for detector half-angles of 0.005° and 15°. We find for a sin-

gle 25-nm radius Ag particle that the integrated power is a decent approximation to the extinction efficiency over a considerable range of acceptance angles. If we plot the scattering efficiency, though, we find that the correspondence with the detector integration is *exact*. This highlights the fact that the detector integration does not take account of absorption in the particle the same way that an extinction measurement does; the integration only accounts for scattered light. In one sense this is as it should be; the detector should only see differences in scattering, not absorption. Nonetheless, if the detector integration is to model extinction measurements, the change in transmission due to absorption should be accounted for in some way. Tabling that discussion for the present, we note that the initial question now hinges on whether we can find differences between *scattering* efficiency and detector response, and point out that scattering dominates absorption in the limit of large particles. In any case, we have shown that for a single particle at normal incidence the simple extinction efficiency is a near-perfect model for an extinction measurement over an appreciable range of real detector angles, and the detector computation is essentially superfluous.
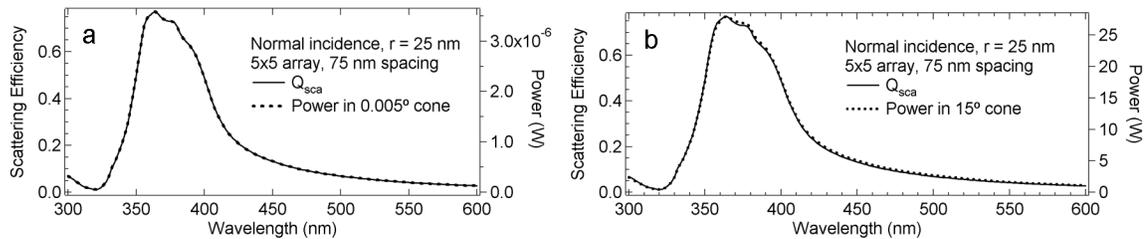
Figure 2.4. Comparison of scattering efficiency and detector integration for light normally incident on 5 x 5 square array of 25 nm Ag spheres spaced 75 nm apart. a) 0.005° cone; b) 15° cone.

If we extend this discussion to square arrays at normal incidence, we find again that for a 5 x 5 array with center-to-center spacing 75 nm the detector spectrum is identical to the scattering efficiency in the zero-angle limit, and even for 15° there are only the slightest spectral deviations (Fig. 2.4). However, if we consider a dark-field geometry in which the array is illuminated from above at a 45° angle, and scattered light is collected directly above the array, we find strong differences between efficiency and the integrated scattering, with strong polarization dependence and a moderate dependence on solid angle (Fig. 2.5).
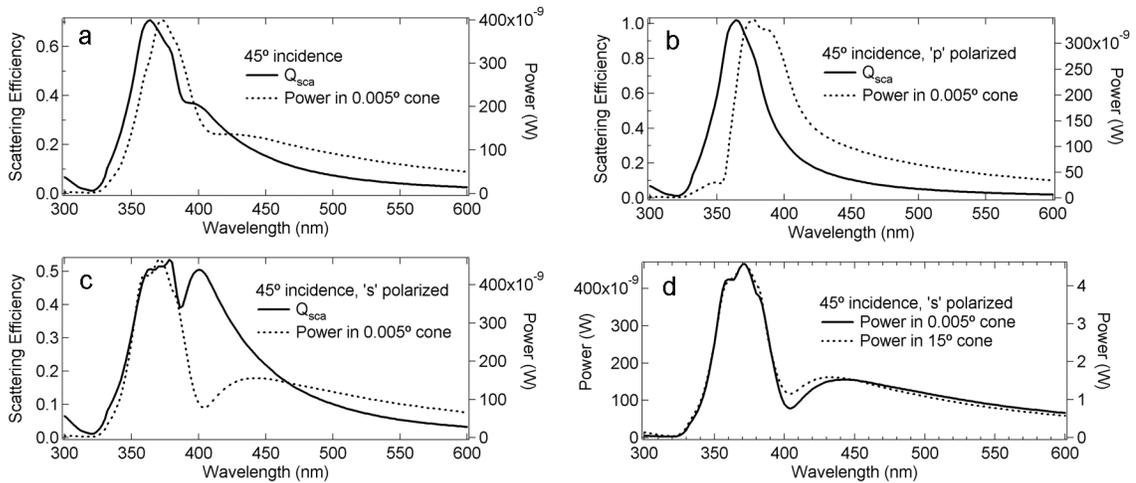
Figure 2.5. 5 x 5 array response under light incident from above at 45°, with wavevector projection along an array axis. a) Unpolarized; b) p-polarized; c) s-polarized. d) s-polarized with different detector acceptance angle.

The case of s-polarized light manifests the starkest difference between scattering efficiency and integrated power. Under s-polarized light the interparticle interaction is most asymmetric, in the sense that across a "row" of particles the polarizations are parallel, whereas across a "column" they are perpendicular. As mentioned previously, for a particle pair such excitation modes lead to opposite behavior (redshifting and blueshifting

32

respectively), and the behavior is complicated here by the presence of the extended array. Physically, the difference between the spectra is a manifestation of the angular dispersion of the scattered field.

As array size increases, for the normal-incidence case the agreement between the scattering efficiency and the integrated power in a 15° detector decreases somewhat, as shown in Fig. 2.6. In Fig. 2.7, we show the effects of increasing particle number for 45° dark-field incidence with s-polarized light. As an aid to the eye, the scattering efficiencies have been multiplied by particle number for comparison with the power graph. Again we see that the detector response captures certain interference effects not present in the scattering efficiency.
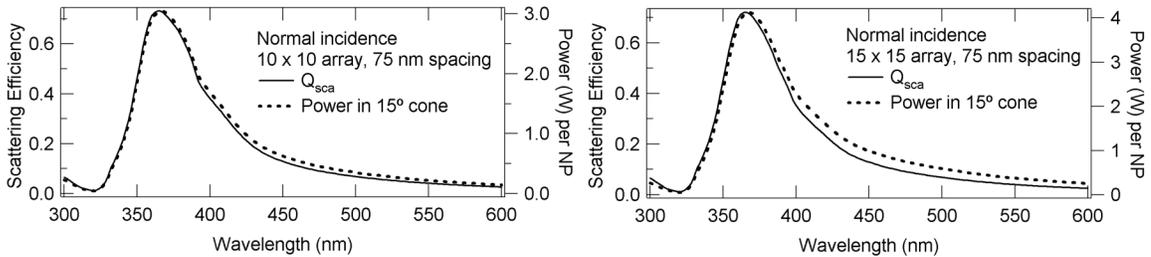
Figure 2.6. Comparison of scattering efficiency and integrated power in 15° cone for light normally incident on a) 10 x 10 array, b) 15 x 15 array. Compare Fig. 2.4b) and Fig. 2.3d).

At normal incidence, all particles are excited in phase; one might expect that the coherence properties dictate that in the forward-scattered direction, the spectrum will not be altered much by varying detector size. However, for a dark-field illumination scheme, the situation is evidently quite different, and the effects of detector geometry should be taken into account in order to accurately compare theory and measurement.
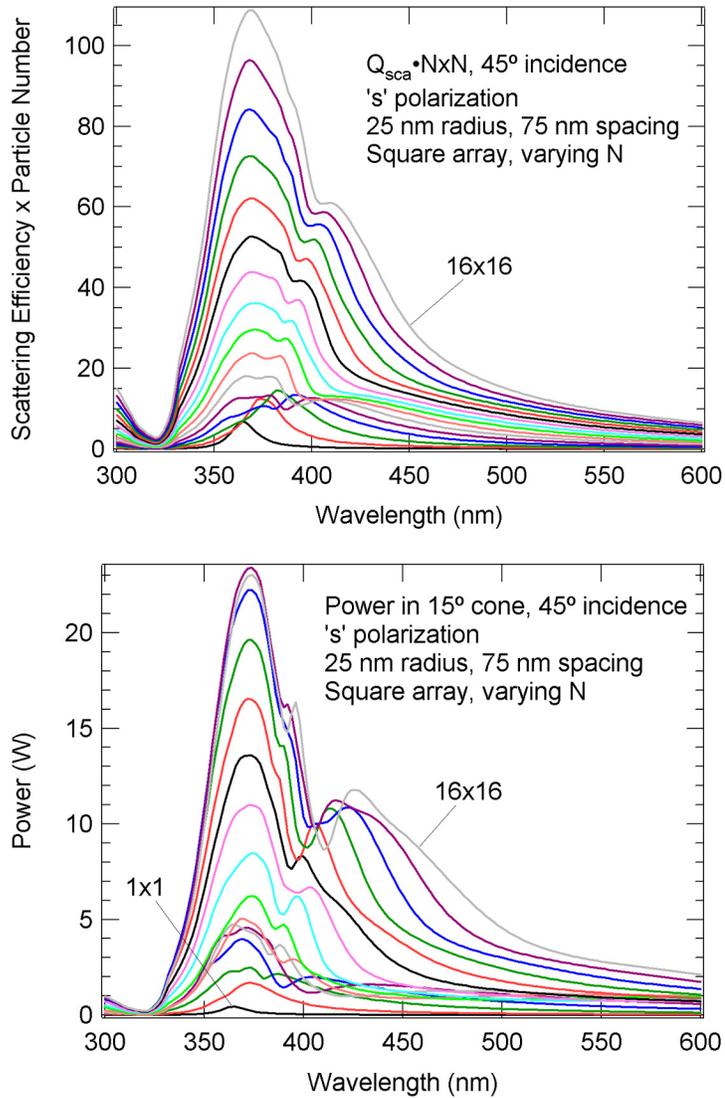
Figure 2.7. Comparison of a) scattering efficiencies and b) integrated power for varying particle number at 45° incidence. Scattering efficiencies are multiplied by the number of particles in the array as a visual aid.

CHAPTER III

EXPERIMENTAL TECHNIQUES

Nanoparticle arrays were prepared with focused-ion-beam lithography; various methods of structural characterization were employed. The ultrafast laser is briefly described. The angle-resolved confocal fiber microscope used to measure scattering at arbitrary azimuthal angle is discussed in detail, and alignment procedures are given.

3.1 Focused Ion Beam Lithography

All nanoparticle arrays in this work were fabricated with Focused Ion Beam (FIB) lithography (IBL) [46]. IBL is similar to electron-beam lithography (EBL) as described in the literature for nanoparticle preparation [8, 13, 47].

Lithographic methods all follow a similar general procedure. The desired substrate is coated with a thin layer of photoresist. The resist layer is exposed with an energized beam which may consist of photons, electrons or ions. The exposure sites determine either the final deposited image or its negative; resists are classified accordingly as "positive" or "negative". In this work the positive photoresist poly(methyl methacrylate) (PMMA) was used exclusively, as it is a common resist whose properties are relatively well-known, particularly for EBL. The exposed parts of the resist may be removed by chemical means. The remaining patterned resist is then coated with the desired material by any of several thin-film deposition techniques. After coating, the resist layer is re-

moved entirely in a chemical bath such as acetone. Deposited material atop the resist layer is removed as well, leaving behind the exposed image in the deposited material.

Substrates. Nearly all substrates used in this work were indium-tin-oxide(ITO)-coated glass slides (Delta Technologies CB-90IN-0105, having 15-30 nm thick ITO layer). The ITO is conductive enough to suppress charging during exposure and later imaging, yet sufficiently transparent (optical density OD less than 0.1 throughout the visible) to measure transmission and/or scattering in optical experiments. As received the slides were 25 mm x 25 mm squares; for processing ease we divided them into quarters measuring approximately 11 x 11 mm after cutting.

The ITO substrates are thoroughly cleaned before resist deposition. A typical procedure is to rinse the substrate in consecutive 30-40 mL baths of acetone (Fisher Acros, electronics use grade), methanol (Fisher Acros, electronics use grade), and de-ionized water. The rinses are then repeated, this time using a cotton swab submerged in the acetone and methanol baths to scrub the substrate clean, generally starting in the center of the substrate and sweeping outwards. Any further spot-cleaning is determined by examination of the substrate reflectance under room lights with the naked eye. Such a simple procedure is sufficient to achieve a clean surface with excellent resist coating characteristics, as confirmed by imaging during exposure. Substrates are blown dry with clean dry air (CDA).

Photoresist Preparation. A thin layer of PMMA photoresist is then spincoated onto the clean substrate. All films in this work were made from solutions of PMMA in anisole (Microchem 950 PMMA A4, 4% in anisole, diluted with Anisole 99%, Acros). We have found experimentally that diluting the solution to ~1.7% yields PMMA thicknesses in the

range of 55-60 nm. The vacuum chuck on the spin processor used in this work (Laurel WS-400A-6NPP/Lite) permits sample diameters as small as 1 cm; however, smaller samples may be accommodated by coating the opening with carbon tape and placing the sample on the tape. The resist solution is applied to the mounted sample with a pipette through an opening in the lid; at most 4 or 5 drops are required to coat a 1 cm x 1 cm sample. The standard spinning procedure (per Microchem recommendations) is to spin the sample at 500 rpm for 5 seconds to spread the solution over the entire sample, and then spin at 4000 rpm for 45 seconds to make a thin layer. The carbon tape mounting method will withstand 4000 rpm. The spun sample is then baked on a digital hotplate at 180° C for 60-90 seconds.

PMMA solution and film freshness is an important factor in film quality. A good rule of thumb to follow is "the sooner, the better". It is inadvisable to use PMMA films that are more than a few weeks old in any case. PMMA solutions, especially diluted solutions, should not be trusted for more than a couple of months without being tested by, *e.g.*, ellipsometry. Dilute solutions that have sat idle for any length of time should be thoroughly mixed before use as the solute will settle. The best results are usually achieved when films are made with fresh solution and used within 24 hours of preparation.

FIB Exposure. Resist exposure is performed with a commercial focused ion beam apparatus (FEI FIB200) having a 30 kV source of Ga^+ ions and a nominal beam diameter of 8 nm when properly focused. The FIB computer interface allows the user to define the sites to be exposed, and the exposure or dwell time at each site; thus arrays of arbitrary complexity may be patterned to the specifications of the researcher. The final array size

depends upon the working magnification of the FIB. On the FIB200, a magnification of 3675 X is calibrated so that the resolution is 20 nm/pixel and the final array size is ~75 μm square. Dwell time does not appear to be a critical parameter, provided that film thickness is in the 55-60 nm range; equivalent results have been obtained for identical array patterns prepared with 60 μs to 100 μs dwell time on the same sample. However, if the film thickness is larger, 100 μs is usually the safest time. The nominal beam current used in all experiments is 1 pA; however, the actual measured values according to the FIB picoammeter range from 2-4 pA.

Resist Development. Following exposure, samples were developed in a 1:3 solution of methyl isobutyl ketone (MIBK, Acros AC32792) to isopropanol (IPA, Acros AC32793) to remove the exposed regions of the resist. The 1:3 ratio is recommended by the PMMA manufacturer (Microchem) as yielding the highest resolution images. Various development procedures have been tested; the one that appears to yield the most consistent results is as follows. Two beakers containing ~40 mL and a third containing ~15 mL of the 1:3 solution are prepared. The sample is bathed for 30 seconds with gentle agitation in each of the first two solutions consecutively. The sample is then rinsed by pipette for ~30 seconds over the second beaker, using fresh solution from the third; the entire process takes 90 seconds. Following the development, the substrate should be gently blown dry with CDA, then "hard-baked" on a digital hotplate at 100° C for 90 seconds. The hard-bake is an important step, as it removes any remaining solvent in the patterned regions.

Thin-Film Deposition. The developed sample is then coated with a layer of metal of the desired thickness.[§] The coating may be done by any of several processes, of which this work employed two – Pulsed Laser Deposition (PLD) and thermal evaporation.

A commercial pulsed laser deposition system (Epion PLD 3000) was used in this work. In PLD, a tightly-focused laser beam ablates a target; the ejected material is collected on the substrate. The laser is a KrF excimer (Lambda-Physik Compex 205) with wavelength 248 nm. The laser energy is set to 400 mJ with a repetition rate of 25 Hz. A beamsplitter can be inserted into the optical path to divert ~50% of the light to a power meter. The meter reading is typically 0.5 W, giving a time-averaged power of ~40 mJ delivered to the target. From burn paper measurements of the spot size we estimate that ~70% of the beam energy is deposited into an approximately elliptical spot with axes 4 mm x 0.5 mm for an area of ~1.5 mm^2; thus the peak fluence at the target is approximately 2 ± 1 J/cm^2, the error dominated by the measurement of the spot size. The PLD vacuum chamber pressure is below 1 x 10^{-5} Torr. The target-sample distance is 7 cm. Both target and sample are rotated (0.5-1 Hz) and the laser beam is rastered across the target to ensure uniform deposition. Prior to each deposition the target is cleaned with ~10^4 laser pulses to remove any surface contamination. PLD of noble metals is a slow process. Depending on laser power, about 50,000 to 80,000 pulses (30-50 minutes at 25 Hz) are required to produce a 20-nm thick film of silver at 7 cm. In crude approximation, this indicates that ~ 600-1000 pulses are required to generate a monolayer of Ag at this distance. Mass thickness is determined *ex situ* by spectrophotometric measurement of the silver film thickness on a cover slide co-deposited with the sample.

[§] The coating, of course, need not be metallic. Any material whose processing is compatible with the resist layer may be used, and in fact other researchers at Vanderbilt have used FIB lithography to create arrays of metal oxide nanoparticles such as vanadium dioxide and sesquioxide via pulsed laser deposition [48].

Thermal evaporation was performed in a Denton Vacuum DV-502A evaporator. In thermal evaporation, large currents cause resistive heating, which evaporates the metal. Tungsten coiled-wire baskets suspended between two electrodes hold the metal shot. The distance between the basket and the sample is ~ 15 cm. Typical base vacuum pressure is 2×10^{-6} Torr. Typical currents needed to evaporate gold are of the order 30 A. Evaporation is a fast process for noble metals, with typical maximum deposition rates 0.5-1 nm/sec; the deposition rate may be controlled in real-time by controlling the current. Mass thickness may be monitored *in situ* with a quartz crystal microbalance (QCM); however, a cover slide is always co-deposited with the sample as a second check. Due to the different placements of the sample and the QCM, the QCM reading is typically 3/2 of the actual deposited thickness. This has been confirmed by measuring distances in the chamber, and by spectrophotometer tests. As the desired thickness is reached, the rate may be slowed by reducing the current, and a mechanical shutter may be used to abruptly stop deposition on the sample. The use of a custom sample holder which protects the sample edges from deposition improves the ease of the liftoff process.

Liftoff. Liftoff of the lithographic mask is performed by immersion in a bath of commercial solvent (Shipley Microposit 1165 Remover, or Remover PG) heated above 55° C. In general I have found that the bath should be heated to at least 57° C, and that hotter is usually better. Recently, good results have been consistently achieved using bath temperatures above 60° C. After the film has lifted off, the sample is rinsed in warm acetone and DI water baths and blown dry with CDA. Examples of nanoparticle arrays we have produced with IBL are shown in Fig. 3.1.
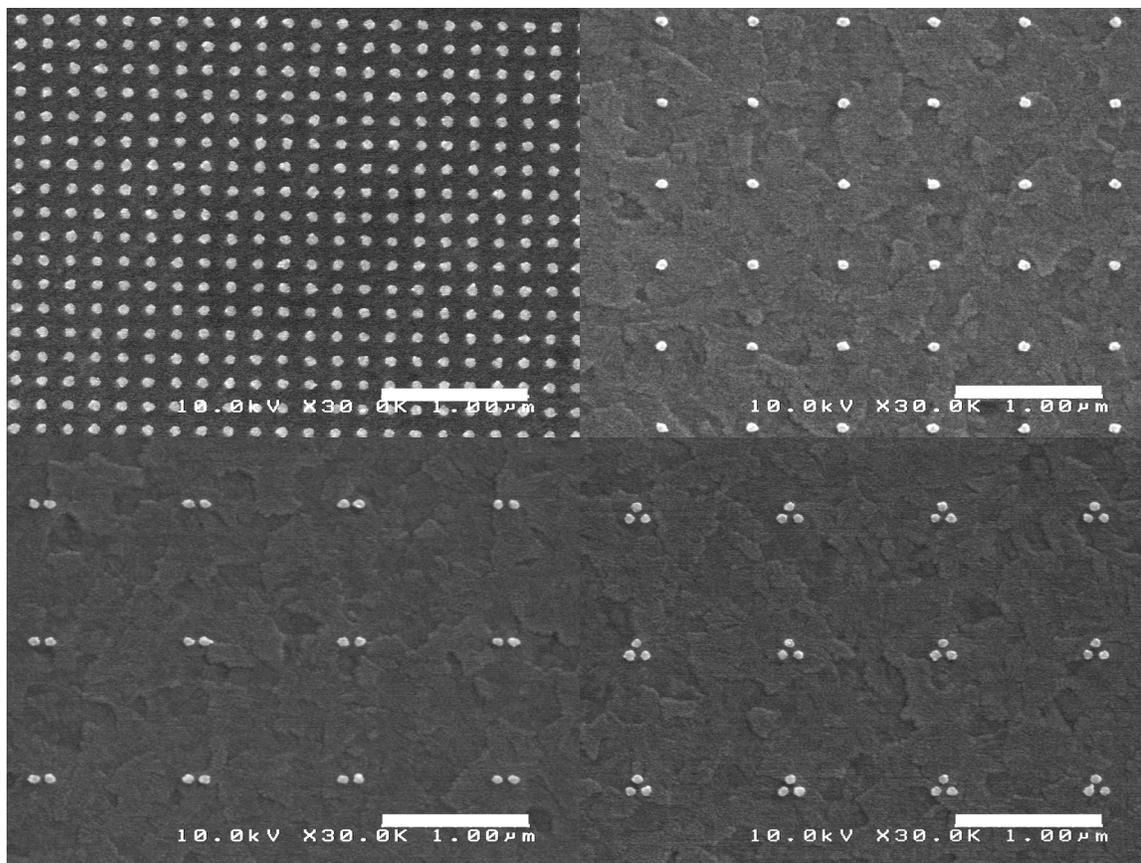
Figure 3.1. Scanning electron micrographs of Ag nanoparticle arrays produced by IBL. Scale bar in all frames is 1 μm.

Choice of Film Thickness. The range of 30 kV Ga$^+$ ions in PMMA may be calculated using the freeware SRIM/TRIM program to be about 50 ± 10 nm. This places a fundamental limit on the PMMA film thickness; for films thicker than 50 nm, only the tail of the ion distribution penetrates the entire film. The desired thickness of the deposited features places a lower limit on the resist thickness. Thinner metal films are easier to lift off for at least two reasons: 1) the lower the ratio between the metal film thickness and the resist thickness, the lower the probability that mechanical connections will form between the metal in the hole and the metal atop the resist; and 2) very thin metal films as deposited by PLD and evaporation are not truly solid; they have a porous structure which

the liftoff solvent can penetrate, dissolving the resist more easily. Mechanical connections would cause the particles to lift off along with the resist layer; they are minimized when the angle between the trajectory of arriving atoms and the substrate normal is zero, *i.e.* when fewer atoms have a chance to collect on the sidewalls. The porous metal-film structure is readily observed in scanning electron micrographs. The object, then, is to use the maximum resist thickness which can be thoroughly exposed within a 100 μs dwell time. Resist thickness of 55-60 nm appears to be the best compromise.

Ga$^+$ Contamination. For 80 μs dwell time at a beam current of 3 pA, about 1500 Ga$^+$ ions are used to expose each site. Thus even if all Ga$^+$ ions remain on an exposure site after development (a highly unlikely situation), the maximum possible contamination in a 60 nm diameter, 20 nm height Ag cylinder (containing more than 3 x 10^6 atoms) is less than 0.05%. Therefore, although bulk Ga is known to have an absorption peak between 500-600 nm, its effects on optical spectra of noble metal nanoparticles prepared by FIB lithography should be negligible.

Comparison with EBL. IBL was used for the simple reason that an appropriate e-beam writer was not available at Vanderbilt during this research. During the years we have used IBL, some advantages of EBL have become apparent:

1. The penetration depth of electrons in PMMA is hundreds of nm; thus EBL does not suffer the resist thickness constraint inherent to IBL.

2. Whereas only 10^3 ions are used to expose a site, some 10^5 electrons are typically used. Better statistics yields smoother edges of exposed regions.

3. With EBL, some fine control over particle diameter is possible, as demonstrated by Gotschy *et al.* [8]. Increasing the electron dose yields larger di-

ameters. This has not yet been shown with IBL, and could be difficult to do because increasing the FIB dose significantly would increase milling effects which we wish to avoid. For doses between 60 and 120 μs (an admittedly narrow exposure range), we have not observed significant particle size differences. Changing the focus of the beam has a greater chance to affect particle size, but this is usually inadvisable for technical reasons. Stigmation in the FIB is known to give skewed particle shapes, and defocusing likely would have a similar effect on the size.

4. *No* Ga^+ contamination is preferable to *any* contamination, however minimal.

5. In IBL the FIB is pushed to its lower limits of exposure; the instrument is not optimal for this application.

6. The FIB is primarily a milling tool, and as such the heavy ions used could conceivably alter the underlying substrate morphology.

7. FIB systems generally require a mechanical stage with eucentric rotation capability for milling purposes. EBL systems do not have this requirement; hence they are more amenable to interferometric stage controllers, which allow fine control over the "stitching" or alignment of adjacent patterns.

Those points notwithstanding, IBL has proven to be quite satisfactory in constructing nanoparticle arrays. Scanning electron microscopy (SEM) images of IBL nanoparticles compare favorably with many literature images of nanoparticles of various shapes prepared by EBL.

Furthermore, the fact that the FIB is best used as a milling tool gives IBL one significant potential advantage over EBL. As nanoscale fabrication methods progress, it

may prove useful to combine the more familiar capability of the FIB for direct sputtering of substrates with lithographic techniques to create nanoscale structures that require both aspects of the FIB.

3.2 Structural Characterization

Nanoparticle arrays were characterized by scanning electron microscopy (SEM, Hitachi S4200) and atomic force microscopy (AFM, Digital Instruments Multimode III). AFM was done in TappingMode. The only nonstandard AFM parameter used was a 3% peak offset of the tapping resonance frequency.

3.3 Ti:sapphire Laser

Second-harmonic generation experiments were performed with a commercial Ti:sapphire laser (Kapteyn-Murnane Laboratories, Boulder, CO). The Ti:sapphire crystal is pumped by 4.5 W of 532 nm light (Coherent Verdi V6) and produces ultrashort pulses at ~ 93 MHz in the 800-nm region, tunable over a considerable range. With external prisms the laser pulse may be compressed to nominal pulse duration 12 fs; however, for all experiments in this work the pulse duration was typically 50 fs, as demonstrated by the second-order autocorrelation trace shown in Fig. 3.2. The trace was acquired by second-harmonic generation in a potassium diphosphate (KDP) crystal using an interferometric autocorrelator. Details of laser parameters are noted as required in later chapters.
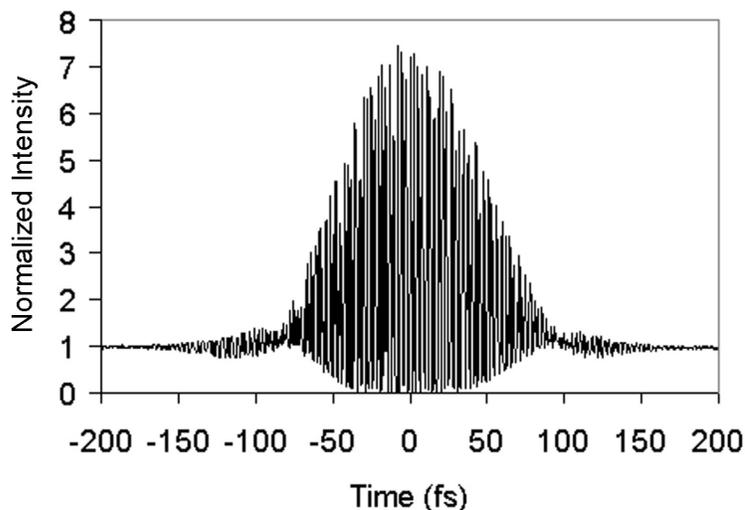
Figure 3.2. Ti:sapphire laser second-order autocorrelation trace. Pulse duration is approximately 50 fs.

3.4 Angle-Resolved Confocal Fiber Microscope

3.4.1   Description of Apparatus

Several optical measurement apparatus were used in this research, all having similar design and purpose. The general concept was to be able to illuminate a nanoparticle array from any angle and measure the scattered or transmitted light at any other angle.

We now describe the most general apparatus. Figure 3.3 shows a schematic of the setup. Incident light (along the z-axis) is focused onto the sample by lens L_F. The sample mount consists of a two-axis positioner with axes $S_{\parallel}$ and $S_{\perp}$, mounted on a rotating stage S_R, mounted on a three-axis positioner with axes $S_{X,Y,Z}$. The sample is mounted vertically. The detector arm is mounted on a rotating stage D_R. A confocal fiber microscope is mounted on the detector arm using another three-axis positioner with axes $D_{X,Y,Z}$. The microscope assembly consists primarily of a microscope objective and a beamsplitter cube reflecting light to a CCD camera and transmitting light to the aperture

45
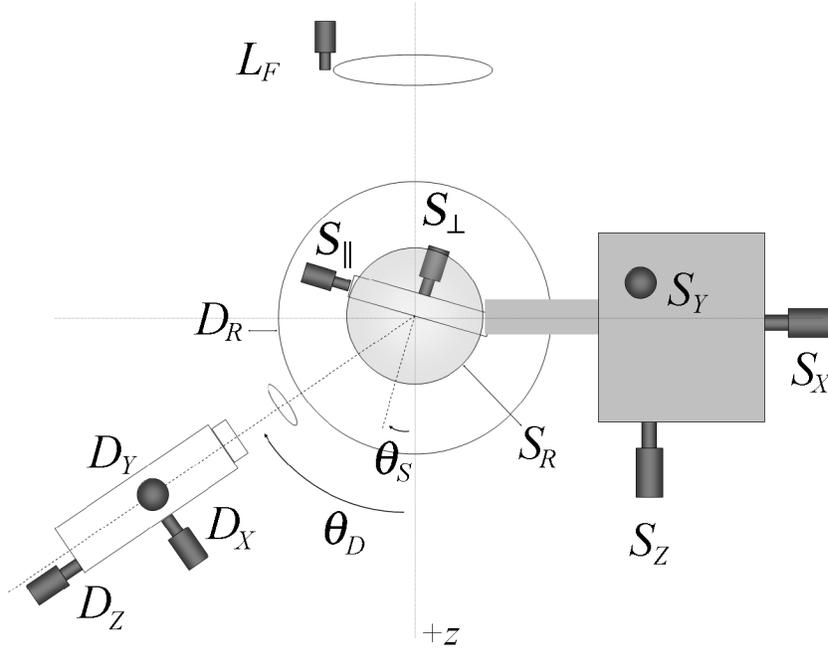
Figure 3.3: Schematic of dual-angle optical measurement system, top view.

of an optical fiber. Between the objective lens and the beamsplitter cube various optical components may be placed (irises, pinholes, filters, polarizers) as needed.

Variations on this design will be described in the experimental details.

3.4.2 Alignment Procedures

The alignment of any system with so many adjustment micrometers is necessarily complicated. The rotating stages S_R and D_R, which are not mechanically coupled in any way, must have their axes of rotation aligned to better than ~50 μm (*i.e.* the size of an array). The laser beam must also intersect the two axes in a point, again to better than 50 μm. In this section we describe the alignment procedure for the system.

The substrate and detector rotation angles θ_S and θ_D are defined with respect to the z-axis (incident light wavevector). $\theta_S = 0°$ when the sample normal points along the $+z$-

46

axis; in this orientation the light enters from the rear of the substrate. $\theta_D = 0°$ when the detector directly faces the incident light. With this convention, $\theta_S = \theta_D$ signifies that the detector is oriented normal to the substrate.

The alignment steps are as follows:

1. Before beginning sample stage alignment, the laser beam and the detector micrometers should be approximately aligned to intersect the rotation axis of D_R. Laser alignment is aided by appropriately placed irises.

2. $S_\perp$ must first be aligned so that the sample plane intersects the sample rotation axis S_R. $S_\perp$ should be adjusted at $\theta_D = 0°$ such that when θ_S is rastered about 0°, the sample region of interest (ROI) is not laterally displaced. (The ROI can be an array or a random substrate flaw). Note that the alignment array should be centered in the camera.

3. S_X may then be approximately aligned by setting $\theta_S = 90°$ and adjusting S_X so that the laser beam grazes the surface, as observed with the camera or a piece of paper. D_Z (the detector focus) may then be aligned at $\theta_D = 90°$.

4. Returning to $\theta_S = \theta_D = 0°$, align S_Z until the sample is in focus. At this step, the ROI should be in focus and centered on the camera screen for both $\theta_S = \theta_D = 0°$ and $90°$. If it is not, this indicates that D_X is misaligned (provided that $S_\perp$ has been adjusted properly) such that the microscope is not pointing at the true center of rotation D_R.
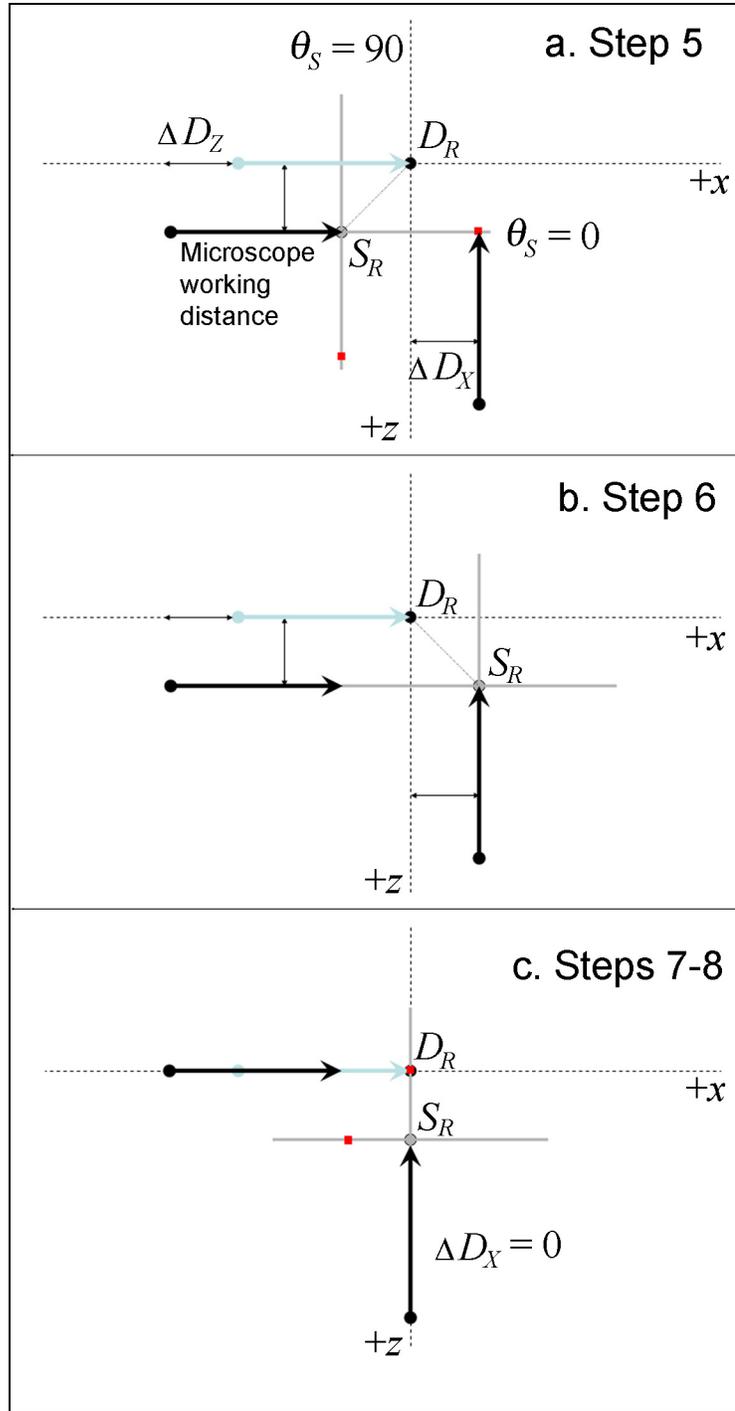
Figure 3.4: Alignment correction diagrams showing the position of the detector and sample relative to the detector rotation mount after each step. Thick black arrows represent detector microscope. Blue arrow represents the goal of alignment. Red squares show where detector is pointing for un-centered cases. a) Sample is in focus at 0° and 90° but un-centered at 0°. b) After adjusting S_X. ROI is centered on detector arm for both orientations, but defocused at 90°. c) After correcting S_X and D_X at 0°. Sample is defocused and un-centered at 90°, but focusing will correct D_Z.

5. To correct D_X: First, adjust S_X, S_Z and D_Z so that the sample is in focus at both 0° and 90°, but the ROI is not centered in one orientation (see Figure 3.4a for symptom diagram). Note the micrometer positions.

6. By adjusting *either* S_X *or* S_Z, one can make the ROI appear centered in both orientations, but in one orientation it will appear unfocused (see Figure 3.4b for symptom diagram). Note the new position for the micrometer that was moved.

7. In both cases (steps 5 and 6) the $S_{X,Z}$ are *both wrong*; but, conveniently, they are wrong by the same amount. In step 6, for example, the chosen micrometer was moved exactly to the *opposite* side of the correct position. Calculate the correct position (midway between the two recorded points) and move the micrometer there. That micrometer should now be in the correct position.

8. D_X should then be adjusted by the same amount (and direction) as the micrometer in step 7. Now D_X is correct. (See Fig. 3.4c.)

9. Switch to the other orientation and adjust D_Z until the sample is in focus (although the ROI will not be centered); the adjustment should be the same distance as the other steps.

10. Switch back to the first orientation and "focus" with the remaining $S_{X,Z}$. Again, the adjustment should be the same distance as the others. At this point the alignment should be very close to correct, and fine-tuning may be done iteratively following the algorithm of steps 5-9.

11. It may prove necessary to realign the laser at this point.

When the system is fully aligned, the sample may be moved in its own plane by the micrometers $S_{||}$ and S_Y (horizontal and vertical respectively.) In an ideal world, the only regular adjustment necessary would be $S_\perp$, when mounting a new sample. The reader may judge for himself whether we live in an ideal world.

CHAPTER IV

RAPID TARNISHING OF Ag NANOPARTICLES

Chemical activity in silver nanoparticles exposed to laboratory air can make interpretation of optical scattering and extinction spectra problematic. We have measured the shift of the plasmon polariton frequency of arrays of silver nanoparticles with increasing exposure to ambient laboratory air. The resonance peak wavelength shifts 65 nm in 36 hours (1.8 nm/hr). We show by scanning Auger spectroscopy that the shift is due to contamination from sulfur, most likely chemisorbed on the surface. The rate of corrosion product growth on the nanoparticles is estimated to be 3 nm per day, 7.5 times higher than that of bulk Ag under the same conditions.[**]

4.1 Introduction

The LSPR of silver nanoparticles is stronger than that of the other noble metals, and has its peak amplitude in vacuum at a higher frequency [3]. The former characteristic makes silver an ideal candidate for use in applications that exploit the plasmon-polariton resonance. The latter uniquely qualifies silver nanoparticles to respond in the violet region of the visible spectrum, since the Mie resonances [2] of gold and copper particles typically appear in the green and red regions and most deviations from the ideal case of spherical particles in vacuum result in a redshift of the SPP wavelength. In addition, silver has strong interband transitions in the visible, and thus is an excellent material for studying the interplay between single-electron and multi-electron excitations (*e.g.* inter-

_____

[**] The content of this chapter has already been published in *Applied Physics B*, 2005 [49].

51

band transitions and SPPs) [50]. However, the utility of silver for nanophotonics applications is compromised by its lack of chemical stability in ambient conditions, leading to damping of the resonance by multiple mechanisms, such as dielectric damping and chemical interface damping (CID) [51, 52].

Silver is widely known to corrode or tarnish in air [53-57], and sensitivity to gas exposure has been measured [58] and explored for gas sensors [59]. Surprisingly, thus far there has been no systematic study of simple corrosion effects on silver nanoparticles in the laboratory environment [A. Leitner, personal communication]. In this chapter we present measurements of the optical shift of the plasmon resonance peak in lithographically-prepared arrays of silver nanoparticles with increasing exposure to laboratory air. We demonstrate by scanning Auger spectroscopy that this optical shift is due to chemisorbed sulfur on the nanoparticles. We estimate the rate of corrosion in the silver nanoparticles using our optical data along with optical constants of silver sulfide from the literature [53] and reasonable physical assumptions.

4.2 Experimental Methods

The ordered arrays of silver nanoparticles used for these experiments were fabricated using IBL as described in Chapter III. Silver was deposited by PLD. In this work all arrays had particles arranged in a 2D square lattice unless otherwise stated. Array size was typically 60 x 60 μm^2; particle diameter was typically 60-70 nm. Following liftoff, the samples were stored in small wafer carriers (Entegris 1" single wafer shippers) having a capacity of about 1 cm^3. The wafer carriers have a screw-tight cover that provides a good seal.
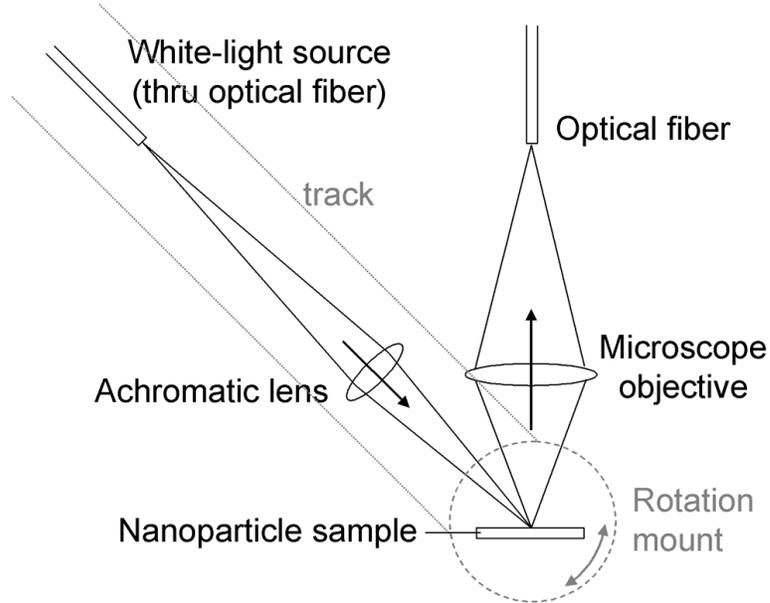
Figure 4.1: Schematic of the confocal microscope used in the optical experiments. Light collected with the microscope objective is sent to a spectrometer (not shown) through the optical fiber, which defines the confocal field of view.

Optical scattering measurements were performed with a custom-built confocal microscope (Fig. 4.1). The apparatus is designed with a light input arm whose center of rotation is the sample region of interest, so that light may be input from virtually any angle of incidence above or below the sample plane. A fiber coupler on the arm permits illumination by either monochromatic or broadband sources. For these experiments we used a fiber-coupled 20 W tungsten-halogen white-light source (ASBN-W-020R, Spectral Products, Putnam, CT). Unpolarized light is incident from 45° above the sample plane and is focused onto the sample using an achromatic lens.

The collected light is sent to a spectrometer (Acton SpectraPro 300i) for spectral analysis, with typical integration time 1 minute. The spectrometer software interface features a built-in time delay that was used to record a complete spectrum, normalized to the

output of the lamp, every 15 minutes over a time span ranging from hours to days for different arrays. The raw spectra were smoothed using an adjacent-averaging smoothing routine in the data analysis software (Origin); the number of adjacent data points used for averaging varied from 25 to 50 for different spectra.

Auger microanalysis of some of the arrays was performed at the High Temperature Materials Laboratory at Oak Ridge National Laboratory, using a Phi 680 Scanning Auger Nanoprobe. The primary electron beam was provided by a field emission source operated at a beam energy of 20kV and beam current of 10nA. This probe beam was focused to a spot size of ~20nm and the Auger electrons emitted from the sample were detected using a cylindrical mirror analyzer. Electron micrographs were obtained at Vanderbilt University using a Hitachi S4200 Scanning Electron Microscope equipped with a cold field emission electron gun.

4.3 Results

Fig. 4.2 shows the change in the optical response as a function of exposure to laboratory air for a 2D square array of annealed silver nanodisks (20 nm height, 60 nm diameter) with grating constant 162 nm. Fig. 4.2a shows selected spectra from a series that was taken every 15 minutes over a period of 36 hours. The redshift, broadening and weakening of the resonance over time are clearly demonstrated. The peak amplitude decreases nearly one order of magnitude. In Fig. 4.2b the resonance peak wavelength position as a function of time is plotted. The resonance position redshifted 65 nm in 36 hours nearly linearly, giving a shifting rate of ~1.8 nm/hr.
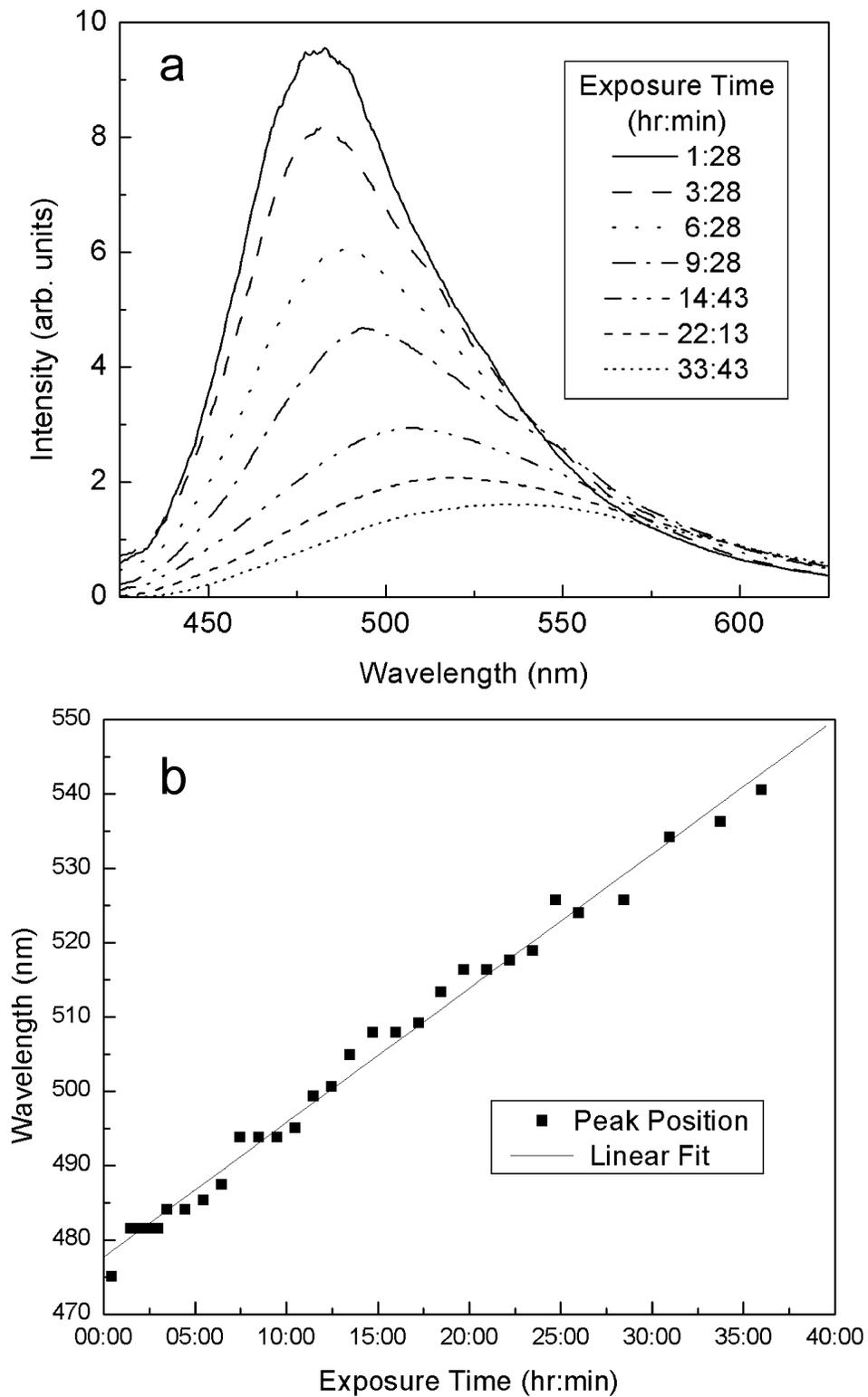
Figure 4.2: (a) Selected SPP spectra from an array of silver nanoparticles with increasing exposure to laboratory air. (b) Redshift of the resonance peak with increasing exposure. Shifting rate is 1.8 nm/hr. Grating constant of array is 162 nm.
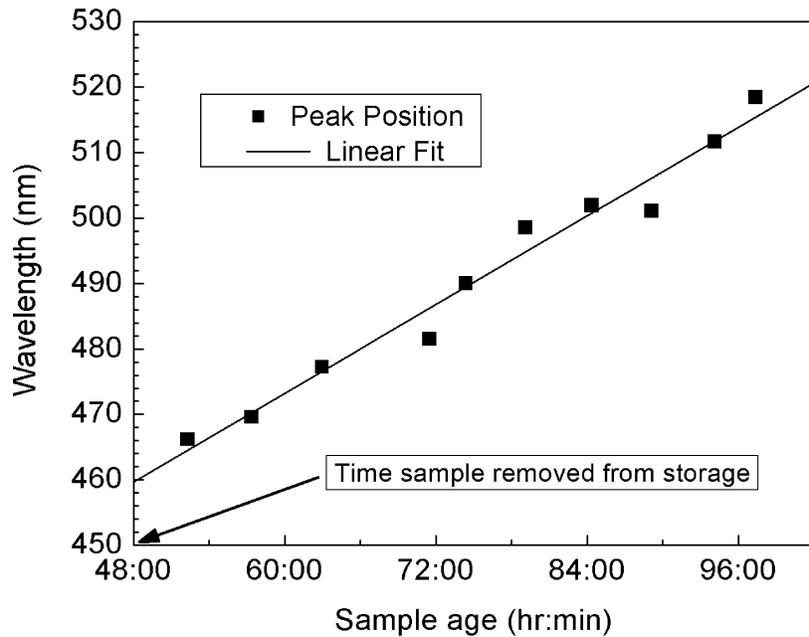
Figure 4.3: SPP resonance shift. Note that the resonance position after removal from storage is comparable to the initial resonance of the array in Fig. 4.2b even though this sample is 2 days older. Shifting rate is 1.25 nm/hr. Grating constant of array is 147 nm.

We observed that arrays sharing a particular grating constant on samples that were stored in the 1" wafer carriers always seemed to have approximately the same initial resonance position immediately after being removed from the carriers, independent of the time spent in storage. Once placed on the microscope stage (open to ambient), however, the arrays began to shift dramatically. Fig. 4.3 shows the shift of one such array (not annealed, grating constant 147 nm) left in storage for 2 days before being placed on the microscope stage. Here the shift is less dramatic but still pronounced (~1.25 nm/hr). The initial resonance position is similar to the array in Fig. 4.2 although the delay between sample preparation and optical characterization was much larger.

A capping layer of dielectric material (200 nm, PMMA) prevented any further shift in the optical properties over an appreciable period. Fig. 4.4 demonstrates that spectra
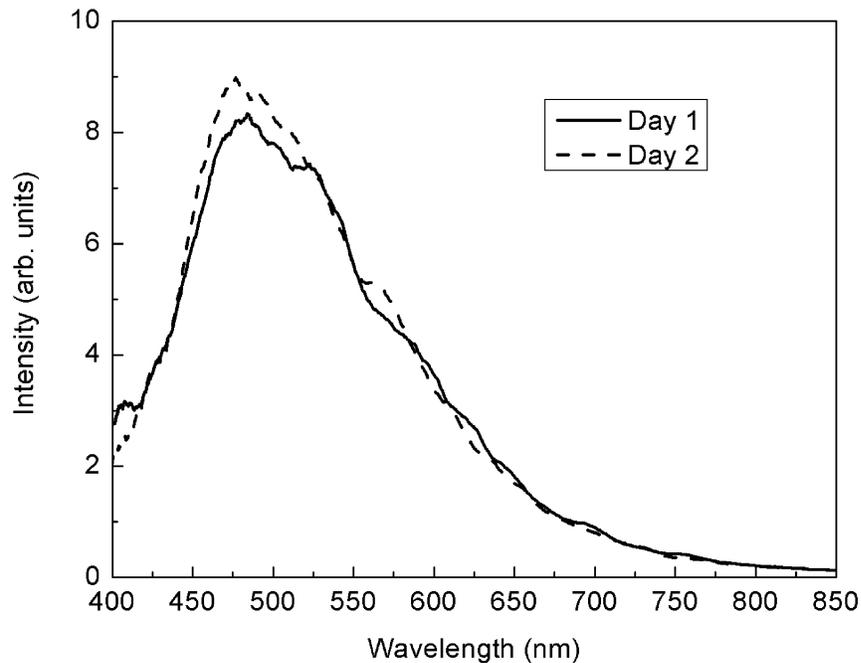
Figure 4.4: Effect of dielectric coating. Spectra were taken from the same PMMA-coated array on consecutive days with 19 hours elapsed between spectra. Spectra have been smoothed with adjacent-averaging process. The resonance position, amplitude and width were preserved.

taken from the same capped array on successive days had virtually identical peak position and line shape.

The results of Auger spectroscopy of silver nanoparticles exposed to ambient are shown in Fig.4.5. The nanoparticle "dimer" shown in Fig. 4.5a constitutes a basis set of a larger 2D lattice structure fabricated by IBL. The Auger spectrum reveals the presence of sulfur on the silver nanoparticle. The indium, tin and oxygen signals are reduced at the nanoparticle locations because the measuring technique is highly surface-sensitive. There is a slight increase in the carbon peak at the nanoparticle.

Over the time intervals given in Figs. 4.2 and 4.3, the nanoparticles do not change their shape significantly. Fig. 4.6 shows electron micrographs of a region of an array (a)
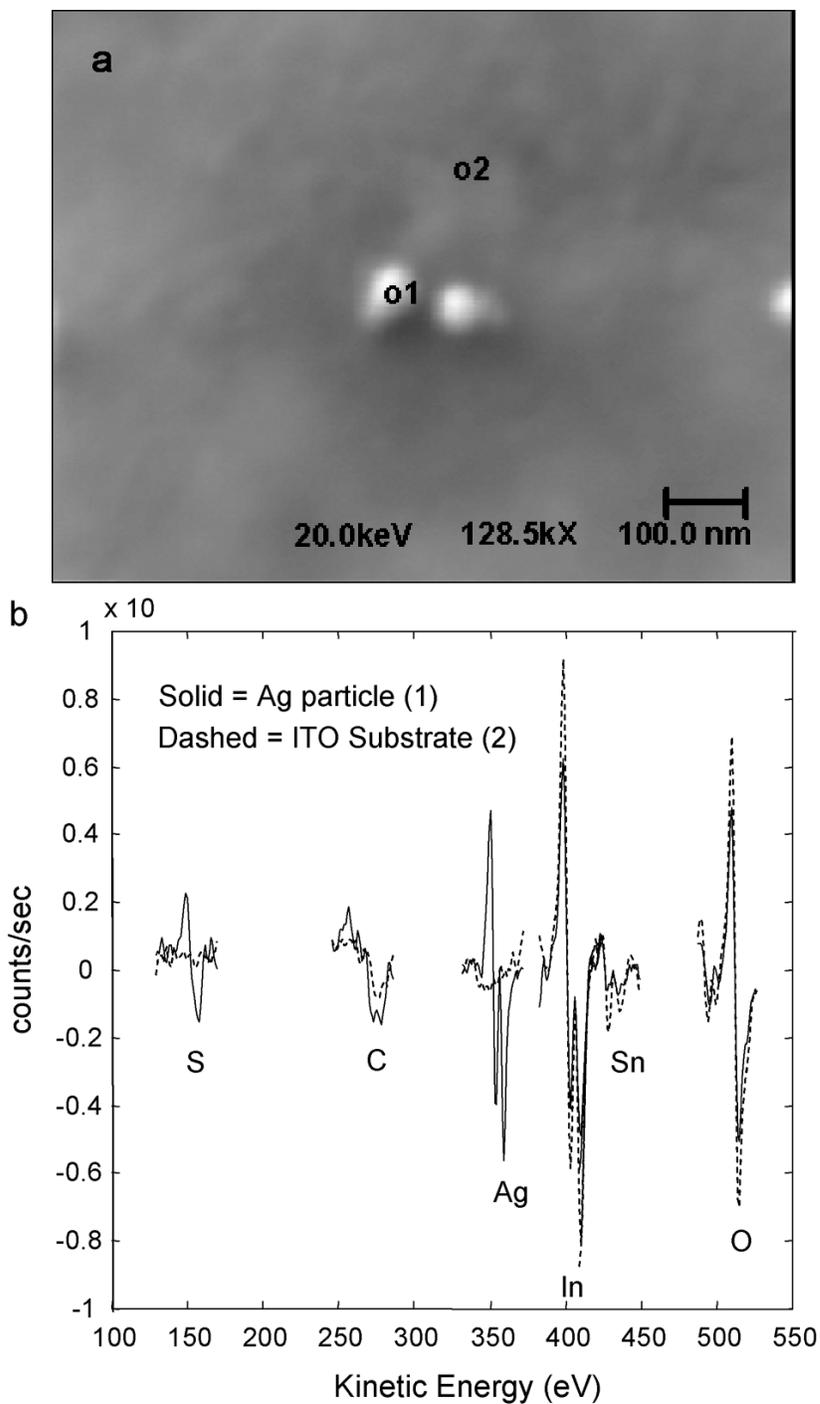
Figure 4.5: (a) Electron micrograph of Ag nanoparticle "dimer" analyzed with Auger spectroscopy. (b) Auger spectra of regions indicated in (a). Sulfur is found with silver on the particle.
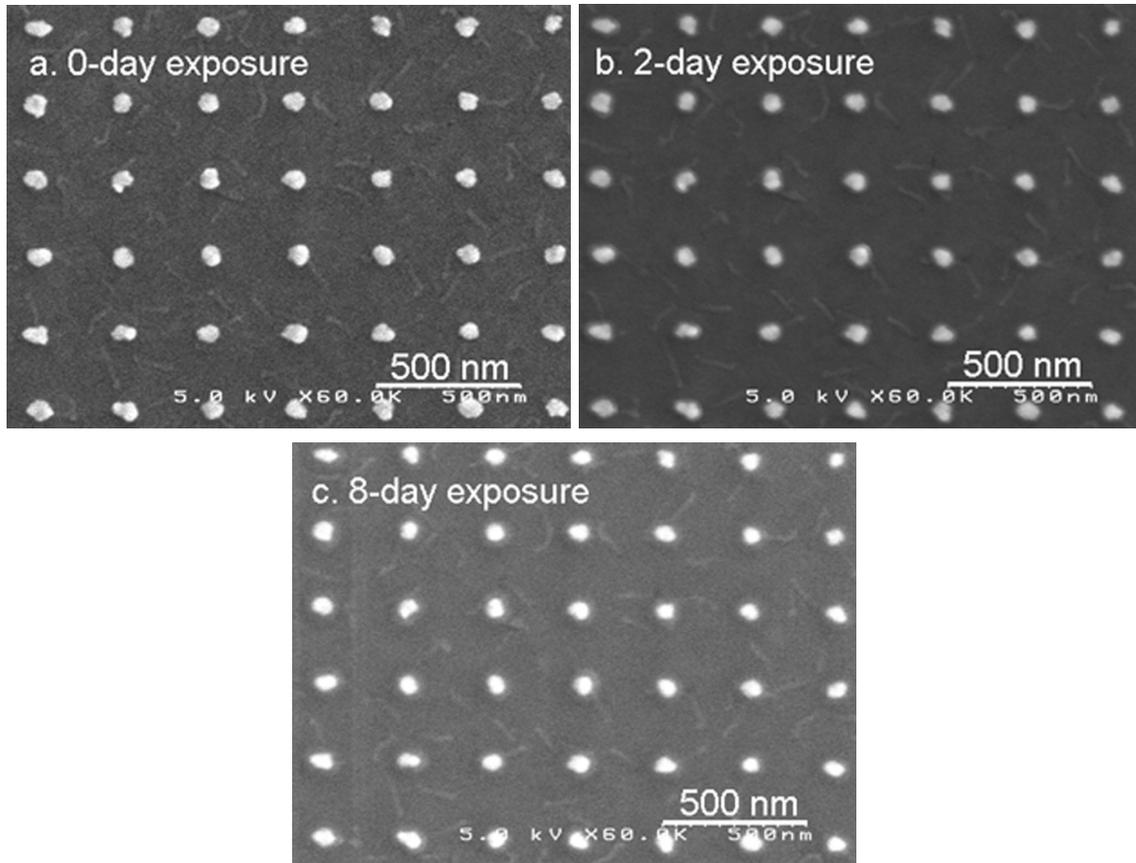
Figure 4.6: Electron micrographs of a particular set of Ag nanoparticles on ITO-coated glass at various exposures. Particles are 65 nm diameter, 22 nm nominal height; grating constant is 300 nm. (a) Immediately (<1 hour) following the liftoff process. (b) After two days exposure to laboratory air. (c) After eight days exposure to laboratory air. The halo that appears around the particles in parts (b) and (c) is an artifact of sample charging in the SEM and is not necessarily representative of the scale thickness; particles elsewhere in the same array that were not previously imaged with the electron beam do not exhibit the halo. The exposure for this sample took place with average outdoor temperature ~15° C and RH ~65%, so scale formation should proceed more quickly than for the samples measured in Figs. 3.2 and 3.3.

immediately following sample preparation, (b) after two days of exposure to laboratory air, and (c) after eight days of exposure to laboratory air. The shape of the particles is preserved even after eight days of exposure; the only observable difference is a slight rounding of particle edges.

4.4 Discussion

The experimental results unambiguously point to chemisorption of sulfur (tarnishing) as the cause of the redshifts in the LSPR spectrum. Lamp-induced shifts (*i.e.* local annealing) are implausible as the intensity of the source is rather low and the temperature of the sample does not change during the hours over which the sample is under illumination. Silver is known to corrode in air by chemical reaction with ambient levels of hydrogen sulfide gas (H_2S, 0.03-5 ppb) and carbonyl sulfide (OCS, 0.5 ppb) to form silver sulfide (Ag_2S) [57]; the process in both cases is significantly enhanced at high relative humidity (RH). H_2S corrosion is also enhanced in the presence of nitrogen dioxide (NO_2) [60]. As the background ambient concentration of H_2S is an order of magnitude lower than that of OCS, and we do not believe that we have any significant H_2S sources in the laboratory, it is probable that OCS plays a larger role than H_2S in our case [56]. It may be anticipated that corrosion in particles will occur more rapidly than in thin films due to the much larger surface/volume ratio. The fact that the optical properties were preserved when stored in small-volume (1 cm^3) containers strongly suggests that the corrosion process was reactant-limited in these cases. The fact that coating the nanoparticles with a dielectric (PMMA) prevented further change in the optical properties strongly suggests a reaction with ambient as the cause of the shift. Gotschy *et al.* [8] reported a similar experiment with coating an array with PMMA, but focused solely on the redshift of the resonance relative to the uncoated array rather than on any preservative effect of the coating. Finally, the scanning Auger results show that the nanoparticles were preferential sites for sulfur accumulation. The slight increase in the carbon peak may indicate some minor
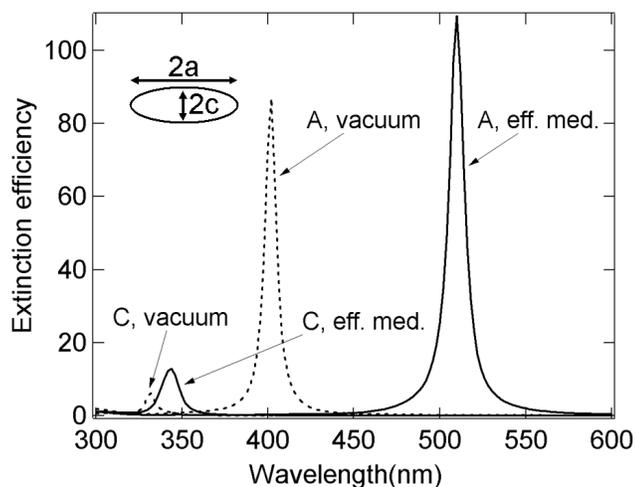
Figure 4.7: Calculated extinction efficiencies, in the quasistatic approximation, of surface-parallel and surface-normal modes of oblate Ag spheroid (height 2c = 20 nm, diameter 2a = 60 nm), embedded in vacuum $(\varepsilon = 1)$ and an effective medium taking account of the substrate $(\varepsilon = 2.3)$ (as parameterized for the nearly identical sample geometry in [8]). 'A' refers to surface-parallel mode, 'C' to surface-normal mode.

preferential hydrocarbon adsorption; it may alternately indicate the presence of PMMA fragments left over from the development and lift-off processes.

Our particles are best approximated as oblate spheroids. Oblate spheroids in general exhibit two resonances: a surface-parallel mode with two symmetric components, and a surface-normal mode. We observe only one peak in our spectra; this corresponds to the surface-parallel mode. For an oblate spheroid having height 20 nm and diameter 60 nm, embedded in an effective medium having $\varepsilon = 2.3$ [8], the surface-normal mode may be calculated (using the quasistatic approximation) to occur at ~350 nm, as demonstrated in Fig. 4.7. The surface-parallel mode occurs at ~500 nm, consistent with our observations. The much weaker surface-normal mode was not in the range of the spectrometer for these experiments. We also note that since we illuminate at 45° with unpolarized light, only about a fourth of the incident light is coupled to the surface-normal mode to begin with.

Changing the nanoparticle interface from silver/air to silver/silver sulfide "scale" of increasing thickness results in redshift and damping of the resonance. A Mie calculation (MQMIE 2.4, Michael Quinten, Wissenschaftlich-technische Software) of the scattering of Ag spheres coated with a shell of varying thickness of Ag_2S demonstrates this qualitatively, and we may draw some limited quantitative bounds from it as well. The Mie calculation makes some obvious but serious approximations. Among other assumptions, particles are modeled as non-interacting spheres in air rather than interacting oblate spheroids on a supporting substrate; step-function boundaries between the various dielectric spatial regions are assumed, which is certainly not the case in our experiment; and chemical interface damping (CID), which represents an *additional* damping mechanism beyond the simple dielectric damping of the Mie model, is neglected entirely. Nevertheless, we can simulate the experimental trends sufficiently to make the sulfidation argument plausible.

Fig. 4.8a shows the scattering efficiency for Ag spheres of 25 nm initial radius. We make the simplifying assumption that a given outer shell thickness of Ag reacts *completely* to form the Ag_2S scale. Optical constants for Ag are taken from Johnson and Christy [40]; optical constants for Ag_2S are taken from Bennett *et al.* [53]. Due to the difference in density between Ag (10.5 g/cm^3) and its sulfide (7.2 g/cm^3) [61], the corresponding scale thickness is significantly (~50%) larger than the original thickness of Ag that reacted to form the scale. For example, for an initial particle radius of 25 nm, a conversion of 1 nm Ag results in a scale layer of 1.6 nm (the correspondence with increasing shell thickness is very slightly sub-linear). The amplitude of the scattering efficiency is very sensitive to the increasing scale thickness; hence the log-linear plot in part a).
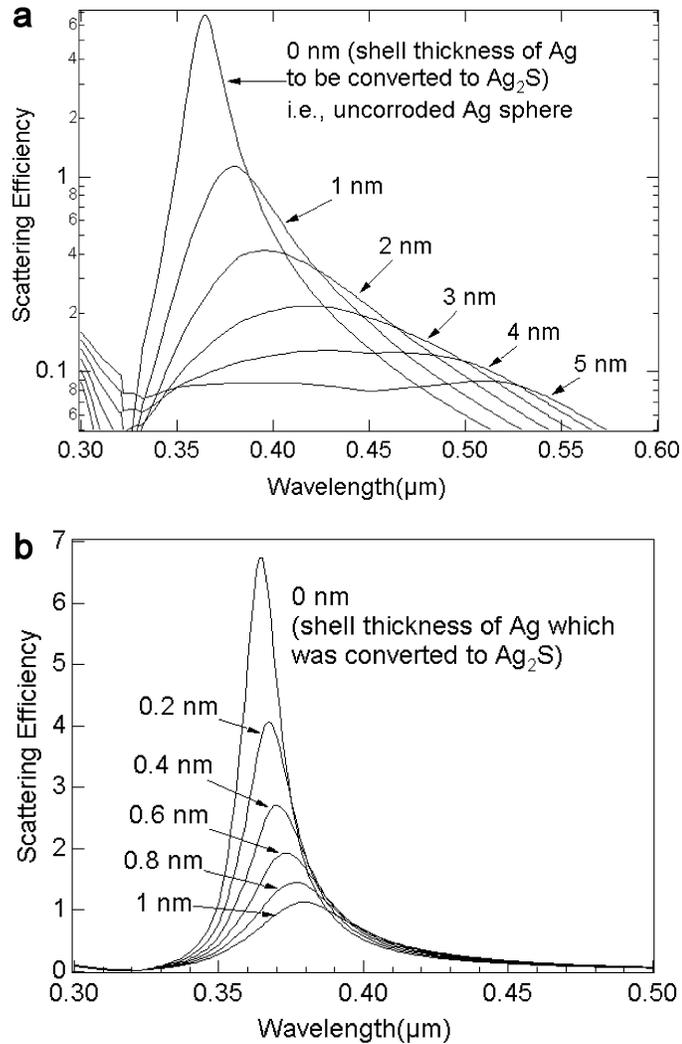
Figure 4.8: Calculated Mie scattering efficiency of Ag spheres with Ag_2S shells of varying thickness, in air. Spheres are initially 25 nm radius pure Ag; the corroded shell is assumed to be completely converted to Ag_2S. Thickness values listed are prior to conversion (1 nm Ag $\rightarrow$ 1.6 nm Ag_2S for a sphere of 25 nm initial radius). In part (a), ordinate is plotted on a log scale for clarity. Note different abscissa range in parts (a) and (b).

Notice that when 4 nm of Ag has corroded, a small dip in the peak appears around 450 nm; the dip becomes more pronounced with increasing scale thickness. We observe no such feature in our spectra (compare Fig. 4.2a); this suggests an upper limit of order 6 nm of scale growth on our particles. In fact, the damping behavior in our data is more closely mimicked by much smaller scale thicknesses $\leq$1.6 nm, as shown in Fig. 4.8b).

Our results show behavior similar to the data presented by Stanford on discontinuous thin Ag_2S layers grown in laboratory ambient on roughened evaporated Ag films [54]. Stanford notes that, because the real part of the dielectric function of both Ag and Ag_2S is nearly linear with respect to wavelength in the 300 to 500 nm region, the resonance peak wavelength should shift nearly linearly with increasing thickness for small thicknesses. This result seems to be applicable in the nanoparticle case as well according to the Mie calculation above, although the ratio of the SPP shift to the sulfide thickness increase is much larger in the nanoparticle case as one might expect. Our results indeed show a linear relation between total exposure and wavelength shift; this suggests that for our particles the average scale thickness increased linearly with total exposure over the time intervals analyzed.

A linear increase of sulfide thickness with exposure is consistent with an initial flux-limited growth phase that, at least in the case of H_2S exposure of bulk Ag, extends through the formation of ten equivalent monolayers (ML) of scale [56]. Since OCS results in approximately the same (usually slightly smaller) scale thickness as H_2S for similar exposures, we may safely assume that the sulfide thickness of our nanoparticles is less than ten ML (~5 nm) which corresponds to total exposure of ~1 ppm·hr. This mildly constrains our previous limit. However, if we assume an OCS concentration of 0.5 ppb, in 36 hours we arrive at a total exposure of ~18 ppb·hr. Even if we are near a source of H_2S, with concentration 5 ppb, the total exposure in 36 hours is 180 ppb·hr, still well within the linear growth regime. Furthermore, the experiments in [57] were performed at 92% RH. Our experiments were performed in cold dry months when the indoor RH is much lower. These considerations would place the upper limit of the scale thickness

much lower, at ≤1 nm. Nonetheless, this conclusion would only be accurate if the reactivity of the silver nanoparticles is the same as that of bulk silver. Due to the high surface-to-volume ratio, and the high curvature of the nanoparticle surface, we may expect that the reaction rate is higher for our nanoparticles than for the samples in [57] (as well as the samples in [55]). Since we are in the linear growth regime, we may use our data to estimate the increase in reactivity for the nanoparticles relative to the bulk.

Fig. 4.8b shows the results of a Mie calculation converting up to 1 nm of an Ag sphere of initial radius 25 nm to sulfide scale (scale thicknesses up to 1.6 nm). The peak wavelength shift of 16 nm is much smaller than we measured here. Since the resonance of Ag spheres blueshifts with decreasing radius to a minimum at ~15 nm, the redshift due to the increased dielectric function of the surroundings is partly compensated by the shrinking of the Ag core. (We note that, since our particles are on a supporting substrate – the dielectric effects of which do not change with time – they are not surrounded by scale; thus we would require in general a larger actual scale thickness to achieve the same optical shift as for an imaginary particle which is symmetrically corroded.) A 3-nm-thick shell of Ag converted to scale (4.7 nm Ag_2S) would give an SPP shift of 54 nm, more congruent with our data. We may compare our results to the work of Burge *et al.* [62] which used samples similar to those of Stanford [54]. They reported H_2S concentration of <0.2 ppb, and under atmospheric conditions in their laboratory the Ag_2S growth rate was 0.4 nm per day and essentially linear over the time interval studied (8 days). Since the resonance shift should be approximately linear with respect to thickness, using Fig. 4.2 data with the Mie calculation we estimate that 4.5 nm scale thickness grows in 1.5 days, giving a growth rate of 3 nm per day, which is 7.5 times higher than the thin film

case; low precision is warranted by the crudeness of our Mie model. Recent papers by Haes et al. [10, 11] indicate that the resonance peak shift with increasing dielectric layer thickness is larger in less spherical particles, so in modeling spheres we likely have over-estimated the growth rate by 10-20%. The actual rate may be still lower depending on the relative importance of the dielectric contribution to the SPP shift (compared to, *e.g.*, CID effects).

The rate of corrosion is different for the data in Figs. 4.2 and 4.3. This is explained by different RH during the two experiments. Archived hourly weather observations for Nashville, TN (http://www.intellicast.com) indicate that the average outdoor RH during collection of data in Fig. 4.2 was 68%, while that for Fig. 4.3 was 47%; in both cases out-door temperatures were near freezing, so the percentages scale to room temperature in the same way. Since all our shifts are in the linear regime, and the RH dependence is roughly linear, this accounts for the difference in the shift (1.8/1.25 = 68/47).

Tarnishing of bulk silver is known to create "whiskers" of silver sulfide [55]. From this fact we might expect that sulfidation could produce a distortion of nanoparticle shape. Contrariwise, the electron micrographs of nanoparticle sulfidation in Fig. 4.6 indi-cate that the exposures in these experiments do not cause significant particle deformation – if anything, morphological changes tend toward a more circular profile. This elimi-nates shape changes as an agent of optical redshift; indeed, any increased sphericity would induce a slight blueshift and cause underestimation of the dielectric shift by coun-tering its effect on the measured spectrum. We have not characterized the nanometer-scale crystallinity of the particles under study (*i.e.*, any porosity within the individual nanoparticles which would increase the surface area, yielding an apparent increase in re-

activity). However, the PLD technique is a standard one used by many researchers for creation of nanoparticles and gives results quite similar to evaporative deposition, so we would not expect any significant structural differences between our particles and those of other researchers. Furthermore, the similarity in behavior between the experiments and the Mie calculations supports the qualitative assertion that the tarnishing occurs on the surface of the particles. Thus we expect that researchers studying nanoparticles prepared by similar techniques would measure reactivities similar to those presented here.

4.5 Conclusion

We have studied the chemical instability of silver nanoparticles under ambient conditions. Relatively thin corrosion layers formed by reaction of silver nanoparticles with atmospheric sulfurous compounds lead to significant changes in the optical response over a period of days. The shifts due to tarnishing can be of the same order as shifts due to variation of the grating constant, for example. The optical changes are primarily due to the modification of the dielectric environment of the nanoparticles, with a slight correction to account for the shrinking Ag core; shape changes are relatively unimportant for the particle types and exposures studied. In the linear growth regime, we may use the optical shift to estimate the reactivity of the nanoparticles; the rate of corrosion in Ag nanoparticles is several times higher than in the bulk and can be as high as 3 nm Ag_2S per day, even at low (~20%) indoor RH. The observed changes in the optical properties with time should be representative of ambient conditions in most laboratories and may be used as a benchmark.

CHAPTER V

PERSISTENCE OF GRATING EFFECTS IN ANNEALED Ag NANOPARTICLE
ARRAYS

We measure the optical characteristics of ordered arrays of silver nanoparticles using a frustrated-total-internal-reflection technique. Momentum conservation dictates that different wavelengths are dispersed at different angles, and the angular characteristics are dependent upon the grating constant. The strength of the diffraction conditions is demonstrated in a frustrated total-internal-reflection geometry using a nanoparticle array which has been annealed to destroy the individual particle quality. The wide particle-size distribution gives rise to extreme inhomogeneous broadening of the LSPR. The finite numerical aperture of the detector reveals the presence of strong diffraction by a cutoff wavelength that depends upon the grating conditions.

5.1 Introduction

The concept driving the emerging field of nanophotonics is to use nanoscale features to control photons, whose characteristic length scale is many times the size of the relevant structural features. For instance, extensive research over the past decade sought to exploit the possibility of using metal nanoparticle chains as photonic circuitry to localize and propagate optical signals [63-65]. The dependence of the LSPR position and width on nanoparticle spacing has also been studied using two-dimensional arrays and particle pairs of gold and silver. Felidj and coworkers demonstrated that the position and width of the LSPR for two-dimensional arrays of gold nanoparticles depends upon the lattice

constant of the array as well as the individual particle sizes [66]; Haynes and coworkers also studied the array spacing dependence for gold and silver disk and trigonal prism arrays [67]. Rechberger and coworkers studied the simpler case of pairs of gold nanoparticles with separation ranging from touching to three diameters apart; they found good agreement with a simple model of interacting dipoles [36]. Gunnarsson and coworkers studied similar silver particle pairs and achieved similar results [37]. But ordered arrays of noble metal nanoparticles provide a particularly interesting method of controlling light not only because the LSPR varies with interparticle spacing, but also because the order contributes strong spatial phase coherence. Put another way, the far-field coupling could be as useful as the near-field coupling.

Some comparisons between near-field and far-field coupling have been explored. Linden and co-workers have shown that coupling of array resonances to guided modes in a dielectric waveguide results in enhanced transmission for certain wavelengths, depending on the array parameters [68]. Lamprecht and coworkers also investigated the effects of far-field coupling on the plasmon dephasing time, showing that as successive diffracted orders become allowed the radiative damping of the LSPR increases [14]. Still – perhaps because the topic of diffraction gratings seems mundane – relatively little work has been done to demonstrate or take advantage of the diffractive character of these two-dimensional gratings as such. In this chapter we present a simple, explicit demonstration of the diffractive character of metal nanoparticle arrays, and consider this as a method for controlling light. In succeeding chapters we will consider ways to exploit the diffractive character in the nonlinear intensity regime.

We have measured the optical response of two-dimensional arrays of silver nanoparticles by a frustrated total internal reflection (FTIR) technique. Particularly when particles are small and spacings are large, it is difficult to achieve good signal in a traditional normal-incidence extinction measurement. FTIR geometry improves the optical signal to such an extent that the technique has been used to study the far-field optical spectra of single nanoparticles [69]. The details of the FTIR measurement allow us to demonstrate that the method by which light is re-radiated from the arrays into the previously forbidden region is governed by the properties of the surrounding media. It also depends on two other controllable experimental parameters: the angle of the incident light, and the geometry of the arrays.

5.2 Experimental Methods

Silver nanoparticle arrays were fabricated by IBL as described in Chapter III. Ag was deposited by PLD to 20 nm mass thickness. In the annealing step, the sample was annealed in the PLD vacuum chamber with a low pressure of argon gas at 350°C for 30 minutes.

We set up our FTIR experiment on the platform of a scanning near-field optical microscope (WITec AlphaSNOM) in a confocal arrangement (Fig. 5.1). The experiments described in this chapter do not take advantage of the optical near-field measurement capabilities of the instrument, but we note that nothing in our setup precludes near-field measurements with FTIR geometry. The sample is placed on a rhomboid glass prism
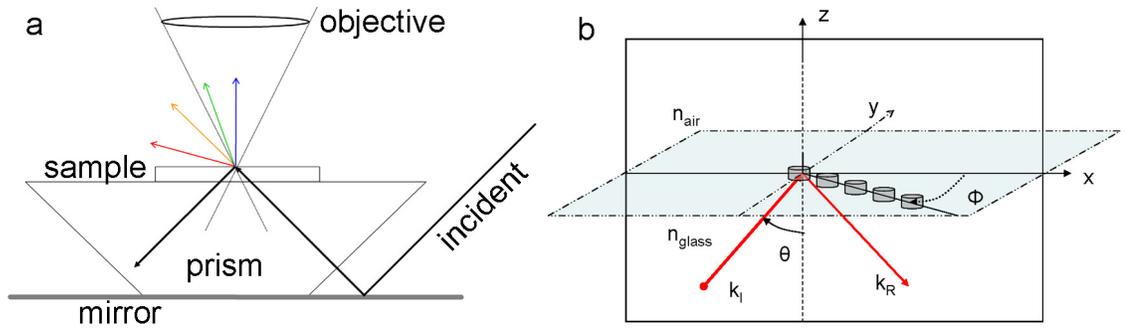
Figure 5.1: Frustrated total-internal-reflection setup. a) Schematic of apparatus. b) Array geometry, showing array rotation angle. Only a portion of one row of nanoparticles is depicted for clarity.

with index-matching fluid to remove any optical interface between the prism and the sample. The prism rests on a mirror. We align the light source and optics on a post system. To prevent dispersion in the prism, the post is carefully aligned so that the light reflects off the mirror at the angle that is normal to the relevant face of the prism. In the following measurements, the light source was a fiber-coupled tungsten lamp emitting in the visible and near-IR. All measurements were done with polarization perpendicular to the plane of incidence (*s*-polarization). The sample may be rotated in-plane to change the projection angle of the wavevector relative to the array axes (see Fig. 5.1b). Light is collected above the sample with the microscope objective of the SNOM. The collected light is sent to a spectrometer through an optical fiber.

5.3 Results

To demonstrate the strength of the diffraction effect, the curves in Figure 5.2 were measured from a sample annealed in argon at 350° C for 30 minutes. During annealing, silver from the particles diffused and formed smaller clusters surrounding the original particles, and the size distribution broadened (see inset). Figure 5.2 shows data taken
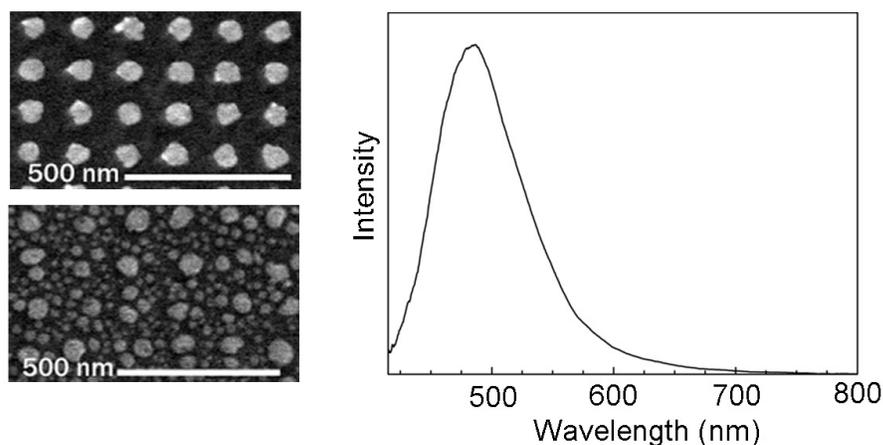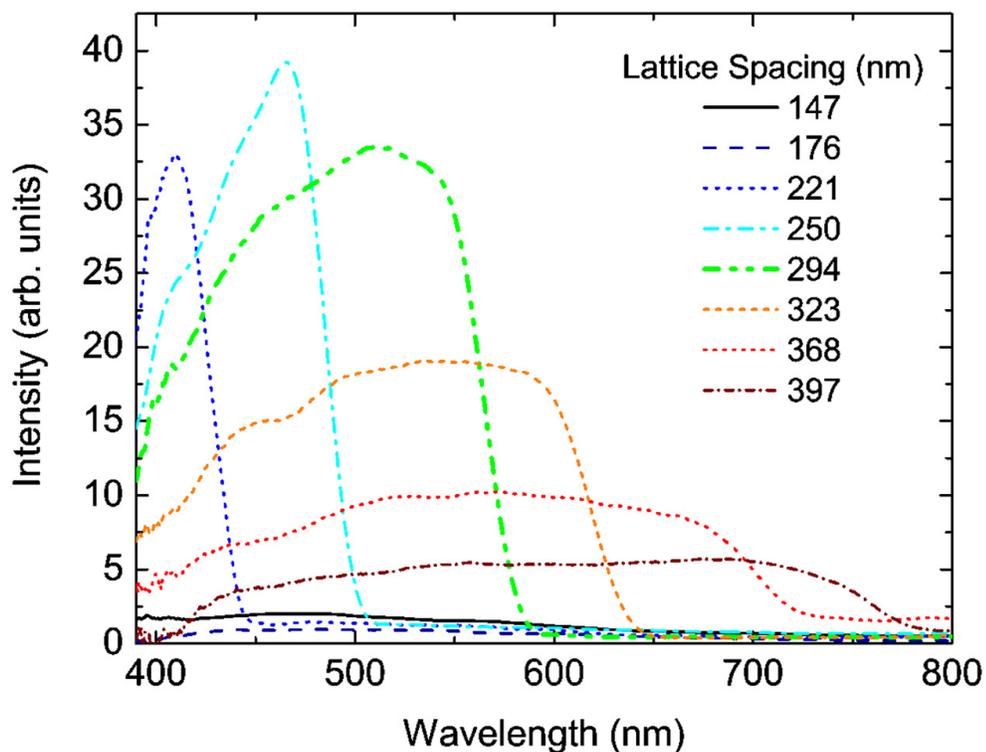
Figure 5.2: TOP – Scattered spectra from several annealed particle arrays with different lattice constant. The light is collected with a microscope objective of numerical aperture 0.8 and normalized to the particle areal density and the spectral profile of the source. LOWER LEFT – Electron micrographs of array with 147 nm periodicity before and after 30 minute anneal in argon at 350° C. LOWER RIGHT – LSPR spectrum of non-annealed array with 147 nm period and silver nanoparticles with 60 nm diameter and 25 nm height, illuminated with white light at 45° from the normal; scattered light was collected in reflection mode (as in Chapter IV) with a NA = 0.25 lens normal to the array.

with the array aligned with the light projection along an axis, *i.e.* 0°. Similar measurements were taken at 45° and 90° array rotation angles. Sharp cutoff wavelengths are observed in the spectra at each rotation angle. In addition, we observe a broad resonance on the low-wavelength side of the cutoffs.

5.4 Discussion

The boundary conditions on the electric and magnetic fields for light impinging on an optical interface require that the x-components of the relevant wavevectors must be equal,

$$k_{incident,x} = k_{reflected,x} = k_{transmitted,x}. \tag{4.1}$$

Ignoring for the moment the reflected wave, we may then write the components of the wavevectors in terms of the vacuum wavevector k_0,

$$k_{incident,x} = n_1 k_0 \sin \theta_I = n_2 k_0 \sin \theta_T = k_{transmitted,x}, \tag{4.2}$$

which is easily recognized as a variant of Snell's Law. The important point here is that for a condition of total internal reflection $\sin \theta_T > 1$, so the x-component of the transmitted wavevector is *larger* than the vacuum wavevector. Consulting the dispersion relation, we see that this does not correspond to a radiative field in the second medium; the only way to vectorially add the wavevector components to achieve an allowed (lightlike) total wavevector is for the z-component to be imaginary, which in fact it is. This is the cause of the exponential attenuation of the evanescent wave in the z direction. The condition for a wavevector to be lightlike in a medium of refractive index n_j is

$$k_{j,x} \leq n_j k_0. \tag{4.3}$$

We require an explanation, then, for the observation that we detect light above the sample. The transmitted wavevector, as we have shown, is too large to exist as light. However, it can couple to plasmons in the particles in the array, which then can reradiate the light. Since light is observed, there must be some shrinking of the wavevector that is caused by the array. We may write the momentum conservation condition as

$$k_{shortened,x} = k_{transmitted,x} - g(\text{Lattice}) \tag{4.4}$$

where g is some function dependent on the lattice parameters. Based on dimensional symmetry and a familiar analogy with solid-state physics, we surmise that g is a reciprocal lattice vector of the form

$$g(\text{Lattice}) = m\frac{2\pi}{a}, \tag{4.5}$$

where a is the lattice constant of the array and m is an integer. (We consider the case in which the array is aligned with the x-axis; the generalization to other array orientations in the xy-plane is straightforward.) Noting that the x-components of the transmitted and incident wavevectors are equal, we have

$$\frac{2\pi n_2 \sin \theta_T}{\lambda_0} = \frac{2\pi n_1 \sin \theta_I}{\lambda_0} + \frac{2\pi m}{a}, \tag{4.6}$$

or rearranging,

$$n_2 \sin \theta_T = n_1 \sin \theta_I - \frac{\lambda_0}{a}. \tag{4.7}$$

Here we have chosen $m = -1$ to correspond to a shortening of the wavevector. This equation implies that if we collect light above the sample with a collector having a numerical aperture $NA = \sin\theta_{T,\max} < 1$, there will be certain wavelengths that will not be collected.
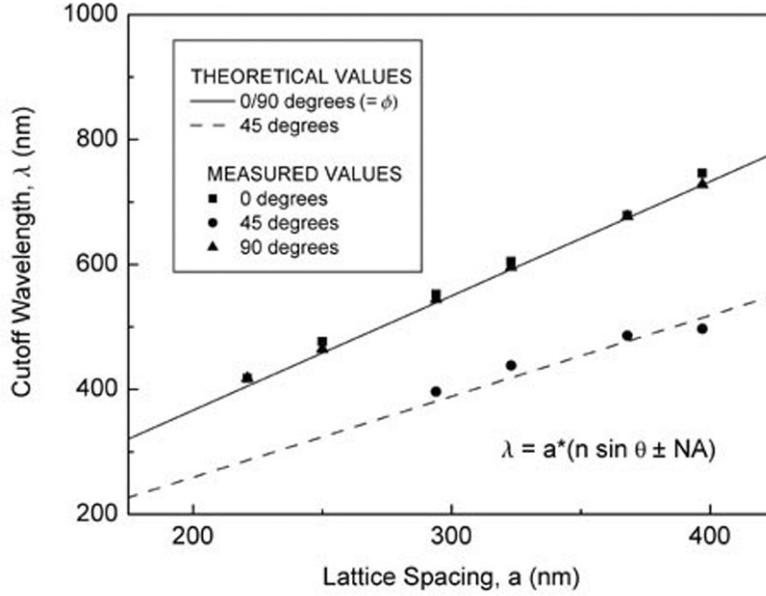
Figure 5.3: Cutoff wavelength vs. lattice spacing for three different angles between the array axis and the plane of incidence for the total internal reflection measurement. The cutoff wavelength in all arrays corresponds to the extremum in the second derivative of the raw spectrum. For square-symmetry arrays, the diffraction conditions at 0° and 90° are identical.

If we can control the parameters of the array, we can control the wavelengths that will pass into the collector. Assuming that $n_2 = 1$ for air, we now have a cutoff wavelength

$$\lambda_{cutoff} = a(n_1 \sin \theta_I \pm NA) \qquad (4.8)$$

where NA is the numerical aperture of the lens. The negative sign before the numerical aperture corresponds to a mirror-like behavior of the array. (Incidentally, this shows that for a lens of a given NA, there are actually *two* cutoff wavelengths. Since our detector is not sensitive to wavelengths much below 400 nm, we only observe the long-wavelength cutoff in our measurements.)

Remarkably, the symmetry in the diffused nanoparticle system is still sufficient for the arrays to exhibit the sharp cutoff. The large width and slight asymmetry of the peaks

is attributed to the size distribution of the individual nanoparticles in the annealed samples. (For reference, Figure 5.2c is the LSPR spectrum of a non-annealed array, measured using a reflection technique. No cutoff is observed in that spectrum because the grating constant is rather short and the incident and reflected wavevectors experience the same refractive index.) Figure 5.3 shows that the cutoff wavelengths measured in the diffused system (from the raw spectra) correspond precisely to the values calculated from diffraction theory.

CHAPTER VI

DIFFRACTED SECOND HARMONIC GENERATION FROM Au NANOPARTICLE
ARRAYS

We show that second-harmonic light can be generated from a diffraction grating of
gold nanoparticles with planar inversion symmetry. By measuring the angular distribu-
tion of second-harmonic light, we observe a novel effect in which the diffraction pattern
of the grating is superimposed on the intrinsic second-harmonic radiation pattern of the
nanoparticles. This result suggests that second-harmonic generation may be used to
study coherent nonlinear optical effects in symmetric as well as asymmetric metal
nanoparticles.[††]

6.1 Introduction

Second-harmonic generation (SHG) has been used for over two decades as an optical
probe of electronic properties of metal nanoparticles (NPs) of varying shape, size, com-
position and spatial organization [3, 16, 17, 71-78]. The objectives of metal NP studies
in general have ranged from measuring electron dephasing [71, 73, 79-83], to pinpointing
the origin of surface-enhanced Raman scattering [17, 84-86] and assessing the potential
for plasmonic applications such as all-optical switching [75, 87-89].

It is usually taken for granted that symmetry forbids the generation of second-
harmonic light in centrosymmetric NP systems [90]. Even when asymmetric NPs are ar-
ranged so that the overall array has inversion symmetry, SHG is completely suppressed

---

[††] The content of this chapter has already been published in *Physical Review B*, 2006 [70] and was included
in the AIP/APS Virtual Journal of Nanoscale Science and Technology (http://www.vjnano.org, **13**, no. 3).

along the illumination direction [81]. This quenching of SHG along the illumination direction holds true for both surface and bulk SHG contributions [72, 81, 82]; for this reason, the potential of SHG for probing electron dynamics in metal NPs has generally been discounted [83]. In this paper, we demonstrate that this difficulty is ameliorated simply by looking at angles other than the illumination direction. This is the first measurement of diffracted SH from NPs with such a high degree of symmetry.

Recently, it has been proposed that arranging asymmetric NPs in a diffraction grating should provide spatial separation of NP-generated SH light from both the incident fundamental beam and the substrate-generated SH light [18], a technique first demonstrated in the 1980s on asymmetric Ag NPs supported on an array of dielectric posts [17]. (From the constructive interference condition $\sin\theta = m\lambda$, odd-integer orders of the second harmonic are equivalent to half-orders of the fundamental, so SH light appears where fundamental light does not. This principle has been used to study SHG from 1D diffraction gratings of polymers [91], adsorbed dye molecules [92] and metals [93].) However, asymmetric NPs are not strictly necessary. We report diffracted SHG from Au nanorods of planar symmetry aligned in a symmetric two-dimensional grating, even when optically excited in a symmetric manner. The resulting SH diffraction pattern is unique in that virtually no zero-order peak exists, and the SHG intensity increases with diffracted order for a single array (and generally with increasing angle of observation from the normal). The SHG depends strongly on resonant enhancement between the particle plasmon resonance and the excitation frequency.

6.2 Experimental Methods

Nanorod arrays were fabricated on indium-tin-oxide(ITO)-coated glass by IBL and thermal evaporation as described in Chapter III. Au was evaporated over the polymer mask to 20 nm mass thickness. Array integrity and NP structure were determined by SEM (Fig. 6.1 inset). Minor defects in the IBL process gave rise to regions of irregular particle coverage, but the arrays had excellent diffractive properties overall. We use nanorods instead of nanodisks (which have higher symmetry) because the different axial lengths in a rod give rise to different resonance energies; hence we may probe SHG on- or off-resonance by rotating the array relative to the incident light. It is also technically easier to control the resonance energy through rod length than through disk diameter.

Fig. 6.1 shows the detection apparatus. The NP arrays, typically 60x60 μm^2, were illuminated by a passively mode-locked Ti:sapphire resonator pumped by 4.5 W of 532 nm light; the oscillator produces 50-fs pulses with center wavelength 800 nm at 93 MHz pulse-repetition frequency with average power ~250 mW. Residual green pump light was blocked with a color filter. Power fluctuations were monitored by a silicon photodi- ode. Pulse duration was measured with an autocorrelator. The fluence was sufficiently low (<0.1 mJ/cm^2) that SHG was achieved without modifying NP morphology. The lin- ear extinction coefficients along the major and minor axes of the nanorods were deter- mined separately with a white-light source and rotatable linear polarizer.
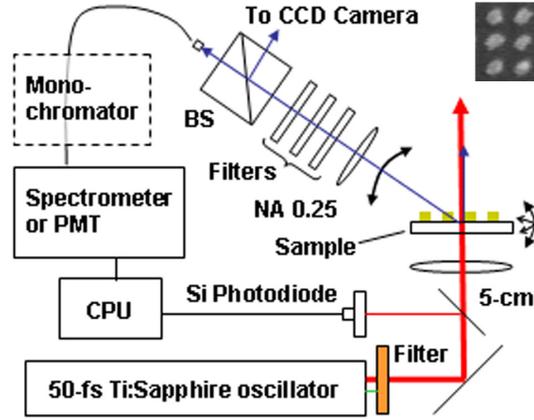
Figure 6.1: Experimental setup for measuring angular distribution of SH light. Inset: SEM image of "tilted" rods with 200 nm spacing.

A 5-cm focal length lens focused the fundamental beam to a ~50 μm diameter spot. We employed the configuration of Zheludev *et al.* [18], in which the laser is normally incident from the rear of the substrate. The arrays were aligned so that the incident polarization pointed along a grating axis. The nanorods pointed either along the grating axis or at a 45° angle to it. The detector arm rotated in the plane defined by the fundamental propagation and polarization directions.

The detector optical train consisted of a microscope objective (NA 0.25), removable filters, a beamsplitter cube for camera viewing, and an optical fiber to direct the light either to a spectrometer with a Peltier-cooled CCD array or a photomultiplier tube (PMT) connected to a photon counting module. For PMT measurements, the SH was filtered by a monochromator set to pass 400 nm, assuring the spectral purity of the signal. At each observation angle the PMT signal was optimized; where multiple measurements were acquired at an angle, the highest recorded value is plotted. In the figures, the relative error is plotted, representing the standard deviation of ten consecutive measurements. Due to difficult alignment the absolute uncertainty could be substantially higher.
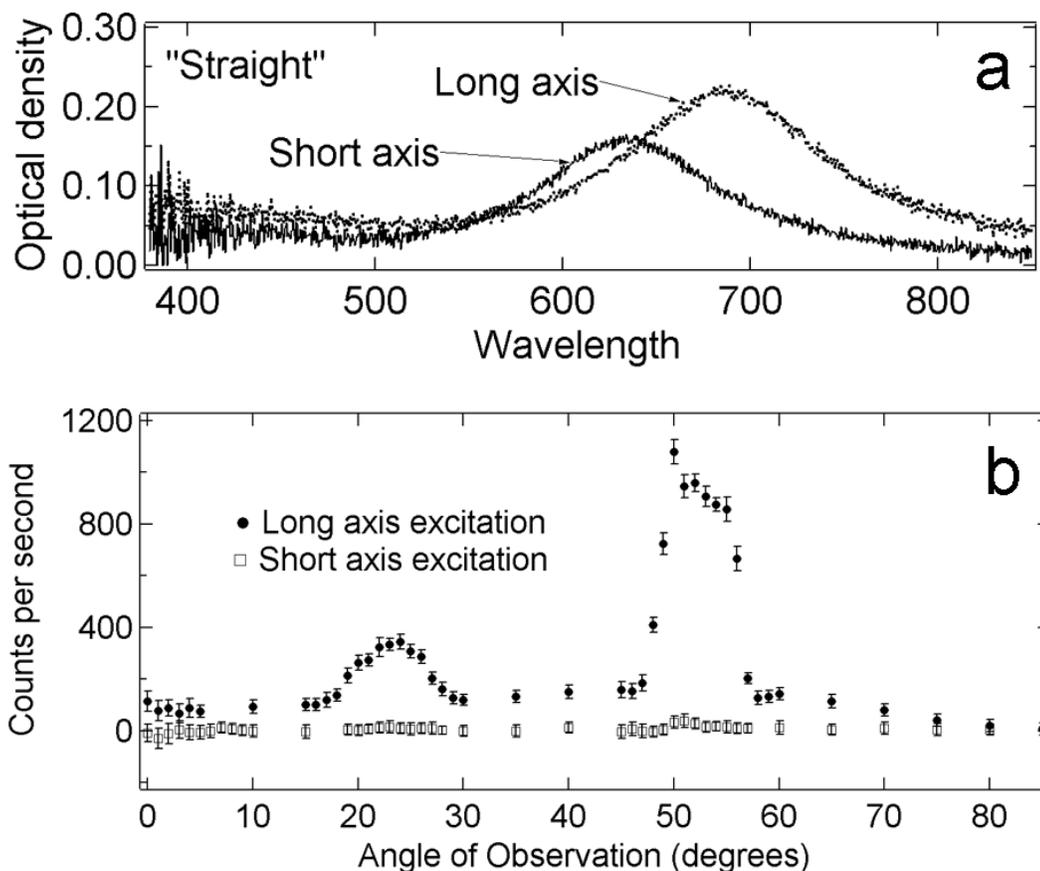
Figure 6.2: (a) Polarization-dependent extinction from "straight" rods. (b) Angular distribution of SHG for the two polarizations. All diffraction patterns are corrected for electrical dark and for the nonlinear response of the bare substrate.

A pervasive difficulty in optical spectroscopy of NP arrays is separating the optical signal from the nanorod array from numerous sources of background light. In this case light must be collected from a 60 x 60 μm^2 area. In the confocal geometry [94] the source (the NP array) is at the focal point of a 10X microscope objective, which refocuses the light to the pinhole of an optical fiber, as in the fiber-optic confocal microscope of Dabbs and Glass [95]. For one-to-one imaging the field of view (FOV) is approximately the same size as the pinhole. We used a 400 μm diameter optical fiber mounted on an adjustable stage as the pinhole, therefore collecting light from a FOV roughly thirty times

81
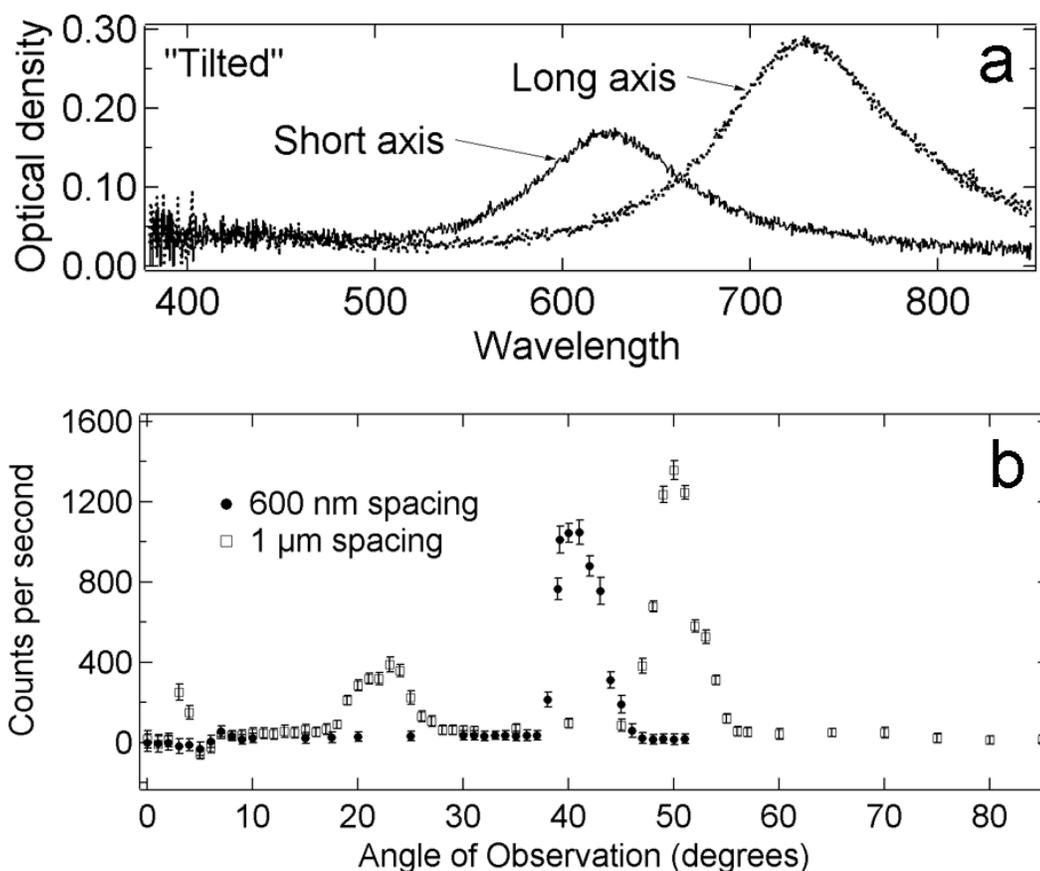
Figure 6.3: (a) Polarization-dependent extinction from "tilted" rods. (b) Angular distribution of SHG with varying lattice spacing. The signal from the 600-nm-spacing array is scaled by 0.36 to match the areal density of the 1-μm-spacing array.

6.3 Results

Figure 6.2 shows the angular distribution of SH light from a 1-μm grating of Au nanorods aligned along the grating axes. The SH output from the long axis is greatly enhanced relative to the short axis because the linear extinction of the long axis is nearly

triple that of the short axis at the excitation wavelength of 800 nm. In the resonant case, the diffracted peak amplitudes are reversed from the conventional situation.

Angular distributions for SH light diffracted by "tilted" rods at NP spacings of 600 nm and 1 μm, respectively, are plotted in Figure 6.3. When normalized to NP areal density, patterns from the two arrays display a general trend of increasing peak intensity with increasing observation angle. These rods are longer than those of Fig. 6.2; thus they exhibit greater extinction (in the long-axis mode) than the "straight" rods at the excitation wavelength of 800 nm. This is why although the particle orientation with respect to the laser is not optimal, the SH output is comparable to the straight-rod case.

At an observation angle of 0°, we observe no SH light except a small and easily identified background that appears in the absence of the arrays. This spurious signal is probably generated at the collection objective by the incident beam, and is generally weaker than the diffracted SH peaks. The first diffracted order of fundamental light is a tiny fraction of the incident beam, so it likely lacks the intensity to produce spurious SH. Thus, even though the second diffracted order of the SH coincides with the first diffracted order of the fundamental, we are confident that we observe only SHG from the NP array at all orders.

6.4 Discussion

The angular distribution in a given measurement is the superposition of the radiation pattern from an individual NP with the diffraction pattern dictated by the array geometry. By adjusting the grating constant, we select the emission angle; in this way we may reproduce the overall angular distribution from the individual nanorods with high sensitiv-

ity due to constructive interference. In all cases we observe no forward-scattered SH light from the NPs, as expected from the symmetry of the array.

Several possible mechanisms may give rise to the observed radiation patterns. In the case of isolated centrosymmetric spheres, such a pattern can be produced either by 1) SH dipole emission generated in a nonlocal process involving both volume and surface susceptibilities of the NPs; or 2) SH quadrupole emission in a local process involving only surface susceptibilities [96]. Either mechanism could be effective in our particles. However, in our particular case the rods are supported on a substrate, so the dielectric environment is asymmetric perpendicular to the substrate with air above and ITO below. This configuration could potentially generate SH even without these more complex mechanisms, since there is a nonzero effective second-order susceptibility (due to the broken symmetry) of the form $\chi^{(2)}_{\perp\|\|}$. The data presented in Fig. 6.3 are insufficient to judge whether there is a quadrupolar component of the SH emission pattern; quadrupolar components could be distinguished at angles θ such that $3\cos^2(\theta) > 1$, *i.e.* at angles beyond 55°.

A simple model of resonant enhancement and SH diffraction gives qualitative agreement with our results. In this model, SH light is generated from an effective dipole SH source that itself varies as the square of the local fundamental field (LFF); thus the SH intensity goes as the fourth power of the LFF, which arises from the response of the ellipsoid to the incident electric field. We caution that this model does not account for multipolar excitations that may indeed be present in particles of the size examined here, and we have further assumed that the induced SH source is purely dipolar and perpendicular to the substrate (*i.e.* out-of-plane) without reference to any nonlinear susceptibilities.

Still, the main features of the experiment – diffraction and resonant enhancement – are reproduced rather well, indicating that the model incorporates most of the essential physics. In addition, although the particles are ~100 nm in the lateral dimensions (which may give rise to quadrupole effects), their height is only 20 nm; thus for the excitation geometry we used, retardation effects should be small since $h/\lambda \sim 1/40$ [97].

The nanorods may be loosely approximated by general ellipsoids. Using a plane wave approximation for the incident light with the foregoing approximations, we may write the induced LFF along an axis of the nanorod (normalized to the incident field) as follows [4]:

$$\frac{E_{1j}}{E_0} = 1 - \left(\frac{L_j}{\varepsilon_1 - 1}\right)\frac{(\varepsilon_1 - \varepsilon_m)^2}{\varepsilon_m + L_j(\varepsilon_1 - \varepsilon_m)}, \qquad (5.17)$$

with indices $j = x, y, z$ corresponding to ellipsoid semiaxes $a \geq b \geq c$ respectively. The shape factors L_j may be written as integrals and computed numerically; for example,

$$L_x = \frac{abc}{2}\int_0^\infty \frac{dq}{(a^2 + q)\sqrt{(a^2 + q)(b^2 + q)(c^2 + q)}}. \qquad (5.18)$$

It is instructive to note that, for wavelengths near resonance, the ratio between the LFFs for the x and y axes reduces to

$$\frac{E_{1x}}{E_{1y}} = \frac{\varepsilon_1 - \varepsilon_m\left(1 - \dfrac{1}{L_y}\right)}{\varepsilon_1 - \varepsilon_m\left(1 - \dfrac{1}{L_x}\right)}. \qquad (5.19)$$

When the numerator and denominator of the RHS are set equal to zero, we obtain the surface plasmon resonance condition for general ellipsoids [4].

Due to the planar fabrication method, the NPs are not strictly ellipsoidal. However, if we assume a fixed particle height 2c = 20 nm, the extinction maxima of Fig. 6.2a can be approximated by an ellipsoid of dimensions 2a = 90 nm, 2b = 78 nm. These parameters were used to calculate the ratio of SH intensities for the major and minor axes, plotted in Fig. 6.4a. Assuming a purely dipolar SH radiation pattern varying with angle as sine-squared, we have modeled Figs. 6.2b and 6.3b using the equations [98]

$$I(\theta) \propto \left(\frac{\sin \beta}{N\beta} \right)^2 \left(\frac{\sin N\alpha}{\sin \alpha} \right)^2 \sin^2 \theta, \quad \alpha \equiv \frac{k\ell_1}{2} \sin \theta, \quad \beta \equiv \frac{k\ell_2}{2} \sin \theta \qquad (5.20)$$

where N is the number of NPs in a row, k is the wavenumber, and ℓ_1 and ℓ_2 are the grating spacing and NP size respectively. The results, plotted in Fig. 6.4, agree reasonably with our experiments. The intrinsic width of the peaks, which is approximately 1°, is not resolved in our experiments due to a relatively large numerical aperture.

The individual particles have considerable substructure common to lithographic NPs, as evidenced by the SEM image. Local field enhancement can be substantial at nano-scale roughness features, giving rise to enhanced nonlinearities, so the roughness defects may be considered SH sources [99]. In addition, deviations from ideal NP shapes have been linked to optical activity particularly in SHG patterns [100]. However, the observed SH diffraction pattern specifies that such defects may not radiate constructively in the forward direction. The data suggest that roughness defects are distributed more or less randomly on the NPs, and our excitation geometry and detection scheme are insensitive to the tensor components discussed in Ref. [100], so we observe no shape bias. There is a small "noise" SH signal at most angles, as seen in Fig. 6.2 (especially for the resonant
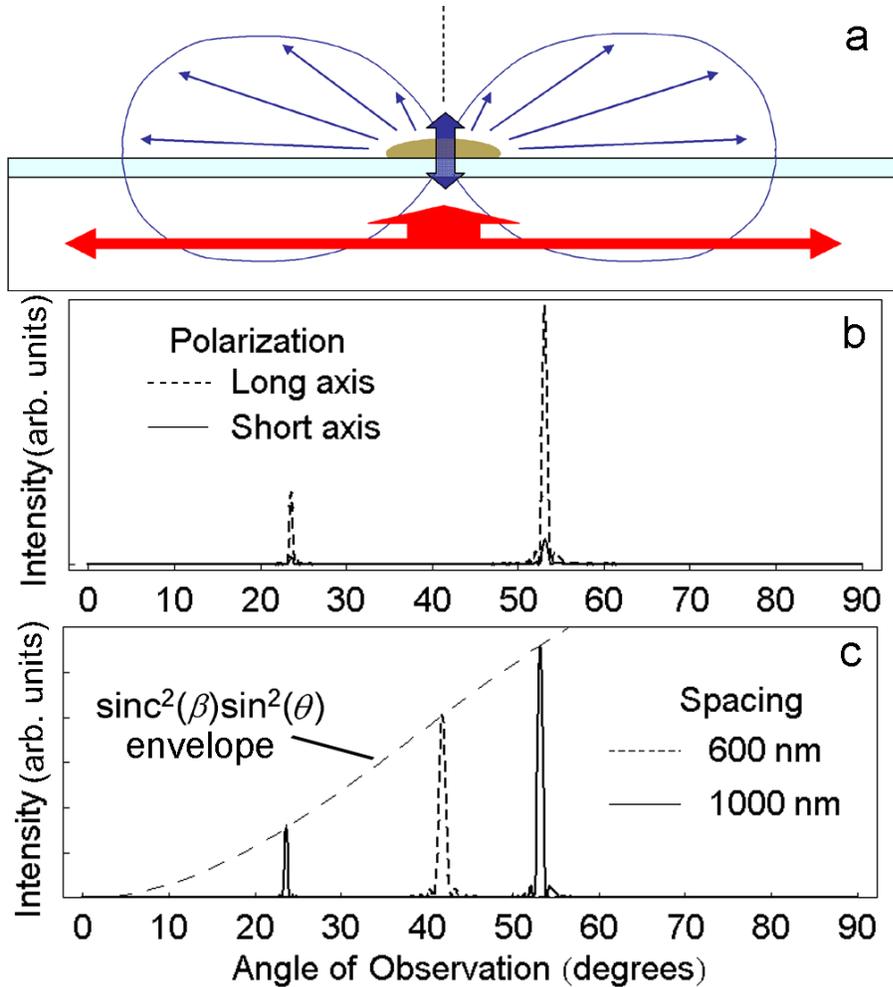
Figure 6.4: (a) Diagram of SH dipole emission pattern. (b) Model calculation of Fig. 6.2b. (c) Model calculation of Fig. 6.3b.

case), which is not attributable to the substrate and is probably due to incomplete cancellation from missing particles rather than the other types of defects.

The SH light from the arrays should retain the temporal coherence properties of the incident light. Our experiment bears a superficial resemblance to hyper-Rayleigh scattering measurements [74, 101], which produce incoherent SH light; however, in the case of arrays the excitation at each particle has a well-defined phase relationship to the others, yielding a coherent output.

The scheme used here differs from that of Ref. [18] in that the NPs we studied have in-plane symmetry. We note that angular measurements on asymmetric particles would retain the out-of-plane SH contribution, while exhibiting an additional in-plane contribution due to individual NP asymmetry. This is not explicitly accounted for in Ref. [18], and could complicate the interpretation of such experiments because the proportion of the out-of-plane contribution would depend on the diffracted angle and hence on the grating spacing. Specifically, the prediction that the ratio of the first-order SH peak to the first-order fundamental peak depends only on the particle structure is called into question.

6.5 Conclusion

This experiment demonstrates that SH may be produced and directed by an appropriately designed grating using symmetric particles, avoiding complications in both lithography and interpretation.

CHAPTER VII

RESONANTLY ENHANCED SECOND HARMONIC GENERATION FROM Au
NANOPARTICLE ARRAYS

SHG from lithographically prepared arrays of symmetric gold nanorods can be increased by two orders of magnitude by choosing nanoparticle size to be resonant with the 800-nm wavelength of the pump laser. The angular variation of the second-harmonic yield, which is defined by the pitch of the nanorod array, can be predicted using standard diffraction theory. This in turn makes it possible to bound approximately the relative contributions of dipole and quadrupole oscillations to the total second-harmonic yield. Resonant ultrafast irradiation also induces morphological changes in the nanorods, a reshaping that apparently results from surface melting and refreezing of the nanorods. At higher fluence, the intensity dependence of the second-harmonic yield changes from quadratic to cubic, an indication that the reshaping influences the mechanism of SHG.[‡‡]

7.1 Introduction

Second-harmonic generation (SHG) is a particularly surface-sensitive optical probe [78]. Metal nanoparticles, with their large optical resonances and high surface-to-volume ratio, would seem to be excellent substrates for measurements that require surface sensitivity. Thus, SHG from metal nanoparticles is of potentially great importance. SHG studies of lithographic arrays of the simplest nanoparticle shapes (disks) have met obstacles because symmetry constraints forbid SHG in the forward and backward directions [96, 101]. To circumvent this problem, some researchers have turned to asymmetric par-

---

[‡‡] The content of this chapter has been submitted for publication to *Applied Physics B*.

89

ticle shapes [81, 102] or to third-order methods [83]. However, we have shown that it is possible to observe SHG from symmetric nanoparticles arranged in a diffraction grating even when illuminated in a symmetric geometry. Because of the symmetry constraints, one must look at nonzero azimuthal angles to observe it. This method avoids the extreme sensitivity of radiated SH light to even small changes in asymmetric particle shape [75, 103], and allows us to excite and detect in the near-visible spectral region. It also accesses different tensor components of the second-order susceptibility than those probed for asymmetric particle shapes like triangles or L-shaped particles. Furthermore, the optical properties of symmetric nanoparticles are much easier to calculate [4], aiding comparison of theory with experiment.

Ordering the NPs in an array is crucial, because the phase-matching condition provided by the grating structure greatly improves the signal-to-noise ratio [18]. In Chapter 6 we used arrays of NPs which were weakly resonant with the excitation wavelength. Here we present results from arrays of NPs whose extinction maxima are well-matched to the laser wavelength, improving the signal by orders of magnitude. By varying the grating constant for a particular NP shape, we can in principle estimate the relative contributions of dipolar and quadrupolar SH radiation modes. However, the high absorption due to resonant enhancement makes thermal effects important. The NPs can be reshaped at temperatures well below the bulk melting point, and calculations show that single laser pulses can heat the NPs to such temperatures. In addition, we find a fluence threshold at which the fundamental intensity dependence of the SH signal switches from 2nd-order to 3rd-order.

7.2 Experimental Methods

Arrays of ellipsoidal Au nanoparticles were fabricated by IBL [49, 70]. The lithographic mask was a 55 nm layer of PMMA, and each addressable pixel in the FIB was exposed for 100 μs. In the arrays described here, Au was evaporated to 15 nm mass thickness, instead of 20 nm as in Chapter VI. This was for two reasons: First, if the lateral dimensions of a general ellipsoid (semiaxes a > b> c) are held constant, reducing the height 2c redshifts the long-axis surface plasmon resonance mode [4], making it easier to tune the SPR to the laser excitation wavelength without unacceptably large increases of the lateral NP dimensions. Second, for a mask thickness of 55 nm, a 15-nm evaporated Au film gives arrays with many fewer missing particles than for a 20-nm film. This thickness dependence of defect density is due to the fact that even for small deposition angles, physical connections may form along the sidewalls of holes in the mask such that many nanoparticles are removed along with the mask during liftoff. We have demonstrated that, for instance, a 4-nm Au layer evaporated over a 55-nm PMMA layer gives defect-free arrays in the sense that there are virtually no missing particles (Fig. 7.1a), whereas a 20-nm evaporated layer for a 55-nm mask can have up to 35% defects depending on the precise deposition angle. For the experiments described here the nominal mass thickness of the NPs was 15 nm. In this case SEM images suggest that ~15% defects is typical (Fig. 7.1b).
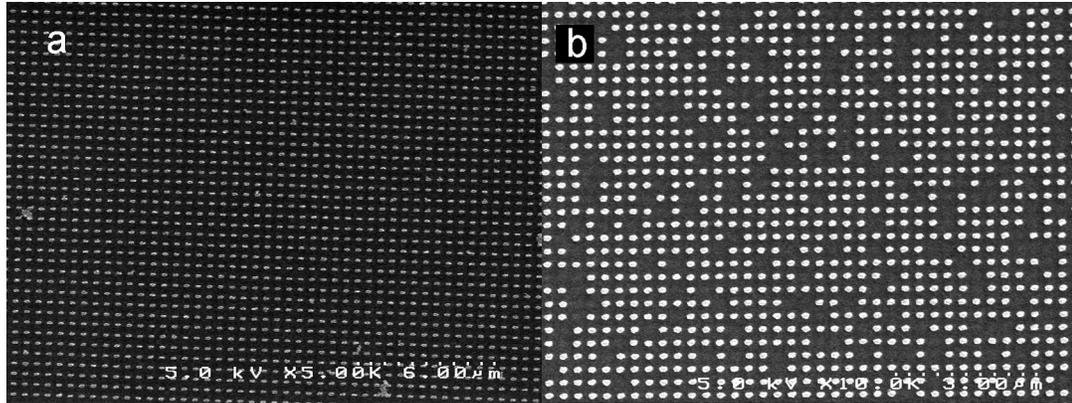
Figure 7.1: a) Subset of an ordered array of lithographically prepared Au nanorods created by evaporating 5 nm Au over 55 nm resist. Perfect particle registration demonstrates the importance of the evaporated layer vs. mask thickness ratio. b) Array of Au nanorods with 15 nm mass thickness. Approximately 15% of particles are missing, which is nonetheless sufficient to maintain strong diffraction grating effect.

We measured angular distributions of SH light using the same custom-built confocal, dark-field optical-fiber microscope described in Chapter VI, with a single modification: a 4X microscope objective was substituted for the 10X objective. We again employed the configuration of Zheludev and Emel'yanov [18] in which the laser is normally incident from the rear of the substrate. Where noted, we induced a slight misalignment of the focusing lens, altering the angle of incidence in order to more easily detect diffracted peaks near the horizon of the sample (80°-90° angle of observation). The arrays were aligned so that the incident polarization pointed along the grating and nanorod axis; in this chapter all nanorods had their long axis along a grating axis. The excitation laser was a passively-mode-locked Ti:sapphire oscillator (Kapteyn-Murnane Laboratories, MTS) pumped by 4.5 W of 532 nm laser light, producing ~50-fs pulses centered at 810 nm. The average output power of the oscillator ranged from 450-500 mW, and fluence was of the order ~0.2 mJ/cm^2.
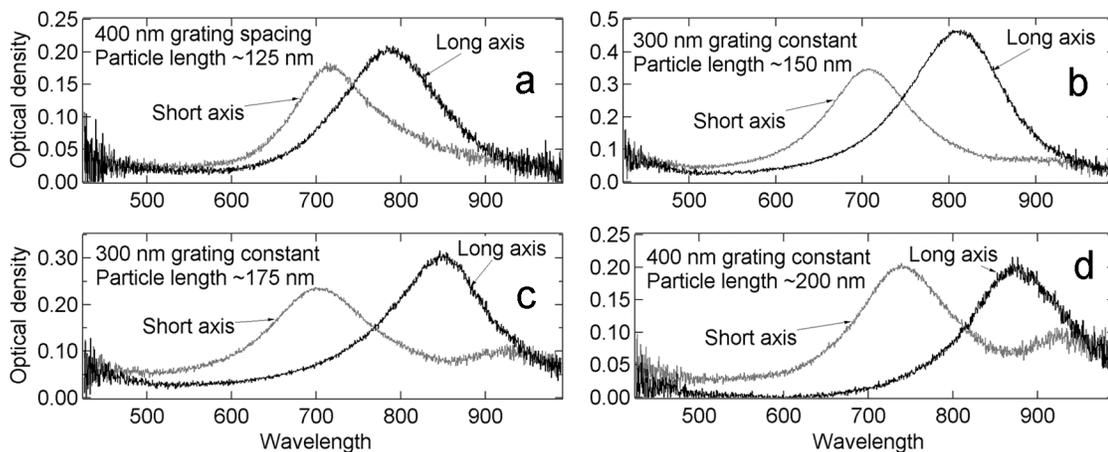
Figure 7.2. Linear extinction spectra of arrays of Au nanorods of varying length: a) ~125 nm; b) ~150 nm; c) ~175 nm; d) ~200 nm. Array from part b) is particularly well-matched to the center wavelength of the excitation laser.

Linear extinction spectra at normal incidence were measured using a Peltier effect-cooled Acton 300i spectrometer in the above configuration, with a 100 W fiber-coupled tungsten lamp (Spectral Products, ASBN-W-L) substituted for the laser and all filters removed from the detector.

7.3 Results and Discussion

7.3.1 Linear Optical Properties of NPs

The extinction maximum for each array was controlled by varying the length of the long axis, with longer NPs giving redder SPR. As seen in Figure 7.2, the extinction maximum of particles with longest dimension ~150 nm occurs at 815 nm, very close to the center wavelength of the laser. This creates the condition for resonantly driving the electrons in the NPs by the Ti:sapphire laser, reminiscent of other antenna-type effects.
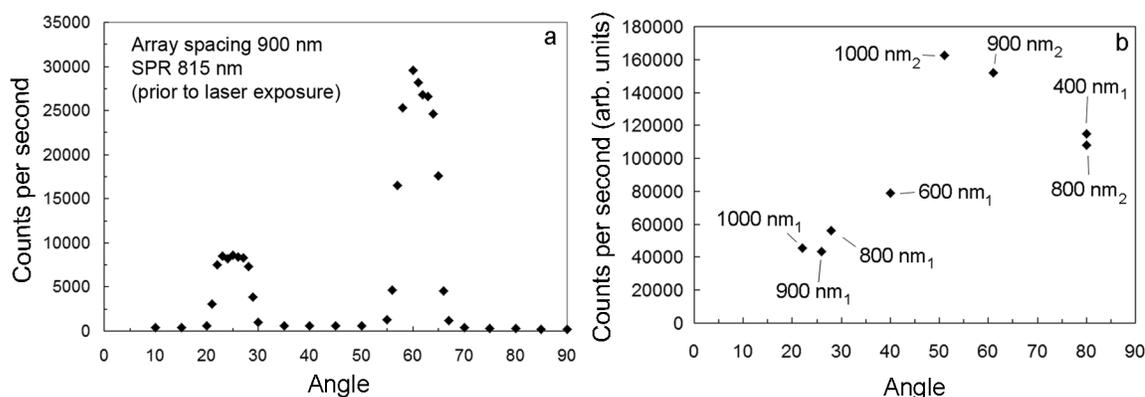
Figure 7.3. a) Angular distribution of SH light from array with 815 nm long-axis SPR (prior to irradiation) and 900 nm grating constant. b) Diffracted peak amplitudes as a function of angle for several arrays with the same NPs (same long-axis SPR). Data points are labeled by grating constant of array; subscript refers to diffracted order. Data are normalized for areal density of arrays using 400-nm-spacing array as a reference.

7.3.2 Angular Distribution of SH Light from Arrays

Fig. 7.3a shows a typical angular SH distribution for an array in which the long-axis SPR of the nanoparticles was at a wavelength of 815 nm. The grating constant of the array is 900 nm. The diffracted peaks occur at the expected angles, and the signal is stronger at the larger angles. In Fig. 7.3b we show the data from arrays with NPs of the same nominal size, but differing grating constants, for calculated laser intensity of order 4-5 GW/cm^2. The data are normalized to the areal density of the different arrays using the 400-nm spacing array as a reference. The two data points shown at 80° are from different arrays and show good agreement. As noted previously, the angle of incidence of the laser was altered slightly to shift the diffracted peaks at the horizon away from the horizon; this did not significantly change the excitation type or mechanism. (For reference, the peaks that occur at 80° in Fig. 7.3b are from an array with 400 or 800 nm separation, so if the laser were perfectly aligned the peaks would occur at 90°. A deviation in the angle of incidence of only a few degrees is required to push the peak to 80°.) Of par-

94

ticular interest is the enormous signal strength observed with the photomultiplier tube and photon counter. For comparison, the maximum signals observed in Ref. [70] were of order 1500 counts/second (cps). Here the maximum signals we present are two orders of magnitude larger, and in some experiments signals as large as 5×10^5 cps were observed. To understand this, we must consider the higher incident intensity, the improved resonant enhancement, and the smaller solid angle subtended by the detector in the present experiment.

7.3.3 Normalization Considerations

A central question regarding the diffraction patterns is whether there is a quadrupole component of the intrinsic radiation pattern of the NPs, and its relation to any dipole component [97]. In certain cases, the quadrupole and dipole contributions can arise from physically different mechanisms. For instance, in isolated metal nanospheres the quadrupole is generated in a local process involving only surface susceptibilities, whereas the dipole is generated in a nonlocal process involving both surface and volume susceptibilities [96, 101]. In these NPs there is an effective second-order susceptibility tensor component of the form $\chi^{(2)}_{\perp \|\|}$ that is nonzero, possibly due to the sole asymmetry in the system, that being the differing dielectrics above (air) and below (ITO) the NP. An alternative mechanism would be a bulk quadrupolar excitation as discussed by Bloembergen *et al.* [104], in which the nonlinear polarization in an isotropic centrosymmetric medium may be written as:

$$\vec{P}^{NL}(2\omega) = (\delta - \beta - 2\gamma)(\vec{E}(\omega) \cdot \vec{\nabla})\vec{E}(\omega) + \beta \vec{E}(\omega)(\vec{\nabla} \cdot \vec{E}(\omega)) + \gamma \vec{\nabla}(\vec{E}(\omega) \cdot \vec{E}(\omega)) \quad (7.1)$$

where the constants δ, β and γ contain materials parameters and frequency. In the case of conducting media the prefactors are as follows:

$$\beta = \frac{e}{8\pi m^* \omega^2}, \quad \gamma = \frac{n_0 e^3}{8 m^{*2} \omega^4}, \quad \delta = \beta + 2\gamma. \tag{7.2}$$

In Eq. 7.2, e is the electronic charge, m^* is the effective electron mass, and n_0 is the electron density of the material. Evidently in the conducting case the first term of Eq. 7.1 vanishes, but Bloembergen cautions that the expression for δ "should not be taken too literally" because of the sensitivity of the term to hydrodynamic forces and surface potential gradients. γ may also be written as $\gamma = \beta(\omega_p^2 / 4\omega^4)$, where ω_p is the classical plasma frequency. (Note that CGS units were used in Ref. [104].)

Consider plane wave excitation of the form $\vec{E}_0(\omega) = E_{0x} \exp(i(\vec{k} \cdot \hat{z} - \omega t))\hat{x}$, where $\hat{z}$ is the surface normal. If the induced field $\vec{E}_1(\omega)$ inside the particle (mediated by the particle plasmon) maintains the functional form of the incident light, the first two terms in Eq. 7.1 vanish and the nonlinear polarization takes the form $\vec{P}(2\omega) \propto E_{1x}^2 \exp(-2i\omega t)\hat{z}$, corresponding to an out-of-plane polarization at the second-harmonic frequency. In this case the nanoscale optical properties would enter through the transition from $\vec{E}_0$ to $\vec{E}_1$.

To first order, each of these possibilities yields a dipolar SH radiation pattern; however, due to the large lateral dimensions of the NPs, there could be quadrupolar components as well. The selection rule that SHG is forbidden in the forward and backward directions holds for the quadrupole as well as the dipole, so it is only at large observation angles that they may be distinguished. From a technological perspective, the ability to manipulate the mechanisms will allow control over the strength and direction(s) of the

SH signal. In order to resolve this, it is essential to properly normalize the SH signal at each diffracted peak. The obvious factors to be normalized are the areal density of particles in the array and any fluctuations in the incident laser intensity. However, the angular spread in a given diffracted peak varies drastically with the grating parameters, and must be accounted for to distinguish dipolar from quadrupolar radiation patterns.

The measured SH angular pattern is the superposition of the multiple-slit diffraction pattern and the SH radiation pattern, which may be written separately as follows [70, 98]:

$$I_{diff}(\theta) \propto \left(\frac{\sin\beta}{\beta}\right)^2 \left(\frac{\sin N_0 \alpha}{N_0 \sin\alpha}\right)^2 \tag{7.3a}$$

$$\alpha \equiv \frac{k\ell_1}{2}\sin\theta, \quad \beta \equiv \frac{k\ell_2}{2}\sin\theta \tag{7.3b,c}$$

$$I_{SH}(\theta) \propto A_{Dipole}\sin^2\theta + 4A_{Quadrupole}\sin^2\theta\cos^2\theta \tag{7.4}$$

Here ℓ_1 is the slit spacing, ℓ_2 is the slit width, and wavenumber $k = 2\pi/\lambda$. Assuming that the SH radiation pattern is given by a linear combination of dipole and quadrupole patterns, A_{Dipole} and $A_{Quadrupole}$ are parameters which can be fitted to the data. The factor of 4 normalizes the maximum of the pure quadrupole pattern to unity, as for the dipole pattern. The multiple-slit diffraction pattern exhibits the following properties. As N_0 increases, the diffracted peak widths decrease due to improved cancellation, stemming from coherent addition of increasing numbers of Fourier components. As the ratio of grating spacing to particle size (which is equivalent, by Babinet's principle, to slit width) increases, the peak widths decrease. As more and more diffracted orders become allowed, the allowed orders are increasingly compressed toward the array normal, compressing the peak widths as well. Finally, as the diffracted angle increases, the angular

peak width increases due to the term containing α. Thus peaks nearest the horizon – precisely where the dipole and quadrupole must be distinguished – exhibit the greatest angular spread.

The measured SH intensity at a given angle is the convolution of the angular SH distribution with the angular width of the detector. An infinitesimally narrow detector would accurately map the intensity, but a real detector with a finite numerical aperture will give erroneously large values for the broader peaks nearer the horizon. With this in mind, we have renormalized the data of Fig. 7.3b as follows. The "extrinsic" diffraction pattern for each array is calculated without any free parameters, using the different experimental values of N_0 and ℓ_1; particle length ℓ_2 is consistent over all arrays in the figure. (We neglect normalization of the perpendicular diffracted peak widths because in that dimension all measured peaks are zero-order, and the peak-width variation is < 3%.) This diffraction pattern is numerically integrated over the specified diffracted peak, with the limits of integration being the angular acceptance of the detector. This is equivalent to performing a convolution with the detector represented by a square function with unit amplitude. The data from Fig. 7.3b are then normalized to the integrated values.

To give a sense of the uncertainty in the measurement, in Fig. 7.4 we have plotted the average between the original dataset of Fig. 7.3b and the renormalized data as described in the previous paragraph. The error bars have been computed by the average difference between the different normalizations, combined with an estimated 10% uncertainty in the original data. We have fitted this dataset, weighted by the error bars, with linear combinations of dipole and quadrupole modes as given by Eq. 7.4.
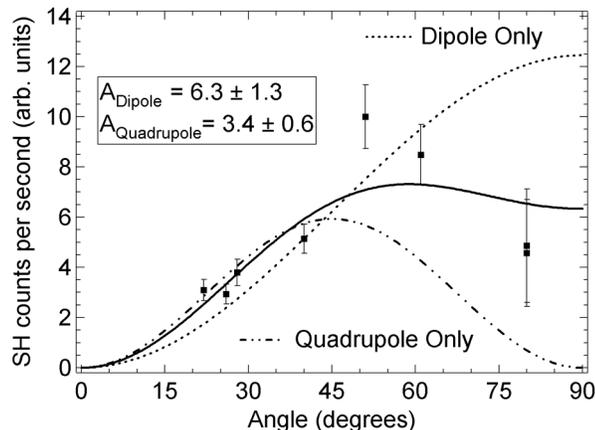
Figure 7.4. Averaged renormalized data of Fig. 7.3b (see text). Solid line is a fit to Eq. 7.3. Dashed lines are fits (using the same weighting as solid line) to pure dipole and quadrupole patterns respectively.

Clearly, the dataset normalized only for areal density exaggerates the dipole contribution relative to the quadrupole contribution. It appears that the contributions from dipolar and quadrupolar modes do not differ by orders of magnitude. Further conclusions based on these data would be premature for three critical reasons. First, the slight alignment offset used to make the diffracted peaks appear at 80° introduces greater uncertainty into those data. Second, the resonant enhancement at the fluence used introduces thermal effects which change the nanoparticle shape. Third, above a certain threshold the fundamental intensity dependence of the SHG changes from 2nd-order to 3rd-order behavior. The latter effects will now be discussed.

7.3.4   Laser-Induced Morphological Changes in NPs

When the SPR mode of the NPs is tuned to the laser wavelength, laser irradiation alters NP shape. Figure 7.5 shows scanning electron micrographs of an array before and after laser exposure. In this case the total exposure time was on the order of one to two
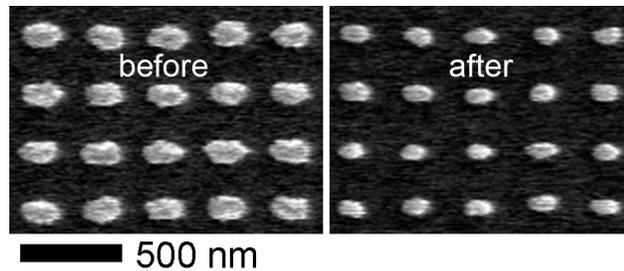
Figure 7.5. Scanning electron micrographs of NPs before and after laser irradiation. Images are of the exact same NPs in the same array. Prior to irradiation SPR was 850 nm.

hours; the average power was ~450 mW, implying peak fluence of ~0.23 mJ/cm^2. The original long-axis SPR of the array was 850 nm; however, after irradiation the lateral dimensions of the particles are reduced to about half of the former area. Extinction measurements following laser irradiation show that the long-axis resonance has considerably blueshifted. At the same time, AFM measurements of laser-irradiated particles demonstrate that the particle heights have approximately doubled relative to the as-deposited mass thickness. Thus, the particles are being reshaped by the laser beam rather than shrinking, as in photodesorption; while we have not ruled out all photodesorption, it is not the dominant effect. Qualitatively, the phenomenon is the "jumping" behavior described by Habenicht and coworkers [105], wherein the particles tend to assume a more spherical shape, increasing the height at the expense of length and width and decreasing the total surface area of the particle in an attempt to minimize the surface energy. However, the fluence used here is orders of magnitude less than the fluence used in their experiment (A. Habenicht, personal communication), which is why we do not observe the range of shapes or the jumping behavior that they found. Our irradiance is much larger than theirs due to the ultrashort pulse duration, confirming that the fluence is the relevant parameter.
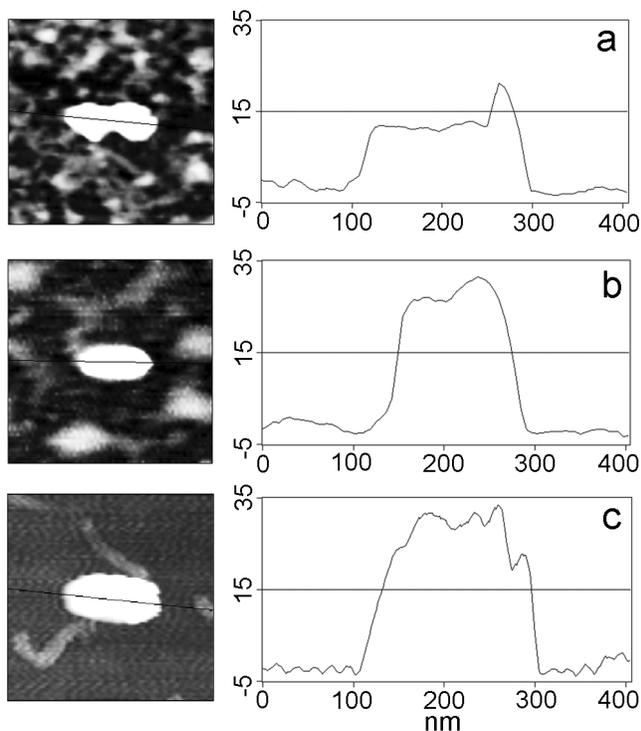
Figure 7.6. AFM images and cross-sections of representative NPs in the same array a) before and b) after annealing for 2 minutes on a hotplate at 180°C. c) AFM of laser-annealed particle from a different sample, which was deposited at the same initial mass thickness as the particle in frame a). Note different scale for x & y axes. All units are nm.

The shape change of Au NPs can take place at temperatures far below the melting point of bulk Au (1064°C); thus this reshaping is likely to be the result of surface melting and diffusion [106]. As a test, we prepared a sample of Au NPs with 15 nm mass thickness of Au. AFM measurements gave particle heights in the range 12-16 nm prior to any treatment (Fig. 7.6a). After the sample is annealed for 2 minutes on a digital hotplate at the relatively low temperature of 180°C, the particles are already significantly reshaped (Fig. 7.6b) in the same way as the laser-irradiated particles (Fig. 7.6c), and SEM indicates that the particles even migrate slightly about the substrate during the anneal. We conclude that the laser need only increase the temperature by a modest amount (temperature

rise on the order of 100 K) for reshaping to occur. At the 2-minute point, the particles appear to have reached equilibrium for that temperature; annealing for an additional 2 minutes does not substantially alter the NP shape.

Here we consider a simple model to find the temperature rise in Au NPs. From Fig. 7.2b we note that the extinction efficiency over the laser spectral range in an array with 300 nm spacing is ~0.45, meaning that roughly half the light incident on a 300 x 300 nm^2 area (one unit cell) interacts with the particle. Assuming 50-fs pulses and a 50-µm spot diameter, the peak fluence of the excitation laser is 2.3 x 10^{-4} J/cm^2. For an Au ellipsoid with major axes 140 x 110 x 16 nm (which for an effective medium $\varepsilon_m = 2$ has resonance maxima very close to that of Fig. 7.2b), the calculated absorption efficiency accounts for about ¾ of the extinction efficiency; the high absorption is similar to that found in an equivalent sphere of radius 31 nm. Thus 45% x 75% = 34% of the incident energy in a 300 x 300 nm^2 area is absorbed by the particle, or ~ 7.0 x 10^{-14} J per pulse. If we consider the NP to have the bulk molar volume (10.21 cm^3/mol) and heat capacity (~25 J/K/mol) values, the temperature rise due to absorption for a single laser pulse is approximately 220 K. Still smaller NPs could have larger temperature rises due to lower volume and increased absorption.

If we consider the effects of pulse repetition frequency as discussed by Gamaly *et al.* [107], we find virtually no cumulative temperature buildup at all. In that model, the increase in average sample temperature is given by $T_{avg} = 2T_{max}\sqrt{t_p / t_{pp}}$, where T_{max} is the temperature rise in a single pulse, t_p is pulse duration and t_{pp} is pulse repetition rate. Because the duty cycle of the laser is small, the cumulative temperature increase over many pulses is of order 1 K. Nonetheless, the temperature rise due to a single pulse can be

quite large, and we reiterate that reshaping of the NP takes place at temperatures far below the bulk melting point. The notion that the NPs are reshaped by each individual pulse, even though there is no cumulative temperature buildup, is supported by the observation that the laser-irradiated sample does not show the degree of particle migration of the annealed sample.
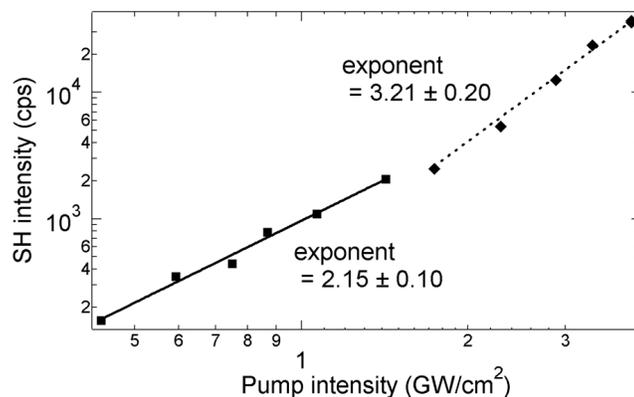
Figure 7.7. Intensity dependence of SH signal, with fits to a power law dependence on fundamental intensity. Note log-log scale.

The intensity dependence of the SH signal is shown in Fig. 7.7. The array used in this measurement had its initial resonance at 770 nm. In these measurements the laser was only unblocked during the 10 s data acquisition for each point. At an approximate fluence threshold of $\sim 7.3 \times 10^{-5}$ mJ/cm^2, the power-law exponent fit changes from 2.15 to 3.21. This may indicate that the thermal effects related to the reshaping process fundamentally change the nonlinear response of the NPs from 2nd- to 3rd-order. The calculated temperature rise at the threshold fluence is ~ 70 K. Working just below this level with arrays whose resonance peak is initially to the red of the excitation laser, we have still detected reshaping through an increase in SHG. The increase is due to the fact that

the reshaping blueshifts the long-axis particle plasmon to be more resonant with the excitation laser. The process takes place on a timescale of a few seconds to minutes.

The error in these measurements is due primarily to the difficulty of aligning the microscope precisely on the diffracted SH peak; we estimate such errors to be on the order of 10% of the measured signal. The thermal reshaping and 3rd-order intensity dependence are likely to affect the results of Fig. 7.3b more than experimental error; *i.e.*, there could be different ratios of dipolar and quadrupolar contributions in the 3rd-order regime than in the 2nd-order regime.

7.4 Conclusions

We have observed SHG from arrays of resonantly excited Au nanoparticles. The unique angular detection capability of our apparatus permits us to compare the relative magnitudes of dipolar and quadrupolar radiation patterns experimentally, once thermal effects such as reshaping have been properly accounted for. The SHG mechanism and the phase-matching condition enforced by the grating set this method apart from hyper-Rayleigh scattering (HRS) measurements [16, 74, 97], which measure an incoherent signal.

The directionality provided by the grating could have applications in nonlinear optical signal generation and routing. An array excited at normal incidence whose grating constant is an integer multiple of the SH wavelength will have a strong diffracted peak running along the surface of the sample. This property could be used to excite fluorescent molecules in the plane of, but some distance away from, the NP array. It could also be exploited in waveguide geometries. The SHG mechanism in concert with the grating

effect could also be a useful probe of fluorescent molecules adsorbed directly on the NPs with specific orientations.

The strong interaction between the light and the NPs makes thermal reshaping effects important. One way to preserve the original dimensions of the NPs might be to cap the NP array with some material as a physical barrier. A capping layer could be useful in other ways: capping the array with ITO, for instance, would remove the asymmetry in the dielectric environment, in which case the HRS mechanisms proposed by Dadap *et al.* [96, 101] would become dominant. Such a method could be used to probe those HRS mechanisms directly and compare the SH strength and radiation pattern with these results. The other important effect of a capping layer is to change the spectral location of the SPR; the particle shape and size would need to be altered in order to maintain the resonant enhancement with the excitation laser. The reshaping is an interesting phenomenon in itself, as it likely relates to the surface tension generated by the small size and large curvature of the NPs [106, 108]; the process dynamics could be studied in an ultrafast pump-probe geometry with a broadband continuum probe pulse.

CHAPTER VIII

REDUCED SECOND HARMONIC GENERATION FROM CLOSELY SPACED PAIRS OF Au NANOPARTICLES

Closely spaced pairs or "dimers" of elongated gold nanoparticles may be expected to exhibit electric field hotspots. We investigate the possible influence of hotspots on second harmonic generation. Preliminary results show that arrays of nanoparticle dimers exhibit reduced second-harmonic generation compared with arrays of single nanoparticles having similar extinction spectra, contradicting a simple model of second-harmonic generation (varying as the fourth power of the local fundamental field).[§§]

8.1 Introduction

The linear optical properties of MNPs have been known for nearly a century and have been widely examined through experiment over the past several decades [2, 3, 33]. The nonlinear optical properties are not nearly as well-characterized, as even the theory of second-harmonic generation from small spheres in homogeneous media was not published until relatively recently [96, 101]. Most studies of SHG from lithographic arrays of NPs have focused on its utility as a tool for autocorrelation measurements of plasmon dephasing, which are unworkable in conventional measurement geometries for particles with in-plane inversion symmetry [81, 83]. The simplest model of SHG in MNPs is that the SH intensity is proportional to the fourth power of the local fundamental electric field (that is, the SH intensity goes as the square of the fundamental intensity). It is well-known that in nanoscale metals, particularly at sharp edges or in small gaps, local "hot

---

[§§] The content of this chapter has been accepted for publication in *Proceedings of the SPIE*.

spots" of greatly increased electric field can occur [86, 109]. These are thought to be related to the unpredictability of surface-enhanced Raman scattering measurements, for example, and control of such hot spots is a major goal of nanoscale photonics. This raises the question of whether hot spots can be exploited to enhance SHG from a spatially controlled metal nanoparticle system.

We have shown that it is possible to measure SH at non-normal observation angles from MNPs with planar symmetry arranged in diffraction gratings; the angular distribution of SH light is the superposition of the radiation pattern of an individual particle with the overall grating pattern [70]. Here, we use this phenomenon to study the effects of particle arrangements on SHG, using "dimer" structures consisting of closely spaced Au nanoparticles that might be expected to exhibit local field enhancements [86]. The extinction characteristics of similar structures have been studied in some detail. Rechberger and coworkers [36] studied pairs of Au disks and found good agreement with a simple dipole-pair model; strong interactions were found for interparticle distances of 50 nm or less. Gunnarsson and coworkers [37] studied isolated pairs of Ag disks and found strong interparticle interactions when the separation was less than ~30 nm. However, no SHG studies of organized dimer structures have been published. SHG from arrays of asymmetric MNPs has been studied, but primarily with attention to dephasing. Another recent study of SHG from MNPs examined Ag nano-pyramids in a hexagonal lattice; no dramatic enhancement effects were observed, and this was attributed to the sample symmetry [110]. Studies of SHG from nano-rough metal surfaces indicated the presence of nanoscale SH hotspots, but relied on random surface features to generate SH [99]. In this study, we report the unexpected finding that dimers exhibit reduced SHG compared with

single particles of approximately identical extinction spectra. We believe that this experiment represents a first step toward testing certain recent predictions of plasmonic effects arising from local hot spots of the electric field, such as the "spaser", which depend on the interactions of femtosecond laser pulses with MNP spatial arrangements achievable at present only by energized-beam lithographies [22].

8.2 Experimental Methods

Gold nanoparticle diffraction gratings measuring ~70 μm were fabricated by IBL as described in Chapter III. For the gratings used here, FIB dwell time per pixel was 100 μs. Au was evaporated to 16 nm mass thickness as measured *in situ* by a quartz crystal microbalance and was verified *ex situ* by spectrophotometry of a co-deposited glass cover slide.

Due to proximity effects, the particles are not physically separated until the nominal gap specified through the software interface exceeds a few pixels. Thus, we fabricated dimers with a range of nominal gap spacings in order to find the separation threshold. The structures are shown in Fig. 8.1(inset); the 5-pixel or "5" spacing is the onset of separation. In this work we label the long axis of the dimer and particles to be the X axis, and the short axis to be the Y axis; grating constants will be denoted (X, Y). We take the +Z-axis to be given by the incident wavevector for convenience in labeling angles.

SH measurements at 400 nm and white-light extinction measurements were performed with the experimental setup described in Chapters VI and VII. In this work a 4X microscope objective was used. The primary feature of the setup is the rotating detection arm, which must be centered on the array of interest to better than 50 μm. The excitation

laser was a Ti:Sapphire (KMLabs) producing 50-fs pulses centered at 805 nm, entering at normal incidence from the rear of the sample. To ensure that we worked in the second-order intensity regime, we used relatively low laser power (~100 mW). For intentional reshaping we used the maximum output power 345 mW, with the focusing lens slightly defocused in order to illuminate the array more homogeneously. AFM indicates that even at 100 mW, some reshaping takes place; we attempted to do the SH measurements with as little laser exposure as possible.

As the physical gap opens up in the dimer, there is a fundamental change in the grating structure along the dimer. The presence of a nearby particle alters the phase of the constructive interference compared with the single-particle case. When the dimer gap approaches one-half the grating constant, the grating spacing is effectively halved. In less extreme cases the opening of the gap primarily reduces the amplitude of the original diffracted peak. To circumvent this complication, we can measure the diffracted SH in the YZ-plane, perpendicular to the dimer long axis. The YZ configuration has the additional advantage that a quadrupole mode will not radiate in the YZ-plane, so the radiation will be dipolar [96]; for single particles, comparison of XZ and YZ results should allow separation of dipolar and quadrupolar effects. Since we cannot easily modify our detector rotation plane, we rotated both the physical sample and the laser polarization using a λ/2 plate to measure in the YZ-plane (Fig 8.2, inset).
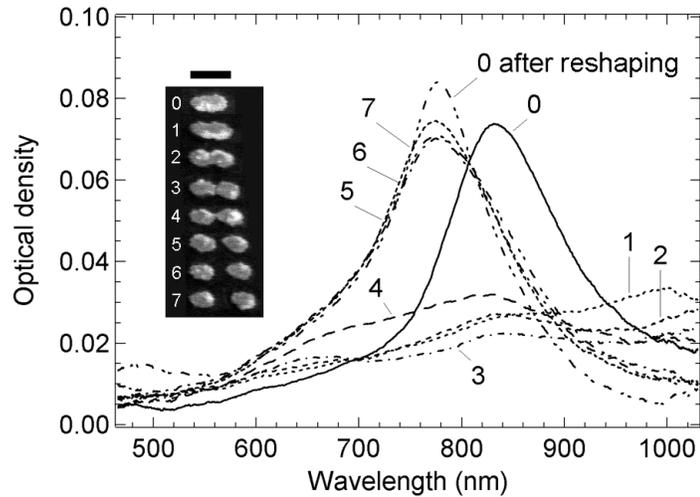
Figure 8.1. Extinction spectra of Au nanoparticle arrays as a function of basis structure. Light is polarized parallel to dimer axis. Inset: SEM images of structure, labeled by nominal gap. Scale bar is 200 nm.

8.3 Results

Extinction spectra are presented in Fig. 8.1 for light polarized along the dimer axis as a function of nominal gap spacing for the set of arrays with spacing (500 nm, 500 nm). Particles with nominal spacing "0" (*i.e.* a single longer particle) have a well-developed resonance, as do the fully-separated dimers "5-7". At a gap of "4", there is a small fraction of physically separated dimers that give slightly increased extinction. Intermediate gap values do not give rise to well-defined resonances; the spectral structure is probably related to a complicated particle morphology caused by proximity effects in the resist. The extinction cross-section values at 800 nm are plotted in Fig. 8.2.

110
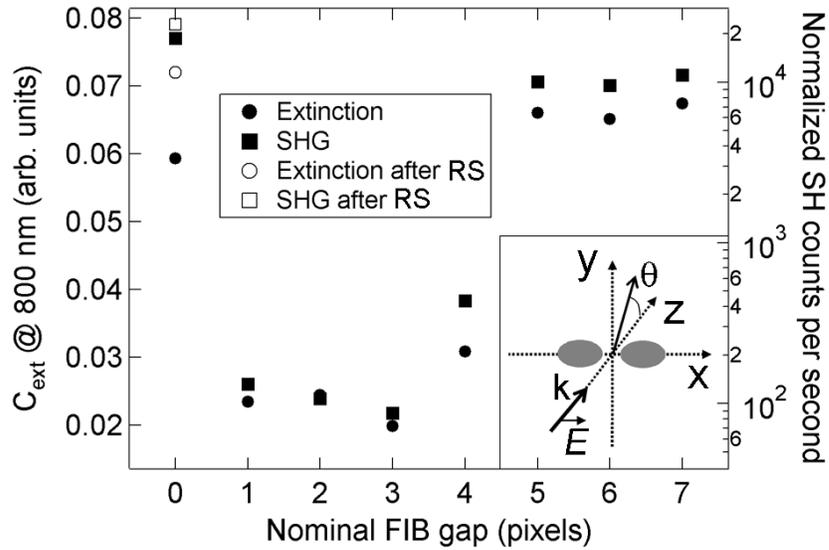
Figure 8.2. Extinction at 800 nm (left axis) and second harmonic intensity (right axis; note log scale) as a function of basis structure. RS = reshaping. Inset: schematic of measurement geometry, where detector angle is varied in YZ-plane.

Diffracted SH intensities are also plotted in Fig. 8.2 (note log scale for right axis). All data points are taken at the same diffracted angle, so we need not normalize for the extrinsic diffraction pattern as we did for the measurement in Chapter VII. In general, the SH output follows the extinction cross-section, regardless of whether there is a well-developed resonance. However, there is an important exception. The "0" array (consisting of single particles with well-developed resonance) gives nearly twice as much SH output as the "5-7" dimer arrays even though the "0" extinction at 800 nm is somewhat less. Since the laser spectrum matched the "0" array extinction better than that of the others, perhaps this could be explained by some effect, thermal or otherwise, that would violate the superposition principle. To explicitly rule this out, we reshaped the "0" array to shift the extinction spectra to better match the dimer arrays. Reshaping was achieved by illuminating with a slightly defocused full-power laser beam for 2 minutes, resulting

111

in an extinction peak that more closely matches the "5-7" dimers (Fig. 8.1). The narrowing and strength increase are partially attributed to increased homogeneity. We measured SH from the reshaped array and found a slight increase in the SH output, as shown in Fig. 8.2 (empty data points). This demonstrates that the extinction at 800 nm is the relevant parameter, rather than the resonance with the laser spectrum at other wavelengths.

8.4 Discussion

The simplest geometric approximation to these particle shapes is the general ellipsoid (semiaxes $a \geq b \geq c$). Calculations of the LSPR modes for general ellipsoids [4] satisfying an arbitrary "flatness" condition $a \geq b > 2c$ show that the out-of-plane LSPR mode is unchanged (within 2 nm) over a large range of a and b values and generally occurs at the shortest wavelength that the dielectric function allows. By contrast, the in-plane spectral positions may vary by hundreds of nm over the same range. Thus we expect that the out-of-plane mode is virtually constant for all particles studied. In addition, the fact that the SH does not seem to change much with increasing dimer gap suggests that near-field coupling of the out-of-plane modes is relatively weak.

In previous work we used a simple model of SHG in which the SH intensity varies as the fourth power of the local fundamental field (LFF) [70]. The LFF is given by the superposition of the incident field with the polarization induced in the NP, so for the SH intensity

$$I_{SH} \propto (1 - L_d \frac{\varepsilon_m}{v} \alpha)^4. \tag{8.1}$$

L_d is a depolarization factor (as in Ref. [4] p. 147), ε_m the dielectric function of the embedding medium, v the NP volume and α its polarizability. (Here we have assumed that

the direction is that of laser polarization.) In this model, the extinction cross-section is related to SHG indirectly through the particle polarizability. For flat ellipsoids similar to our NPs, calculations show that scattering and absorption are comparable at 800 nm $= 2\pi / k$. Since polarizability is directly proportional to volume, volume cancels from the SH expression but not from the extinction cross-section. As the long axis of an NP is reduced, the cross-section for the long-axis mode blueshifts and weakens. The SHG predicted by this model blueshifts as well, but the amplitude is more complicated, reflecting an intricate interplay between the polarizability and the depolarization (which depends on geometry and dielectric behavior). To illustrate this we have calculated extinction cross-sections and SH response from two different ellipsoids using the MLWA (see Section 2.5), designed to have extinction maxima on opposite sides of 800 nm but identical extinction cross-section at 800 nm. In a variety of cases studied, we find that the shorter-wavelength NP *always* gives more SHG than a longer-wavelength NP for equivalent extinction at 800 nm. This is a property of the metallic dielectric function of Au in the 800-nm region [40]; if we input a fictitious dielectric function with similar real values but opposite slope, the behavior is reversed.

This model is contradicted by our results. The dimer particles ("5-7") are smaller and their resonance maxima shorter than 800 nm, yet even in spite of the small interparticle gaps (which are not included in the simple model above) they exhibit considerably *less* SH output than the larger, redder "0" particles. We point out that we do not observe clear evidence (spectral shifts) of strong interparticle interactions in the extinction spectra. This is probably due to inhomogeneities in our sample. Strong spectral shifts rela-

113

tive to isolated disks have been observed in pairs of Ag disks with similar separation; the shifts are highly sensitive to small differences in the gap distance [37].

It is not clear from these results what the effects of local electric field hotspots on SHG would be. Since there is not much variation in the linear spectra with gap separations up to a particle length, the smallest gap sizes here may yet be too large to elicit strong hotspots. This hypothesis can be tested experimentally through more-homogeneous samples, and computationally through more-detailed calculations based on a discrete dipole approximation or a finite-difference-time-domain method. On the other hand, if hotspots do in fact exist in these gaps, then it would appear that hotspots do not enhance SHG, but rather divert energy into other channels, such as non-radiative excitations.

CHAPTER IX

SUMMARY

The goal of this dissertation has been to explore the linear and nonlinear optical properties of lithographically-prepared ordered arrays of metal nanoparticles. In particular we have examined the effects of diffractive behavior caused by the array periodicity.

We showed in Chapter IV through optical and Auger spectroscopy that silver nanoparticles tarnish more readily than bulk Ag in air. This result highlights both the increased chemical reactivity in nanoscale particles and the high sensitivity of the LSPR to small changes in the local dielectric surroundings. It also presents a caution regarding the interpretation of optical spectra from silver nanoparticles exposed to ambient. In Chapter V we demonstrated diffraction from metal nanoparticle arrays in a frustrated-total-internal-reflection measurement, showing that the diffraction is fairly robust even when the particles are largely destroyed.

The diffractive character of ordered arrays may be exploited to study second-harmonic generation from metal nanoparticles, which we explored in Chapters VI-VIII. The non-normal angles of the diffracted peaks allow us to examine particles possessing in-plane symmetry, in contrast to normal-incidence geometries. When the particle plasmon is tuned to match the excitation wavelength, the second-harmonic signal is resonantly enhanced to levels that are particularly striking when the source volume is considered. There is anecdotal evidence suggesting that for high incident fluence the second-harmonic light from MNP arrays may be visible to the unaided eye. These resonant opti-

cal effects are partially obscured by thermal effects, such as surface melting, that occur at high excitation fluence.

Using the diffraction as a heuristic for studying second-order nonlinearities, we have begun to examine the effects of local field enhancements on second-harmonic generation. The first results suggest the possibility that near-field interactions between neighboring particles may suppress SHG relative to single nanoparticles. Further tests are necessary to confirm or confute this idea.

There are many possibilities for future study with diffracted harmonic light. I now present a brief list of experiments which seem to be natural extensions of the work presented in this dissertation.

- The question of dipole vs. quadrupole SH radiation modes, raised in Chapters VI and VII, has not been definitively answered. Careful measurements with arrays whose grating constant is finely controlled are needed to probe the near-horizon diffracted angles. The rather minor technical difficulty is that near the horizon, the angle depends most strongly on the grating spacing, so fine control of grating spacing is needed to specify the angle.

- For arrays whose grating constant exactly matches the second-harmonic wavelength, the SH light should be radiated directly across the sample plane. The propagation of SH light across the sample could be probed with fluorescent markers to find propagation lengths. SH light could also conceivably be produced in a waveguide geometry for similar effect.

- An important question regarding resonantly enhanced SH light is the strength of the resonant enhancement and the character of the excitation in the absence of any ther-

mal reshaping. Since second-harmonic intensity should depend on the incident intensity, not fluence, it will be beneficial to reduce the pulse duration of the laser as much as possible. If a 12-fs pulse can be achieved (most recently the shortest pulse achieved is ~20 fs; the bandwidth of the laser is sufficient to produce 12-fs pulses), the second-harmonic intensity could be increased by a factor of ~16, allowing a dramatic decrease in fluence which should reduce and eventually eliminate thermal effects.

- It would be of particular interest to measure the pulse duration of the diffracted second-harmonic light. The grating provides transverse phase-matching, but the coherence properties of the second-harmonic light are yet unknown.

- There are well-known polarization selection rules for SHG (see Refs. [21, 75, 97, 100]) analogous to the dipole/quadrupole selection rules mentioned in the dissertation. These could be studied in the present experimental apparatus by inserting rotating polarizers at appropriate places in the optical path.

- The computations presented in Chapter II can be enhanced by the introduction of more precise numerical methods for arbitrary particle shapes. The Discrete Dipole Approximation is similar in spirit to the CDA and exists for such a purpose. In addition, it may be feasible to model the effects of a substrate near a metal nanoparticle rather than using an effective-medium approach [7]. If the second-order nonlinearities can be connected to the LSPR in a straightforward manner, it may be interesting to study a kind of nonlinear coupled-dipole model including the second-order behavior. Already, quadrupolar components can be inserted into the CDA without

too much pain [33]; so if the SH turns out to be primarily quadrupolar this should not present insurmountable difficulty.

In summary, this work has unlocked a door to a potential wealth of information about the nonlinear (second-order, in particular) optical properties of metal nanoparticles. This information is made available by exploiting the phase-matching provided by the grating, which results from the ordered arrangement of the nanoparticles.

APPENDIX

COMPUTER PROGRAMS

For the interested programmer, I have appended several sample MATLAB files used in the CDA computations. For convenience, to avoid lengthening the List of Figures unnecessarily I have labeled each file as a separate Figure, but these Figures can extend over several pages.

Figure A.1 is a CDA program for oblate ellipsoids. Figure A.2 is the driver file to call the program of Fig. A.1. Figure A.3 is a CDA program for spheres, including the quasistatic, MLWA and Mie-dipole versions of the sphere polarizability, from which I have stripped the majority of the array-creation and file-handling code.

Figure A.4 is the integrand function, which is called by the CDA programs to calculate the detector response, and itself calls two custom functions. Figure A.5 is the function "mcross4.m", which is a custom generalized version of the built-in MATLAB matrix cross-product function "mcross.m". Figure A.6 is a similar custom cross-product function which I have named "arraycross.m". Each of these functions takes two matrices of 3-vectors as inputs. MCross4 computes the cross-products of each 3-vector in matrix A with each 3-vector in matrix B. ArrayCross requires that A and B have the same dimension, and only computes the cross-products of 3-vectors having the same column index in A and B; the result of ArrayCross is a matrix with the same dimensions as A and B. Computation efficiency can be improved by writing custom function files like these for each combination of the desired dimensions of the input vectors or matrices.

```matlab
 1 function [null] = CDAprogramE(dim,type,N,a,h,space,subspace,Polar,...
 2     Azimuthal,E0,detector)
 3 % CDAPROGRAME(dim,type,N,a,space,subspace,E0,detector) Functionalized
 4 % version of the CDA calculation FOR OBLATE ELLIPSOIDS which may be called
 5 % repeatedly by a driver m-file. Required inputs are dim, type, N, a, h,
 6 % space, subspace, Polar, Azimuthal, E0, detector. Program does not return
 7 % anything; should simply execute.
 8
 9 % Computing the power (integrated intensity) of radiation over a 15-degree
10 % cone from the array of self-consistent dipole moments; full-scale program
11 % with data handling and directory creation. Version 2.8.2,
12 % 6/July/2006, Matthew McMahon, Vanderbilt University.
13
14 disp(sprintf('CDAEv2.8.2 called for dim = %d, type = %s, N = %d, a = %d,'...
15     'h = %d, space = %d,',dim,type,N,a,h,space));
16 disp(sprintf('\tsubspace = %d, Polar(deg) = %g, Azimuthal(deg) = %d,'...
17     'E0 = %s.',subspace,Polar*180/pi,Azimuthal*180/pi,E0));
18
19 %******CONSTANT DEFINITIONS USED IN PROGRAM
20 % Speed of light in vacuum [nm/fs]
21     c = 299.792458;
22 % imaginary unit, just so I don't confuse with dummy index i
23     I = complex(0,1);
24 % Permittivity of free space [fC/Volt/nm]
25     eps_0 = 8.854187817e-6;
26 % Impedance of free space [fs/V/fC]
27     Z0 = 376.7303135;
28
29 %******SELECT DIELECTRIC FUNCTION
30 % Get INTERPOLATED SMOOTHED PALIK/NW silver dielectric function, 300-600 nm
31 %   load newNWeps.dat; silver_eps = newNWeps; clear newNWeps;
32 % Get INTERPOLATED JOHNSON & CHRISTY silver dielectric function, 300-600 nm
33   load newJCeps.dat; silver_eps = newJCeps; clear newJCeps;
34
35 %******SELECT INCIDENT LIGHT INITIAL CONDITIONS
36 % WAVEVECTOR
37 % Calculates direction of wavevector in Cartesian coords. given the Polar
38 % and Azimuthal angles (in radians) as inputs.
39     wavevector = [sin(Polar)*cos(Azimuthal),sin(Polar)*sin(Azimuthal),...
40         cos(Polar)];
41 % POLARIZATION
42     ph2 = E0; % placeholder for info tags
43 % Incident light p-polarized (PARALLEL to plane-of-incidence);units [V/nm];
44     E0p = [sin(Polar-pi/2)*cos(Azimuthal),...
45             sin(Polar-pi/2)*sin(Azimuthal),cos(Polar-pi/2)];
46 % Incident light s-polarized (NORMAL to plane-of-incidence); units [V/nm];
47     E0s = [cos(Azimuthal+pi/2),sin(Azimuthal+pi/2),0];
48 % Normalized incoherent superposition of s- and p- polarizations; [V/nm];
49     E0i = (E0p+E0s)/sqrt(2);
50
51 if E0=='p' E0 = E0p;
52 elseif E0=='s' E0 = E0s;
53 elseif E0=='i' E0 = E0i; end;
54
55 %******PARTICLE ARRAY CALCULATION
```

Figure A.1.1. CDA program for oblate ellipsoids, page 1 of 5.

```matlab
56 % Returns particle positions in (x,y,z) coordinates such that the array is
57 % centered at the origin. All particle position units are [nm].
58
59 Total = 0; % counter variable
60 r=[];
61 if dim==1 % Lattice is a linear chain (Can be a chain of dimers or trimers)
62     if strcmp(type,'single')==1
63         ph1='S'; % placeholder for 'type' info tags
64         for i = 1:N
65           Total = Total + 1;
66           r = [r [(i-(N+1)/2)*space,0,0].'] ;
67         end;
68     elseif strcmp(type,'dimer')==1  % specify basis type to be dimer
69         ph1='D';
70         for i = 1:N
71             Total = Total + 2;
72             r = [r [(i-(N+1)/2)*space - subspace/2, 0, 0].'] ;
73             r = [r [(i-(N+1)/2)*space + subspace/2, 0, 0].'] ;
74         end;
75     elseif strcmp(type,'trimer')==1 % specify basis type to be trimer
76         ph1='T';
77         height = subspace*tan(pi/3)/2; % height of equilateral triangle
78         for i = 1:N
79             Total = Total + 3;
80             r = [r [(i-(N+1)/2)*space, height/2, 0].'] ;
81             r = [r [(i-(N+1)/2)*space - subspace/2, -height/2, 0].'] ;
82             r = [r [(i-(N+1)/2)*space + subspace/2, -height/2, 0].'] ;
83         end;
84         r = sortrows(r',[1 2])';
85     end;
86 elseif dim==2 % Lattice is a 2D square array
87     if strcmp(type,'single')==1
88         ph1='S';
89         for i = 1:N
90             for j = 1:N
91                 Total = Total + 1;
92                 r = [r [(i-(N+1)/2)*space , (j-(N+1)/2)*space ,0].'] ;
93             end;
94         end;
95     elseif strcmp(type,'dimer')==1  % specify basis type to be dimer
96         ph1='D';
97         for i = 1:N
98             for j = 1:N
99                 Total = Total + 2;
100                 r = [r [(i-(N+1)/2)*space - subspace/2,...
101                     (j-(N+1)/2)*space, 0].'] ;
102                 r = [r [(i-(N+1)/2)*space + subspace/2,...
103                     (j-(N+1)/2)*space, 0].'] ;
104             end;
105         end;
106         r = sortrows(r',[1 2])';
107     elseif strcmp(type,'trimer')==1 % specify basis type to be trimer
108         ph1='T';
109         height = subspace*tan(pi/3)/2; % height of equilateral triangle
110         for i = 1:N
```

Figure A.1.2. CDA program for oblate ellipsoids, page 2 of 5.

```
111                 for j = 1:N
112                     Total = Total + 3;
113                     r = [r [(i-(N+1)/2)*space,...
114                         (j-(N+1)/2)*space + height/2, 0].'] ;
115                     r = [r [(i-(N+1)/2)*space - subspace/2,...
116                         (j-(N+1)/2)*space - height/2, 0].'] ;
117                     r = [r [(i-(N+1)/2)*space + subspace/2,...
118                         (j-(N+1)/2)*space - height/2, 0].'] ;
119                 end;
120             end;
121         r = sortrows(r',[1 2])';
122     end;
123 else disp('Error in dimension or type variables');
124 end;
125
126 %******OBLATE ELLIPSOID PARAMETERS CALCULATION
127 % Calculate eccentricity, shape factor
128 ee = 1-h*h/a/a ; % from Bohren/Huffman p.146 Eqn.(5.34)
129 ge = sqrt((1-ee)/ee) ; % e is eccentricity, ee is e^2
130 Ll = ge/2/ee*(pi/2 - atan(ge)) - ge*ge/2 ; % shape factor
131 if h==a % this caveat avoids spurious NaNs/infinities for spherical limit
132     Ll=1/3;
133 end;
134
135 %******SELF-CONSISTENT DIPOLES and INTEGRATED INTENSITY
136 % File headers and array preallocation
137 % Create header information string to tag data columns
138     header = sprintf('%d%s%s_%02d_%02da%02dh%03d_%03d', dim, ph1, ph2,...
139         N, a, h, space, subspace);
140 lambdavals = size(silver_eps,1);
141 lambdacol = silver_eps(:,1);
142 Alpha = [lambdacol zeros(lambdavals,1)];
143 Cext = [lambdacol zeros(lambdavals,1)];
144 Qext = [lambdacol zeros(lambdavals,1)];
145 Power = [lambdacol zeros(lambdavals,1)];
146 tic
147 for num = 1:lambdavals % iterates over different values of wavelength
148     %******SELF-CONSISTENT DIPOLE ARRAY CALCULATION
149     % Returns a 3*Total x 1 vector (3 dipole moment components at each
150     % particle location for Total particles) for each wavelength of
151     % interest.
152
153     % Get wavelength [nm]
154         lambda = silver_eps(num,1);
155     % Get complex dielectric function [unitless]
156         epsilon = complex(silver_eps(num,2),silver_eps(num,3));
157     % Calculate wavenumber [nm^-1]
158         K0 = 2*pi/lambda;
159     % Incident wavevector
160         K = K0*wavevector;
161     % Oblate spheroid polarizability function in the quasistatic limit,
162     % WITHOUT MLWA
163         %polarizability from Bohren/Huffman, SI volume factor
164 %         Alpha_i = 4*pi*h*a*a*(epsilon-1)/(1+Ll*(epsilon-1)) ;
165 %         Alpha(num,2) = Alpha_i;
```

Figure A.1.3. CDA program for oblate ellipsoids, page 3 of 5

```
166      % WITH MLWA
167          % Soller & Hall expression (2002 JOSAB):
168          F = 1 - K0^2*a^2 - 2*I*K0^3*a^3/3;
169          %polarizability from Bohren/Huffman, SI volume factor
170          Alpha_i = 4*pi*h*a*a*(epsilon-1)/(1+L1*(epsilon-1)*F) ;
171          Alpha(num,2) = Alpha_i;
172
173      % Calculate the incident electric field at each particle location
174      % (NOT retarded field)
175      % 1 V/nm incident field in either polarization, modulated only by phase
176          Ein = [];
177              for i = 1:Total
178              Ein = [Ein E0*exp(I*dot(K,r(:,i)))] ;
179              end;
180          Ein = Ein.' ;              % unconjugated complex transpose
181
182      % Calculate the 3Total x 3Total interparticle interaction matrix that
183      % accounts for the retarded fields at each dipole location
184      Aij = [];
185          for i = 1:Total
186              for j = 1:Total
187                  % Self-interaction terms; 1/alpha terms along matrix
188                  % diagonal, 3 at a time
189                  if j==i
190                      Aij(3*i-2:3*i,3*j-2:3*j) = 1./Alpha_i./eps_0 * eye(3);
191                      continue;
192                  end;
193                  % rij vector for retarded field at ri from particle at rj
194                  rijv = r(:,j) - r(:,i);
195                  r_mat = rijv*rijv';        % 3x3 matrix rijrij
196                  rij = sqrt(dot(rijv,rijv)); % magnitude of rij vector
197                  % Interparticle interaction matrix
198                  Aij(3*i-2:3*i,3*j-2:3*j)=exp(I*K0*rij)/4/pi/eps_0/rij^3*...
199                      (K0*K0*r_mat - K0*K0*rij*rij*eye(3) + ...
200                      (1-I*K0*rij)*eye(3) - 3*(1-I*K0*rij)*r_mat/rij/rij) ;
201              end;
202          end;  % end of calculating matrix Aij
203
204      % Calculate dipole moments P [fC*nm] using MATLAB's left matrix divide
205      % operator
206          P = Aij\Ein;
207      % Calculate extinction cross sections and efficiencies
208          % cross section, SI version [nm^2]
209          Cext(num,2) = K0./eps_0.*imag(dot(Ein, P))./dot(Ein, Ein);
210          % extinction efficiency [unitless]
211          Qext(num,2) = Cext(num,2)/pi/a^2;
212      % Convert P from a 1 x 3N^2 vector to a 3 x N^2 matrix
213          P = reshape(P,3,[]);
214
215      %******INTEGRATED INTENSITY CALCULATION
216      % Integrate the power per steradian to get the total power inside a
217      % cone of opening angle specified by "detector". Natural units for the
218      % integration are spherical (r, theta, phi). Units of power_k are [W].
219      % File "integrand2.m" must be in the same directory as this program.
220          detector = pi/12;
```

Figure A.1.4. CDA program for oblate ellipsoids, page 4 of 5

123

```
221          integral = dblquad(@integrand2, 0, detector, 0, 2*pi,[],[],I,K0,...
222             Total,r,P);
223          power_k = c.^2.*Z0.*K0^4./32./pi^2 .* integral;
224          Power(num,2) = power_k;
225 end;
226 toc
227
228 %******SAVING VARIOUS DATA TO FILES
229 % Syntax: "%02d" (also "%+02d") means convert from decimal form to string,
230 % padding with zeroes on the left to 2 decimal places. Each successive
231 % instance of %..d refers to the successive variables passed after the
232 % string. Use %s instead of %d to pass a string variable. For fprintf
233 % calls, it is CRITICAL to make sure unconjugated transpose .' is always
234 % used.
235
236 % Create information string to append to filenames
237     infostring = sprintf('_%d%s%s_%02dx%02da%02dh%03dnm%03d', dim, ph1,...
238        ph2, N, a, h, space, subspace);
239 % Create data directory in which to save files
240     datadir = sprintf('DATA%s', infostring);
241     mkdir(datadir);
242 % Particle positions, named using RAW convention (ASCII)
243     tempname = sprintf('xvals%s.dat', infostring);
244     save(tempname, 'r', '-ascii');
245     movefile(tempname, [datadir '/' tempname]); clear tempname;
246 % Polarizabilities (dat-file) WITH HEADERS, tab-delimited
247 % For convenience I save the imaginary part of Alpha in a 3rd column.
248     tempname = sprintf('alphas%s.dat', infostring);
249     fid = fopen(tempname, 'wt');
250     fprintf(fid, sprintf('wavelength\tReA%s\tImA%s\n', header, header));
251     fprintf(fid, '%3g\t%g\t%g\n', [Alpha(:,1).'; real(Alpha(:,2)).';...
252        imag(Alpha(:,2)).']);
253     fclose(fid);
254     movefile(tempname, [datadir '/' tempname]); clear tempname;
255 % Extinction efficiencies (ASCII) WITH HEADERS, tab-delimited
256     tempname = sprintf('qext%s.dat', infostring);
257     fid = fopen(tempname, 'wt');
258     fprintf(fid, sprintf('wavelength\tQ%s\n', header));
259     fprintf(fid, '%3g\t%g\n', Qext.');
260     fclose(fid);
261     movefile(tempname, [datadir '/' tempname]); clear tempname;
262 % Extinction efficiencies (IGOR TEXT FILE) WITH HEADERS, tab-delimited
263     tempname = sprintf('qext%s.itx', infostring);
264     fid = fopen(tempname, 'wt');
265     fprintf(fid, sprintf('IGOR\rWAVES\twavelength\tQ%s\rBEGIN\r', header));
266     fprintf(fid, '%3g\t%g\r', Qext.');
267     fprintf(fid, 'END\r');
268     fclose(fid);
269     movefile(tempname, [datadir '/' tempname]); clear tempname;
270 % Copy program file to data directory
271     tempname = sprintf('PROGRAM%s.m', infostring);
272     copyfile([mfilename '.m'], [datadir '/' tempname]); clear tempname;
273
274 disp(sprintf('Subroutine complete'));disp(datestr(now))
```

Figure A.1.5. CDA program for oblate ellipsoids, page 5 of 5

```
 1 % Driver program to call the CDAprogramE function, in order to iterate
 2 % through many calculations at one time.  This driver would compute arrays
 3 % of oblate ellipsoids ranging from a single particle (1x1 array) to a
 4 % 10x10 array.
 5
 6 % Note: To iterate over different strings for string variables, use cell
 7 % arrays {} in the iterator and convert to strings in the body of the loop
 8 % by using the 'char' command, i.e.
 9 % for cell = {'s','p','d','f'}
10 %    string = char(cell);
11 % end;
12
13 clc;
14 clear all;
15 diary todaysDate_log.txt
16 disp(datestr(now));
17
18 % Initialize variables
19 dim = 2;
20 type = 'single';
21 a = 50;    % semimajor axis
22 h = 5;     % semiminor axis (half-height h)
23 space = 200;    % interparticle spacing
24 subspace = 1;   % not used for single-particle basis
25 Polar = 0;      % normal incidence
26 Azimuthal = 0;
27 E0 = 'i';
28 detector = pi/12;   % 15 degree opening angle
29
30 for N = 1:10
31     CDAprogramE(dim, type, N, a, h, space, subspace,...
32     Polar, Azimuthal, E0, detector);
33 end;
34
35 disp('The run has been completed.');disp(datestr(now))
36
37 diary off
```

Figure A.2. Driver program to call the function "CDAprogramE,m" defined in Fig. A.1.

```matlab
 1 function [null] = CDAprogram(dim,type,N,a,space,subspace,Polar,...
 2     Azimuthal,E0,detector)
 3 % CDAPROGRAM(dim,type,N,a,space,subspace,E0,detector) Functionalized
 4 % version of the CDA calculation which may be called repeatedly by a driver
 5 % m-file. Required inputs are dim, type, N, a, space, subspace, Polar,
 6 % Azimuthal, E0, detector. Program does not return anything; should simply
 7 % execute.
 8
 9 % Computing the power (integrated intensity) of radiation over a x-degree
10 % cone from the array of self-consistent dipole moments. Version 2.7.2,
11 % 27/June/2006, Matthew McMahon, Vanderbilt University.
12
13 disp(sprintf('CDAv2.7.1 called for eps_m=1,dim = %d, type = %s, N = %d,'...
14     'a = %d, space = %d,',dim,type,N,a,space));
15 disp(sprintf('\tsubspace = %d, Polar(deg) = %g, Azimuthal(deg) = %d,'...
16     'E0 = %s.,detector = %g',subspace,Polar*180/pi,Azimuthal*180/pi,...
17     E0,detector*180/pi));
18
19 %******CONSTANT DEFINITIONS USED IN PROGRAM
20 % Speed of light in vacuum [nm/fs]
21     c = 299.792458;
22 % imaginary unit, just so I don't confuse with dummy index i
23     I = complex(0,1);
24 % Permittivity of free space [fC/Volt/nm]
25     eps_0 = 8.854187817e-6;
26 % Impedance of free space [fs/V/fC]
27     Z0 = 376.7303135;
28
29 %******SELECT DIELECTRIC FUNCTION
30 % Get INTERPOLATED SMOOTHED PALIK/NW silver dielectric function, 300-600 nm
31 %   load newNWeps.dat; silver_eps = newNWeps; clear newNWeps;
32 % Get INTERPOLATED JOHNSON & CHRISTY silver dielectric function, 300-600 nm
33     load newJCeps.dat; silver_eps = newJCeps; clear newJCeps;
34 % EFFECTIVE MEDIUM DIELECTRIC CONSTANT
35     eps_m = 1;
36
37 %******SELECT INCIDENT LIGHT INITIAL CONDITIONS
38 % WAVEVECTOR
39 % Calculates direction of wavevector in Cartesian coords. given the Polar
40 % and Azimuthal angles (in radians) as inputs.
41     wavevector = [sin(Polar)*cos(Azimuthal),sin(Polar)*sin(Azimuthal),cos
(Polar)];
42 % POLARIZATION
43     ph2 = E0; % placeholder for info tags
44 % Incident light p-polarized (PARALLEL to plane-of-incidence); units
[Volts/nm];
45     E0p = [sin(Polar-pi/2)*cos(Azimuthal),...
46             sin(Polar-pi/2)*sin(Azimuthal),cos(Polar-pi/2)];
47 % Incident light s-polarized (NORMAL to plane-of-incidence); units
[Volts/nm];
48     E0s = [cos(Azimuthal+pi/2),sin(Azimuthal+pi/2),0];
49 % Normalized incoherent superposition of s- and p- polarizations; [V/nm];
50     E0i = (E0p+E0s)/sqrt(2);
51
52 if E0=='p' E0 = E0p;
```

Figure A.3.1. CDA program for spheres, page 1 of 4

```matlab
53 elseif E0=='s' E0 = E0s;
54 elseif E0=='i' E0 = E0i;
55 end;
56
57 %******PARTICLE ARRAY CALCULATION
58 % Returns particle positions in (x,y,z) coordinates such that the array is
59 % centered at the origin. All particle position units are [nm].
60
61 Total = 0; % counter variable
62 r=[];
63
64 % Deleted dim==1 option here for clarity!!
65
66 elseif dim==2 % Lattice is a 2D square array
67     if strcmp(type,'single')==1
68         ph1='S';
69         for i = 1:N
70             for j = 1:N
71                 Total = Total + 1;
72                 r = [r [(i-(N+1)/2)*space , (j-(N+1)/2)*space ,0].'] ;
73             end;
74         end;
75         % Deleted dimer, trimer options here for clarity!!
76     end;
77 else disp('Error in dimension or type variables');
78 end;
79
80 %******SELF-CONSISTENT DIPOLES and INTEGRATED INTENSITY
81 % File headers and array preallocation
82 % Create header information string to tag data columns
83     % Formatting trick to avoid decimal places in file headers
84     if detector*180/pi>=1
85         ph3 = num2str(detector*180/pi,'%03g');
86     elseif detector*180/pi<1
87         ph3 = sprintf('0p%03g',detector*1000*180/pi);
88     end;
89     header = sprintf('%d%s%s_%02d_%02dr%03d_%s_%d', dim, ph1, ph2, N,...
90         a, space, ph3, Polar*180/pi);
91 lambdavals = size(silver_eps,1);
92 lambdacol = silver_eps(:,1);
93 Alpha = [lambdacol zeros(lambdavals,1)];
94 Cabs = [lambdacol zeros(lambdavals,1)];
95 Cext = [lambdacol zeros(lambdavals,1)];
96 Csca = [lambdacol zeros(lambdavals,1)];
97 Qabs = [lambdacol zeros(lambdavals,1)];
98 Qext = [lambdacol zeros(lambdavals,1)];
99 Qsca = [lambdacol zeros(lambdavals,1)];
100 Power = [lambdacol zeros(lambdavals,1)];
101 tic
102 for num = 1:lambdavals % iterates over different values of wavelength
103     %******SELF-CONSISTENT DIPOLE ARRAY CALCULATION
104     % Returns a 3*Total x 1 vector (3 dipole moment components at each
105     % particle location for Total particles) for each wavelength of
106     % interest.
107
```

Figure A.3.2. CDA program for spheres, page 2 of 4

```
108        % Get wavelength [nm]
109            lambda = silver_eps(num,1);
110        % Get complex dielectric function [unitless]
111            epsilon = complex(silver_eps(num,2),silver_eps(num,3));
112        % Calculate wavenumber [nm^-1]
113            K0 = 2*pi/lambda;
114        % Incident wavevector
115            K = K0*wavevector;
116        % Straight sphere polarizability, without MLWA (Quasistatic limit!!)
117 %          Alpha_i = 4*pi*a^3*(epsilon-1)/(epsilon+2);
118 %          Alpha(num,2) = Alpha_i;
119        % MLWA polarizability [nm^3]
120        % Eqn.(16), Soller and Hall, JOSAB Vol.19, No.5, May 2002, p.1197
121 %          Alpha_i = 4*pi*a^3*(epsilon-1)/(3+(epsilon-1)*...
122 %              (1-(K0*a)^2-2*I*(K0*a)^3/3));
123 %          Alpha(num,2) = Alpha_i; % concatenate new value into alpha vector
124
125        % Polarizability based on Mie scattering coefficient al:
126            x = K0*a;  % Size parameter definition
127            m = sqrt(epsilon)/sqrt(eps_m); % "Relative" index of refraction
128            z = m*x; % convenient for argument of Bessel/Hankel functions
129            % See Bohren/Huffman p. 101 Eq(4.56), with recurrence relations for
130            % derivatives taken from Kerker, "The Scattering of Light and other
131            % electromagnetic radiation", p. 65. al is the Mie dipole
132            % scattering coefficient.
133            psiz = sqrt(pi*z/2)*besselj(1.5,z);
134            dpsiz = sqrt(pi*z/2)/2*(besselj(0.5,z) + besselj(1.5,z)/z -...
135                besselj(2.5,z));
136            psix = sqrt(pi*x/2)*besselj(1.5,x);
137            dpsix = sqrt(pi*x/2)/2*(besselj(0.5,x) + besselj(1.5,x)/x -...
138                besselj(2.5,x));
139            tsix = sqrt(pi*x/2)*besselh(1.5,1,x);
140            dtsix = sqrt(pi*x/2)/2*(besselh(0.5,1,x) + besselh(1.5,1,x)/x -...
141                besselh(2.5,1,x));
142 %          % Expressed in sin/cos form using identities from
143 %          %   Abramowitz/Stegun p.445:
144 %          psiz = sin(z)/z - cos(z);
145 %          dpsix = cos(x)/x + (1-x^-2)*sin(x);
146 %          psix = sin(x)/x - cos(x);
147 %          dpsiz = cos(z)/z + (1-z^-2)*sin(z);
148 %          tsix = (-I/x - 1)*exp(I*x);
149 %          dtsix = (-I + 1/x + I/x^2)*exp(I*x);
150            al=(m*psiz*dpsix - psix*dpsiz)/(m*psiz*dtsix - tsix*dpsiz);
151            Alpha_i = I*al*6*pi/K0^3;
152            Alpha(num,2) = Alpha_i;
153
154        % Calculate the incident electric field at each particle location
155            Ein = [];
156            % 1 V/nm incident field in either polarization, modulated only
157            % by phase
158            for i = 1:Total
159            Ein = [Ein E0*exp(I*dot(K,r(:,i)))] ;
160            end;
161        Ein = Ein.' ;            % unconjugated complex transpose
162
```

Figure A.3.3. CDA program for spheres, page 3 of 4

128

```
163        % Calculate the 3Total x 3Total interparticle interaction matrix that
164        % accounts for the retarded fields at each dipole location
165        Aij = [];
166            for i = 1:Total
167                for j = 1:Total
168                    % Self-interaction terms; 1/alpha terms along matrix
169                    % diagonal, 3 at a time
170                    if j==i
171                        Aij(3*i-2:3*i,3*j-2:3*j) = 1./Alpha_i/eps_0 * eye(3);
172                        continue;
173                    end;
174                    % rij vector for retarded field at ri from particle at rj
175                    rijv = r(:,j) - r(:,i);
176                    r_mat = rijv*rijv';           % 3x3 matrix rijrij
177                    rij = sqrt(dot(rijv,rijv)); % magnitude of rij vector
178                    % Interparticle interaction matrix
179                    Aij(3*i-2:3*i,3*j-2:3*j)=exp(I*K0*rij)/4/pi/eps_0/rij^3*...
180                        (K0*K0*r_mat - K0*K0*rij*rij*eye(3) + ...
181                        (1-I*K0*rij)*eye(3) - 3*(1-I*K0*rij)*r_mat/rij/rij) ;
182                end;
183            end;  % end of calculating matrix Aij
184
185        % Calculate dipole moments P [fC*nm] using MATLAB's left matrix divide
186        % operator
187          P = Aij\Ein;
188        % Calculate cross sections and extinction efficiencies
189          % "effective" polarizability of entire array for extinction
190          Alpha_eff = dot(Ein, P);
191          % EXTINCTION CROSS SECTION, SI version [nm^2]
192          Cext(num,2) = K0./eps_0.*imag(Alpha_eff)./dot(Ein, Ein);
193          % SCATTERING CROSS SECTION, SI version (must divide by eps_0 for
194          % each instance of effective polarizability)
195          Csca(num, 2) = K0.^4./6./pi.*Alpha_eff*Alpha_eff'./...
196              (dot(Ein, Ein))^2./eps_0.^2 ;
197          Qext(num,2) = Cext(num,2)/pi/a/a;   %extinction efficiency [unitless]
198          Qsca(num,2) = Csca(num,2)/pi/a/a;   %scattering efficiency [unitless]
199          Cabs(num,2) = Cext(num,2)- Csca(num,2);
200          Qabs(num,2) = Qext(num,2)- Qsca(num,2); %absorption efficiency
201
202        % Convert P from a 1 x 3N^2 vector to a 3 x N^2 matrix
203            P = reshape(P,3,[]);
204
205        %******INTEGRATED INTENSITY CALCULATION
206        % Integrate the power per steradian to get the total power inside a
207        % cone of opening angle specified by "detector". Natural units for the
208        % integration are spherical (r, theta, phi). Units of power_k are [W].
209        % File "integrand2.m" must be in the same directory as this program.
210            integral = dblquad(@integrand2, 0, detector, 0,...
211                2*pi,[],[],I,K0,Total,r,P);
212            power_k = c.^2.*Z0.*K0^4./32./pi^2 .* integral;
213            Power(num,2) = power_k;
214 end;
215 toc
216 disp(sprintf('Subroutine complete'));disp(datestr(now))
```

Figure A.3.4. CDA program for spheres, page 4 of 4

```matlab
1 function z = integrand2(x, y, I, K0, Total, r, P);
2 % "integrand" is the integrand of the double integral over the solid angle
3 % which is called by a CDA program file. It accepts a vector of x (theta)
4 % values and a scalar y (phi) value, and returns a vector of values of the
5 % integrand. It takes the total number of particles (Total), the array of
6 % dipole positions (r) and the array of self-consistent dipole moments (P)
7 % as inputs. Complex unit I and wavenumber K0 are also passed from the
8 % chosen CDA program. MAJOR ASSIST from Brian Lennon, EE, Vanderbilt.
9
10 s = size(x,2);
11 n1 = sin(x).*cos(y);
12 n2 = sin(x).*sin(y);
13 n3 = cos(x);
14 n = [n1; n2; n3];
15
16 d = reshape((n'*r)',[],1);
17 phase = repmat(exp(-I.*K0.*d'),3,1);
18 summand = reshape(phase.*mcross4(n,P),[3 Total s]);
19 nxp = squeeze(sum(summand,2));
20 nxpxn = arraycross(nxp,n);
21 z = [sin(x).*dot(nxpxn, nxpxn)];
```

Figure A.4. Integrand function called by CDA programs to calculate detector response.

130

```
 1 function [output] = mcross4(a,b)
 2 %MCROSS4 Cross products of 2 matrices of 3-vectors.
 3 %    A more general implementation of "MCROSS".
 4 %    output = MCROSS4(A,B)
 5 %    A is a 3 by M matrix
 6 %    B is a 3 by N matrix
 7 %    Output is a 3 by N*M 2-D array
 8
 9 output = [reshape(b(3,:).'*a(2,:) - b(2,:).'*a(3,:),1,[]);
10          reshape(b(1,:).'*a(3,:) - b(3,:).'*a(1,:),1,[]);
11          reshape(b(2,:).'*a(1,:) - b(1,:).'*a(2,:),1,[])];
```

Figure A.5. Custom matrix cross-product function "MCross4.m".

```
 1 function [output] = arraycross(a,b)
 2 %ARRAYCROSS Cross products of corresponding columns of 2 same-size
 3 %    matrices of 3-vectors. Used to compute "nxpxn" in integrands.
 4 %    output = ARRAYCROSS(A,B)
 5 %    A is a 3 by N matrix
 6 %    B is a 3 by N matrix
 7 %    Output is a 3 by N 2-D array, in which column j is the result of the
 8 %    cross product of A(:,j) with B(:,j)
 9
10 output = [a(2,:).*b(3,:)-a(3,:).*b(2,:);
11          a(3,:).*b(1,:)-a(1,:).*b(3,:);
12          a(1,:).*b(2,:)-a(2,:).*b(1,:)];
```

Figure A.6. Custom matrix cross-product function "ArrayCross.m".

REFERENCES

[1] M. Faraday, Philosophical Transactions of the Royal Society of London, Series A **147**, 145 (1857).

[2] G. Mie, Annalen der Physik **25**, 377 (1908).

[3] U. Kreibig and M. Vollmer, *Optical Properties of Metal Clusters.* Springer Series in Materials Science, Vol. 25, Springer Verlag, Berlin-Heidelberg, 1995.

[4] C. F. Bohren and D. R. Huffman, *Absorption and Scattering of Light by Small Particles.* Wiley-Interscience, New York, 1983.

[5] H. Raether, *Surface Plasmons.* Springer-Verlag, Berlin, 1988.

[6] N. W. Ashcroft and N. D. Mermin, *Solid State Physics.* Holt, Rinehart and Winston, Philadelphia, 1976.

[7] B. J. Soller and D. G. Hall, Journal of the Optical Society of America B **19**, 1195 (2002).

[8] W. Gotschy, K. Vonmetz, A. Leitner, and F. R. Aussenegg, Applied Physics B **63**, 381 (1996).

[9] A. J. Haes and R. P. Van Duyne, Journal of the American Chemical Society **124**, 10596 (2002).

[10] A. J. Haes, S. L. Zou, G. C. Schatz, and R. P. Van Duyne, Journal of Physical Chemistry B **108**, 6961 (2004).

[11] A. J. Haes, S. L. Zou, G. C. Schatz, and R. P. Van Duyne, Journal of Physical Chemistry B **108**, 109 (2004).

[12] A. D. McFarland and R. P. Van Duyne, Nano Letters **3**, 1057 (2003).

[13] H. G. Craighead and G. A. Niklasson, Applied Physics Letters **44**, 1134 (1984).

[14] B. Lamprecht, G. Schider, R. T. Lechner, H. Ditlbacher, J. R. Krenn, A. Leitner, and F. R. Aussenegg, Physical Review Letters **84**, 4721 (2000).

[15] A. Christ, S. G. Tikhodeev, N. A. Gippius, J. Kuhl, and H. Giessen, Physical Review Letters **91**, 183901 (2003).

[16] R. C. Johnson, J. T. Li, J. T. Hupp, and G. C. Schatz, Chemical Physics Letters **356**, 534 (2002).

[17] A. Wokaun, J. G. Bergman, J. P. Heritage, A. M. Glass, P. F. Liao, and D. H. Olson, Physical Review B **24**, 849 (1981).

[18] N. I. Zheludev and V. I. Emel'yanov, Journal of Optics A **6**, 26 (2004).

[19] Y. Cui, M. T. Bjork, J. A. Liddle, C. Sonnichsen, B. Boussert, and A. P. Alivisatos, Nano Letters **4**, 1093 (2004).

[20] A. J. Haes, C. L. Haynes, A. D. McFarland, G. C. Schatz, R. R. Van Duyne, and S. L. Zou, MRS Bulletin **30**, 368 (2005).

[21] B. K. Canfield, S. Kujala, K. Jefimovs, Y. Svirko, J. Turunen, and M. Kauranen, Journal of Optics A **8**, S278 (2006).

[22] D. J. Bergman and M. I. Stockman, Physical Review Letters **90**, 027402 (2003).

[23] S. A. Maier, M. L. Brongersma, P. G. Kik, S. Meltzer, A. A. G. Requicha, and H. A. Atwater, Advanced Materials **13**, 1501 (2001).

[24] S. A. Maier and H. A. Atwater, Journal of Applied Physics **98**, (2005).

[25] H. M. Gibbs, *Optical bistability: controlling light with light.* Academic Press, Orlando, 1985.

[26] R. Fuchs, Physical Review B **11**, 1732 (1975).

[27] S. Asano and G. Yamamoto, Applied Optics **14**, 29 (1975).

[28] M. I. Mishchenko, L. D. Travis, and D. W. Mackowski, Journal of Quantitative Spectroscopy & Radiative Transfer **55**, 535 (1996).

[29] S. A. Maier, P. G. Kik, and H. A. Atwater, Physical Review B **67**, (2003).

[30] T. Jensen, L. Kelly, A. Lazarides, and G. C. Schatz, Journal of Cluster Science **10**, 295 (1999).

[31] E. Moreno, D. Erni, C. Hafner, and R. Vahldieck, Journal of the Optical Society of America A **19**, 101 (2002).

[32] A. A. Lazarides and G. C. Schatz, Journal of Chemical Physics **112**, 2987 (2000).

[33] K. L. Kelly, E. Coronado, L. L. Zhao, and G. C. Schatz, Journal of Physical Chemistry B **107**, 668 (2003).

[34] J. D. Jackson, *Classical Electrodynamics.* 3rd ed., John Wiley & Sons, Inc., New York, 1999.

[35] L. L. Zhao, K. L. Kelly, and G. C. Schatz, Journal of Physical Chemistry B **107**, 7343 (2003).

[36] W. Rechberger, A. Hohenau, A. Leitner, J. R. Krenn, B. Lamprecht, and F. R. Aussenegg, Optics Communications **220**, 137 (2003).

[37] L. Gunnarsson, T. Rindzevicius, J. Prikulis, B. Kasemo, M. Kall, S. L. Zou, and G. C. Schatz, Journal of Physical Chemistry B **109**, 1079 (2005).

[38] S. L. Zou, N. Janel, and G. C. Schatz, Journal of Chemical Physics **120**, 10871 (2004).

[39] *Handbook of Optical Constants of Solids.* ed. E.D. Palik, Academic Press, 1985.

[40] P. B. Johnson and R. W. Christy, Physical Review B **6**, 4370 (1972).

[41] M. Quinten and U. Kreibig, Applied Optics **32**, 6173 (1993).

[42] M. Moskovits, I. Srnova-Sloufova, and B. Vlckova, Journal of Chemical Physics **116**, 10435 (2002).

[43] W. T. Doyle, Physical Review B **39**, 9852 (1989).

[44] M. Abramowitz and I. A. Stegun, *Handbook of mathematical functions with formulas, graphs and mathematical tables.* 10th ed., National Bureau of Standards Applied Mathematics Series, Vol. 55, U. S. Department of Commerce, Washington, D.C., 1972.

[45] N. V. Voshchinnikov and V. G. Farafonov, Astrophysics and Space Science **204**, 19 (1993).

[46] N. W. Liu, A. Datta, C. Y. Liu, and Y. L. Wang, Applied Physics Letters **82**, 1281 (2003).

[47] H. G. Craighead, Journal of Applied Physics **55**, 4430 (1984).

[48] R. Lopez, L. C. Feldman, and R. F. Haglund, Physical Review Letters **93**, 177403 (2004).

[49] M. D. McMahon, R. Lopez, H. M. Meyer, L. C. Feldman, and R. F. Haglund, Applied Physics B **80**, 915 (2005).

[50] A. Yelon, K. N. Piyakis, and E. Sacher, Surface Science **569**, 47 (2004).

[51] A. Pinchuk, U. Kreibig, and A. Hilger, Surface Science **557**, 269 (2004).

[52] U. Kreibig, G. Bour, A. Hilger, and M. Gartz, Physica Status Solidi A **175**, 351 (1999).

[53] J. M. Bennett, J. L. Stanford, and E. J. Ashley, Journal of the Optical Society of America **60**, 224 (1970).

[54] J. L. Stanford, Journal of the Optical Society of America **60**, 49 (1970).

[55] B. T. Reagor and J. D. Sinclair, Journal of the Electrochemical Society **128**, 701 (1981).

[56] J. P. Franey, G. W. Kammlott, and T. E. Graedel, Corrosion Science **25**, 133 (1985).

[57] T. E. Graedel, J. P. Franey, G. J. Gaultieri, G. W. Kammlott, and D. L. Malm, Corrosion Science **25**, 1163 (1985).

[58] T. Brandt, W. Hoheisel, A. Iline, F. Stietz, and F. Träger, Applied Physics B **65**, 793 (1997).

[59] U. Kreibig, M. Gartz, and A. Hilger, Berichte der Bunsen-Gesellschaft fuer Physikalische Chemie **101**, 1593 (1997).

[60] J. H. Payer, G. Ball, B. I. Rickett, and H. S. Kim, Materials Science & Engineering A **A198**, 91 (1995).

[61] *Handbook of Chemistry and Physics.* CRC Press, Boca Raton, FL, 2003-2004.

[62] D. K. Burge, J. M. Bennett, R. L. Peck, and H. E. Bennett, Surface Science **16**, 303 (1969).

[63] S. A. Maier, M. L. Brongersma, P. G. Kik, and H. A. Atwater, Physical Review B **65**, 193408 (2002).

[64] S. A. Maier, P. G. Kik, and H. A. Atwater, Applied Physics Letters **81**, 1714 (2002).

[65] S. A. Maier, P. G. Kik, H. A. Atwater, S. Meltzer, E. Harel, B. E. Koel, and A. A. G. Requicha, Nature Materials **2**, 229 (2003).

[66] N. Felidj*, et al.*, Physical Review B **65**, 075419 (2002).

[67] C. L. Haynes*, et al.*, Journal of Physical Chemistry B **107**, 7337 (2003).

[68] S. Linden, J. Kuhl, and H. Giessen, Physical Review Letters **86**, 4688 (2001).

[69] C. Sonnichsen*, et al.*, Applied Physics Letters **77**, 2949 (2000).

[70] M. D. McMahon, R. Lopez, R. F. Haglund, E. A. Ray, and P. H. Bunton, Physical Review B **73**, 041401 (2006).

[71] T. Götz, M. Buck, C. Dressler, F. Eisert, and F. Träger, Applied Physics A **60**, 607 (1995).

[72] F. R. Aussenegg, A. Leitner, and H. Gold, Applied Physics A **60**, 97 (1995).

[73] B. Lamprecht, A. Leitner, and F. R. Aussenegg, Applied Physics B **64**, 269 (1997).

[74] E. C. Hao, G. C. Schatz, R. C. Johnson, and J. T. Hupp, Journal of Chemical Physics **117**, 5963 (2002).

[75] B. K. Canfield, S. Kujalal, K. Jefimovs, T. Vallius, J. Turunen, and M. Kauranen, Journal of Optics A **7**, S110 (2005).

[76] A. M. Malvezzi, M. Patrini, A. Stella, P. Tognini, P. Cheyssac, and R. Kofman, European Physical Journal D **16**, 321 (2001).

[77] A. Podlipensky, J. Lange, G. Seifert, H. Graener, and I. Cravetchi, Optics Letters **28**, 716 (2003).

[78] Y. R. Shen, *The Principles of Nonlinear Optics.* John Wiley and Sons, New York, 1984.

[79] T. Vartanyan, M. Simon, and F. Trager, Applied Physics B **68**, 425 (1999).

[80] M. Simon, F. Trager, A. Assion, B. Lang, S. Voll, and G. Gerber, Chemical Physics Letters **296**, 579 (1998).

[81] B. Lamprecht, A. Leitner, and F. R. Aussenegg, Applied Physics B **68**, 419 (1999).

[82] B. Lamprecht, J. R. Krenn, A. Leitner, and F. R. Aussenegg, Applied Physics B **69**, 223 (1999).

[83] B. Lamprecht, J. R. Krenn, A. Leitner, and F. R. Aussenegg, Physical Review Letters **83**, 4421 (1999).

[84] H. G. Bingler, H. Brunner, A. Leitner, F. R. Aussenegg, and A. Wokaun, Molecular Physics **85**, 587 (1995).

[85] P. F. Liao, J. G. Bergman, D. S. Chemla, A. Wokaun, J. Melngailis, A. M. Hawryluk, and N. P. Economou, Chemical Physics Letters **82**, 355 (1981).

[86] E. Hao and G. C. Schatz, Journal of Chemical Physics **120**, 357 (2004).

[87] R. F. Haglund, L. Yang, R. H. Magruder, J. E. Wittig, K. Becker, and R. A. Zuhr, Optics Letters **18**, 373 (1993).

[88] G. Assanto, G. Stegeman, M. Sheikbahae, and E. Vanstryland, Applied Physics Letters **62**, 1323 (1993).

[89] Y. Chiu, U. Rambabu, M. H. Hsu, H. P. D. Shieh, C. Y. Chen, and H. H. Lin, Journal of Applied Physics **94**, 1996 (2003).

[90] T. F. Heinz, *Second-order nonlinear optical effects at surfaces and interfaces*, in *Nonlinear Surface Electromagnetic Phenomena*, H.-E. Ponath and G.I. Stegeman, Editors. 1991, North-Holland: Amsterdam. p. 353.

[91] R. D. Schaller, R. J. Saykally, Y. R. Shen, and F. Lagugne-Labarthet, Optics Letters **28**, 1296 (2003).

[92] T. Suzuki and T. F. Heinz, Optics Letters **14**, 1201 (1989).

[93] A. C. R. Pipino, R. P. Van Duyne, and G. C. Schatz, SPIE **2622**, 254 (1995).

[94] G. Kino and T. Corle, *Confocal Scanning Optical Microscopy and Related Imaging Systems*. Academic Press, San Diego, 1996.

[95] T. Dabbs and M. Glass, Applied Optics **31**, 3030 (1992).

[96] J. I. Dadap, J. Shan, and T. F. Heinz, Journal of the Optical Society of America B **21**, 1328 (2004).

[97] J. Nappa, G. Revillod, I. Russier-Antoine, E. Benichou, C. Jonin, and P. F. Brevet, Physical Review B **71**, 165407 (2005).

[98] E. Hecht, *Optics*. Addison-Wesley, Reading, Massachusetts, 1998.

[99] M. I. Stockman, D. J. Bergman, C. Anceau, S. Brasselet, and J. Zyss, Physical Review Letters **92**, (2004).

[100] B. K. Canfield, S. Kujala, K. Jefimovs, J. Turunen, and M. Kauranen, Optics Express **12**, 5418 (2004).

[101] J. I. Dadap, J. Shan, K. B. Eisenthal, and T. F. Heinz, Physical Review Letters **83**, 4045 (1999).

[102] H. Tuovinen*, et al.*, Journal of Nonlinear Optical Physics & Materials **11**, 421 (2002).

[103] B. K. Canfield, S. Kujala, M. Kauranen, K. Jefimovs, T. Vallius, and J. Turunen, Applied Physics Letters **86**, 183109 (2005).

[104] N. Bloembergen, R. K. Chang, S. S. Jha, and C. H. Lee, Physical Review **174**, 813 (1968).

[105] A. Habenicht, M. Olapinski, F. Burmeister, P. Leiderer, and J. Boneberg, Science **309**, 2043 (2005).

[106] V. Kotaidis, C. Dahmen, G. von Plessen, F. Springer, and A. Plech, Journal of Chemical Physics **124**, 184702 (2006).

[107] E. G. Gamaly, A. V. Rode, and B. Luther-Davies, Journal of Applied Physics **85**, 4213 (1999).

[108] A. Plech, V. Kotaidis, M. Lorenc, and J. Boneberg, Nature Physics **2**, 44 (2006).

[109] M. I. Stockman, S. V. Faleev, and D. J. Bergman, Physical Review Letters **88**, 067402 (2002).

[110] A. M. Moran, J. H. Sung, E. M. Hicks, R. P. Van Duyne, and K. G. Spears, Journal of Physical Chemistry B **109**, 4501 (2005).